

Cooper pair transport in arrays of Josephson junctions

Cooperpaartransport in Feldern von Josephson-Kontakten

Zur Erlangung des akademischen Grades eines
DOKTORS DER NATURWISSENSCHAFTEN
von der Fakultät für Physik des
Karlsruher Instituts für Technologie (KIT)

genehmigte

DISSERTATION

von

Dipl.-Phys. Jochen Oltmann Zimmer
aus Norden

Tag der mündlichen Prüfung: 21. Juni 2013

Referent: Prof. Dr. A.V. Ustinov

Korreferent: Prof. Dr. A. Shnirman

Contents

| | | |
|----------|--|-----------|
| 1 | Introduction | 1 |
| 2 | Charge transport through SQUID chains | 5 |
| 2.1 | Electrostatic modeling | 5 |
| 2.1.1 | Basic electrostatic model | 6 |
| 2.1.2 | FEM calculation of capacitance | 11 |
| 2.1.3 | Bias comb design calculations | 15 |
| 2.2 | Coherent properties | 22 |
| 2.2.1 | Superconductivity, Josephson junctions and SQUIDs | 22 |
| 2.2.2 | Quasiparticles | 28 |
| 2.2.3 | Quantum mechanics of an LC-circuit | 30 |
| 2.2.4 | The RCSJ model | 31 |
| 2.2.5 | Phase-charge duality | 33 |
| 2.2.6 | Junction chains in the Bloch limit | 36 |
| 2.2.7 | Random background charges | 39 |
| 2.3 | Hopping transport | 41 |
| 2.3.1 | General hopping model of a long array | 43 |
| 2.3.2 | Charge tunneling in ultrasmall junctions and P(E) . | 44 |
| 2.3.3 | Incoherent tunneling model of a long array | 49 |
| 3 | Fabrication methods | 53 |
| 3.1 | Optical lithography | 55 |
| 3.1.1 | Photolithography mask fabrication | 55 |
| 3.1.2 | Pattern transfer | 57 |
| 3.1.3 | Thin film metal deposition | 59 |
| 3.1.4 | Bond pads and leads design | 59 |
| 3.2 | Junction lithography | 61 |
| 3.2.1 | Electron beam lithography | 61 |

| | | |
|----------|---|------------|
| 3.2.2 | Shadow evaporation of Al/AlO _x /Al junctions | 64 |
| 3.2.3 | Fabrication of periodic SQUID chains | 65 |
| 3.2.4 | Aluminum T_c dependence on the film thickness . . | 69 |
| 4 | Measurements | 73 |
| 4.1 | Experimental setup | 75 |
| 4.1.1 | Low temperature environment | 75 |
| 4.1.2 | Wires and filters | 76 |
| 4.1.3 | Instruments | 76 |
| 4.2 | Sample characterization | 78 |
| 4.2.1 | Typical current-voltage characteristics | 78 |
| 4.2.2 | Charging energy and tunneling resistance estimation | 79 |
| 4.2.3 | Overview of samples | 81 |
| 4.2.4 | Estimation of the SQUID inductance | 85 |
| 4.3 | Voltage-activated conductance | 86 |
| 4.3.1 | Sample IFP11-255 | 87 |
| 4.3.2 | Sample KTH2011chip1 | 88 |
| 4.4 | Dual gap feature | 91 |
| 4.5 | Thermally activated conductance | 94 |
| 4.5.1 | Method for nonlinear conductances | 94 |
| 4.5.2 | Measurement results | 96 |
| 4.5.3 | Analysis by flux dependence | 98 |
| 4.5.4 | Additional data | 102 |
| 4.5.5 | Discussion | 103 |
| 4.6 | Analysis of flux noise influence | 105 |
| 4.6.1 | Setup modifications | 105 |
| 4.6.2 | Results | 105 |
| 4.6.3 | Discussion | 109 |
| 5 | Outlook | 113 |
| 6 | Conclusion | 117 |
| A | Incoherent tunneling model | 121 |
| B | Temperature Control | 125 |

| | | |
|----------|----------------------------|------------|
| C | Photolithography | 127 |
| C.1 | Mask fabrication | 127 |
| C.2 | Pattern transfer | 129 |
| D | E-beam lithography | 133 |
| | Bibliography | 137 |
| | Acknowledgments | 143 |

1 Introduction

The opinion seems to have got abroad, that in a few years all the great physical constants will have been approximately estimated, and that the only occupation which will then be left to men of science will be to carry on these measurements to another place of decimals.

James C. Maxwell

Introductory Lecture on Experimental Physics,
held at Cambridge in 1871 [NM65]

In this thesis, experimental work on one-dimensional small capacitance Josephson junction arrays (1D SCJJAs) is presented. The results help gain a quantitative understanding of the charge transport properties of these 1D SCJJAs, paving the way for applications in quantum metrology and the study of quantum phase transitions.

In this case, the Josephson junctions are superconductor-insulator-superconductor tunnel junctions. The capacitances C of the junctions are small in the sense that the quantized character of the charging energy $q^2/2C$, $q \in \{0, \pm e, \pm 2e, \dots\}$ becomes relevant (see e.g. Ref. [Bou+98]). A Josephson junction much smaller than a square micrometer might have a capacitance of 1 fF, leading to a single electron charging energy of $80 \mu\text{eV}$, which corresponds to a temperature of about 1 Kelvin.

If several small superconducting electrodes, often referred to as *islands*, are connected in series, each island is a site for charge localization, and Cooper pairs can tunnel from one to the other. It has been predicted that in a certain parameter range, a single Cooper pair can extend over several such islands [HBJS96]. A serial connection of several islands is called a chain or a (one dimensional) array. If the size of a charge object, determined by the electrostatic screening length Λ , is smaller than the length of the array, it is called a long array. Both Λ and the array length are usually expressed in the number of islands.

1 Introduction

The dynamics of this charge object can be modeled by non-linear equations of the sine-Gordon type, similar to the vortex motion in long Josephson junctions, where moving flux solitons can be observed (see e.g. Ref. [Ust98]). Therefore, in long SCJAs, *charge* solitons are expected ([HBS96]; [HD96]).

From the duality to the experimentally well known fluxon systems, a degree of control of the charge soliton movement is expected that enables Cooper pair counting with metrological precision. This would open the possibility to close the quantum metrological triangle (see e.g. Ref. [Piq+04]).

In this work, the islands are connected in two separate places, forming nano-scale superconducting quantum interference devices (nano-SQUIDs). This means that the tunneling probability of the Cooper pairs can be controlled by a weak external magnetic field. A scanning electron micrograph of a section of such a nano-SQUID chain is shown in Fig. 1.1.

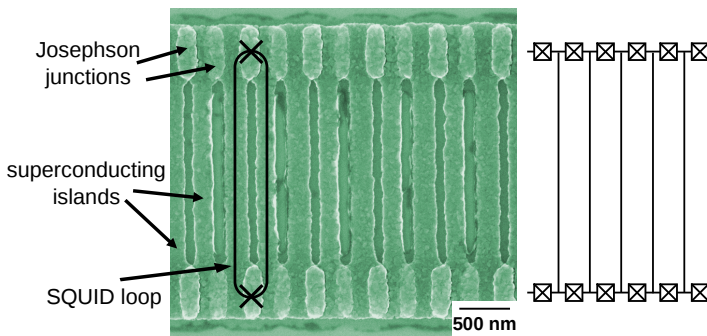


Figure 1.1: Section of a long nano-SQUID chain. The bright oval objects are Josephson junctions, connecting the Aluminum islands, which are superconducting below 1.2 Kelvin. Each pair of parallel Josephson junctions forms a SQUID. The circuit diagram of such a section is shown on the right.

By tuning the tunnel coupling between the islands, the transport properties can be changed from entirely superconducting to entirely insulating behavior. This makes the 1D SCJJA an in situ tuneable model system for a quantum phase transition [Hav+01].

The insulating behavior is expressed in the current-voltage characteristics as a Coulomb blockade. Transport through Coulomb blocked arrays can be activated e.g. by voltage, or by thermal energy. The thermally activated transport is the main subject of this thesis.

1D SCJJAs have been studied for two decades now. Aspects of the current-voltage characteristics can be explained, but quantitative understanding is still limited. A major advantage of measuring and analyzing the thermally activated conductance at zero bias is the accessibility to theoretical modeling. This may lead to a level of understanding sufficient to build devices for application.

Contents of this work

First, the properties of 1D SCJJA are examined theoretically, by analytical and numerical modeling (Chapter 2). The electrostatic limit of the arrays is described in section 2.1. In section 2.2, consequences of the superconducting nature of the sample, and the quantum mechanical nature in general, are discussed. A hopping model for charges in 1D SCJJAs is derived in section 2.3.

Then, the methods to fabricate these structures are described (Chapter 3). That chapter includes a brief report about an experiment on the special properties of Aluminum, the superconductor used for the reported experiments.

The setup, the characterization and measurement methods and all charge transport measurement results are included in Chapter 4.

Finally, an outlook (Chapter 5) and a conclusion (Chapter 6) are presented. In the appendix, details on calculations and on aspects of experimental realizations are included.

2 Charge transport through SQUID chains

Today's scientists have substituted mathematics for experiments, and they wander off through equation after equation, and eventually build a structure which has no relation to reality.

Nikola Tesla

Radio Power Will Revolutionize the World

in: Modern Mechanics and Inventions (July 1934)[Tes34]

2.1 Electrostatic modeling

Before considering the more realistic quantum mechanical description of the Josephson junction chains, it is useful to describe the system in the classic electrostatic limit. The tunnel effect is neglected, and the system is described as a network of capacitors (subsection 2.1.1).

The actual capacitance of some of the capacitors is very hard to determine experimentally, and the geometry is too complex for simplified analytic calculations. The capacitances are therefore calculated by numerically solving the electric field distribution for realistic geometries, as presented in subsection 2.1.2.

During the first part, it will become apparent that in the case of no transport, the bias voltage does not penetrate far into long chains. A modified environment geometry, a *bias comb* (2.1.3), will be presented to tackle that problem.

2.1.1 Basic electrostatic model

The basic model of an array of tunnel junctions is an infinite chain of capacitors of capacitance C , with each island having an additional capacitance C_0 to ground¹.

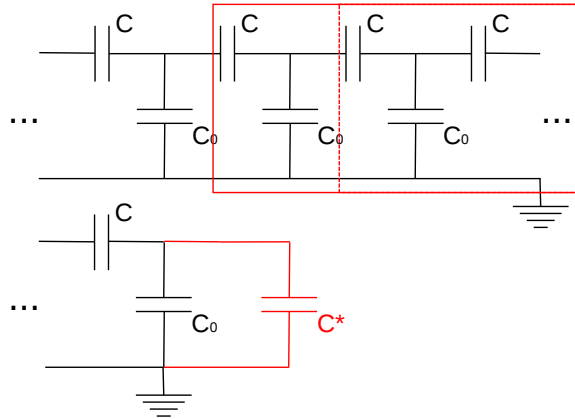


Figure 2.1: Infinitely long half-array. The addition of another island at the front does not change the capacitance.

The fact that the model array is infinitely long can be exploited analytically.

Effective capacitance within the array

Suppose an effective capacitance C^* that captures the ray of capacitance unit cells, infinite in one direction. The addition of an extra island at the front should not change the effective capacitance (see Fig. 2.1). So the effective capacitance fulfills

$$C^* = \left(\frac{1}{C} + \frac{1}{C_0 + C^*} \right)^{-1} \quad (2.1)$$

¹A similar description can be found in Ref. [Del91]. Ref. [Mel+97] describes a more general method that includes arbitrary capacitances and background charges.

Rewriting and solving for C^* , one arrives at:

$$C^* = \frac{C_0}{2} \left(\sqrt{1 + 4 \cdot \frac{C}{C_0}} - 1 \right) \quad (2.2)$$

In the described systems, the island to island capacitance C is much larger than the capacitance to ground. That means $\frac{C}{C_0} =: \Lambda^2$ is large, and it can be approximated:

$$C^* \approx \Lambda \cdot C_0 \quad (2.3)$$

Λ is the *electrostatic screening length*.

Static single charge excitation

Consider a single cooper pair charge of $2e$, sitting on an island somewhere in the infinite array. The neighboring islands are connected to ground by a capacitor C_0 and by the rest of the half-infinite chain. See figure 2.2 for visualization.

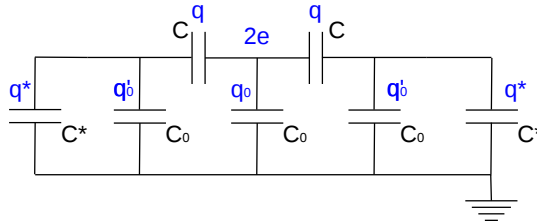


Figure 2.2: Environment of a localized charge on an island in the infinite array.

The equations for charge conservation are:

$$\begin{aligned} 2 \cdot q + q_0 &= 2e \\ q^* + q'_0 &= q \end{aligned}$$

The Kirchoff loop rule for the voltages gives

$$\begin{aligned}\frac{q}{C} + \frac{q'_0}{C_0} &= \frac{q_0}{C_0} \\ \frac{q^*}{C^*} &= \frac{q'_0}{C_0}\end{aligned}$$

The screening charges at the central island are:

$$\begin{aligned}q &= 2e / \left(\frac{1}{\Lambda^2} + \frac{1}{1 + \frac{C^*}{C_0}} + 2 \right) \\ q_0 &= 2e - 2q\end{aligned}$$

The screening continues in both directions. Using very similar equations, extra islands can be inserted, shifting C^* outwards. The charge on N -th capacitor in each direction, $q(N)$ and $q_0(N)$, can be calculated. One arrives at:

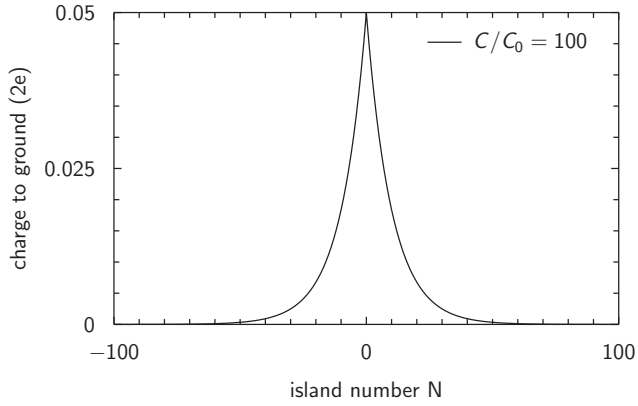
$$q(N) = q(N-1) / \left(\frac{1}{\Lambda^2} + \frac{1}{1 + \frac{C^*}{C_0}} + 1 \right) \quad (2.4)$$

$$q_0(N) = q(N) \cdot \left(\frac{1}{\Lambda^2} + \frac{1}{1 + \frac{C^*}{C_0}} \right) \quad (2.5)$$

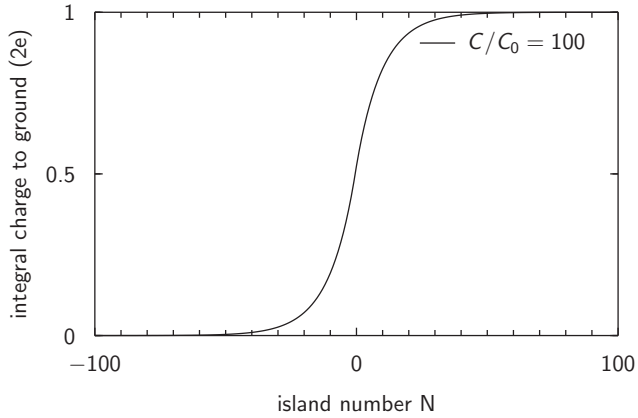
In the case of $\Lambda \gg 1$, Eq. can be iterated to $q_0(N+n) = q_0(N) \cdot (1 + 1/(1 + \Lambda))^{-n}$. It drops to $q_0(N)/e$ after $n = \Lambda + 1$ islands.

As an example, the case of $C/C_0 = 100$ has been chosen, because it is a good approximation of the typical experimental case. The screening charges on different islands are shown in Fig. 2.3(a). In the chosen example, the electrostatic screening length $\Lambda = 10$ gives a reasonable estimate of the size of the screening.

For islands that are much further than Λ islands away, the screening charge vanishes. The total screening of the excess charge is distributed over the ground capacitances, as one can see by summing up the $q_0(n)$: $\sum_{n=-100}^N q_0(n)$, as is shown in Fig. 2.3(b).



(a) Partial charge on GND capacitors



(b) Summed screening charge

Figure 2.3: Evaluation of the analytic solution for an infinitely long array. a) Charges on the ground capacitors. FWHM is ≈ 15 . b) Integral charge ($\sum_{n=-100}^N q_0(n)$) changes by $2e$ when passing the charged island.

The total effective capacitance of a single island is:

$$C_{\text{eff}} = C_0 + 2 \cdot C^* \quad (2.6)$$

The total energy of a single excess cooper pair is $E_{\text{tot}} = (2e)^2/(2C_{\text{eff}})$. In the limit of $C \gg C_0$, it will be useful to rewrite this in terms of the single junction cooper pair charging energy $E_c = (2e)^2/(2C)$:

$$E_{\text{tot}} = \frac{(2e)^2}{2C_{\text{eff}}} \approx \frac{(2e)^2}{2 \cdot (2C/\Lambda)} = \frac{\Lambda}{2} E_c \quad (2.7)$$

Bias voltage penetration

Suppose now the half-infinite array is connected to a voltage source. The charge on the first capacitor will be determined by the bias voltage. Beginning with the next island, the screening charges will follow equations 2.4 and 2.1.1. That means that the screening length Λ also applies to an electrostatic bias voltage penetrating the array.

In the following, an array will be considered *long* if the inner islands can be treated as parts of an infinite array, which means $N \gg \Lambda$. In the electrostatic limit picture, it is impossible to apply an electric force to a charge situated deep inside a long array – by definition.

Boundary effects

In reality, the limit of the infinite array is not be the best description. Even if one fabricates arrays with $N \gg \Lambda$, the islands close to the leads feel a different total screening. Consider a finite array. The first and last island are coupled to the leads in the same way as all the islands amongst each other, by capacitance C . Since for $C/C_0 \gg 1$, C is much bigger than the effective capacitance $C^* \approx C/\Lambda$, the total charging energy near the boundary is smaller than deep inside the array. The exact charging energy of each island is shown in Fig. 2.4.

The energy of an excess charge carrier rises to approach the infinite chain limit (Eq. 2.7). Λ islands in, the limit is already almost reached. In a transport model in the following section, this rise will be approximated by a linear rise over Λ islands.

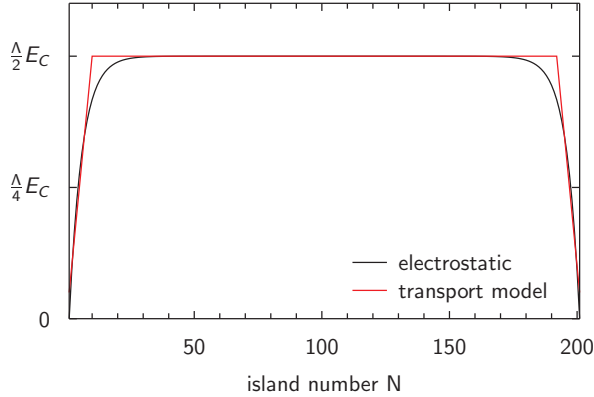


Figure 2.4: Total energy of an extra charge carrier, depending on its position, in the case of $C/C_0 = 100$. In the center, the energy is exactly the same as in the infinite chain limit (Eq. 2.7). Near the borders, the energy is lowered. A simple approximation is a linear change over Λ islands, shown in red.

2.1.2 Experimental realization details: finite element calculation of the capacitance to ground

A simple way to include ground capacitances into the electrostatic model is to assume a uniform ground capacitance, as discussed in the previous subsection.

Consider a uniform chain of strongly capacitively coupled islands, placed on an insulating surface in an experimental setup. The chain is connected to leads on both sides. For an island somewhere in the middle of the chain, the closest counter-electrode to define a ground capacitance might be the backside plane of the insulating substrate. An island on one of the sides will additionally form a capacitor with the lead electrode. This results in a very non-uniform ground capacitance profile. In order to produce uniform capacitances and thereby a uniform screening length, the distance to the ground electrode should be identical for all islands.

Our designs always feature ground electrodes in the same plane as the islands (see Fig. 2.5). In this subsection, capacitance calculations for that kind of geometry are presented.

Geometry of the model

The geometry we chose for the calculations is shown in Fig. 2.5.

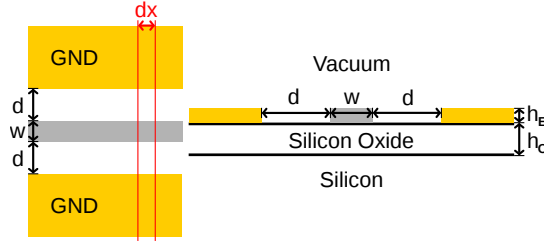


Figure 2.5: Geometry for the numerical simulation of the capacitance. Left: top view onto the substrate. A slice of infinitesimal thickness dx will be used for the 2D calculations. Right: Geometry of the slice. Height and width of the slice were chosen large enough that the electric field lines could run undisturbed. The figures are not to scale.

For simplicity and to economically use computation time, a two-dimensional slice model was used. It calculates a capacitance per unit length, which by multiplication with a typical island length gives an estimate of the island's ground capacitance.

The island size is $w = 1 \mu\text{m}$ times $h_E = 50 \text{ nm}$, the gap d is varied between $d = 0.25 \mu\text{m}$ and $d = 2 \mu\text{m}$. The top half is just vacuum ($\epsilon_r = 1$). Below the structures is a $h_O = 400 \text{ nm}$ layer of silicon oxide ($\epsilon_r = 4.5$), and below that is the silicon wafer ($\epsilon_r = 11.7$).

Computation

The capacitance was computed using the finite elements method (FEM, see e.g. ref [BBO04]) to solve Poisson's equation.

The geometry was defined in a parametrized form using the open software Salome², which was also used to generate the mesh, i.e. the discretization of the defined geometry.

The mesh was then imported to the open FEM solver software Elmer³, which numerically solved Poisson's equation. Von Neumann boundary conditions were applied.

The energy density of the electric field, as calculated by Elmer, is shown in Fig. 2.6.

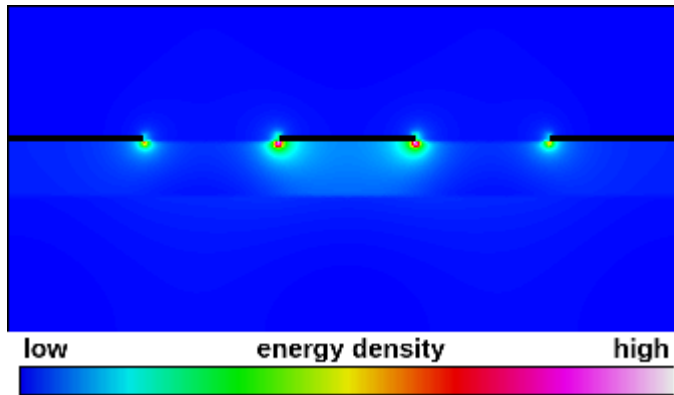


Figure 2.6: Energy density (arbitrary units) for a given charge on the island. Most of the electric field is concentrated in the Silicon Oxide layer.

Results

The resulting ground capacitance per nanometer is shown in Fig. 2.7.

The distance dependent data can be extrapolated with a power law, $C_0(d) \propto x^{-1/4}$. A typical island length of 200 nm and a ground electrode distance of 1 μm result in a C_0 of 13.4 aF. This agrees with the order of magnitude estimated for similar geometries⁴, and together with a typical

²Salome - Open Source Integration Platform for Numerical Simulation, Version 5.1.3, <http://www.salome-platform.org>

³ELMER - Open Source Finite Element Software for Multiphysical Problems, Version 5.5.0, <http://www.csc.fi/english/pages/elmer>

⁴Ref. [AAH01] estimates 9 aF, ref. [RS09] quotes 5-20 aF.

2 Charge transport through SQUID chains

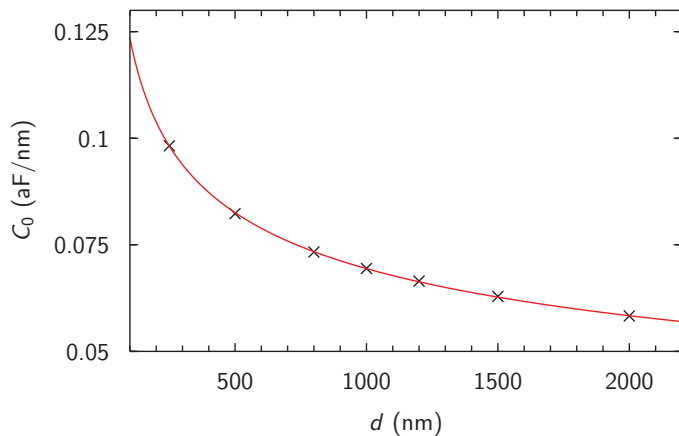


Figure 2.7: Simulated linear capacitance density depending on the distance between islands and electrodes. The data can be extrapolated with a power law, $C_0(d) \propto d^{-1/4}$ (red line).

junction capacitance of 1 fF, the screening length would indeed be on the order of 10.

2.1.3 Bias comb design calculations

In subsection 2.1.1, it has been shown that in the case of a continuous ground electrode, a bias voltage penetrates only on the scale of the electrostatic screening length Λ . For transport experiments, it is interesting to separate the charge screening length from the bias voltage screening length.

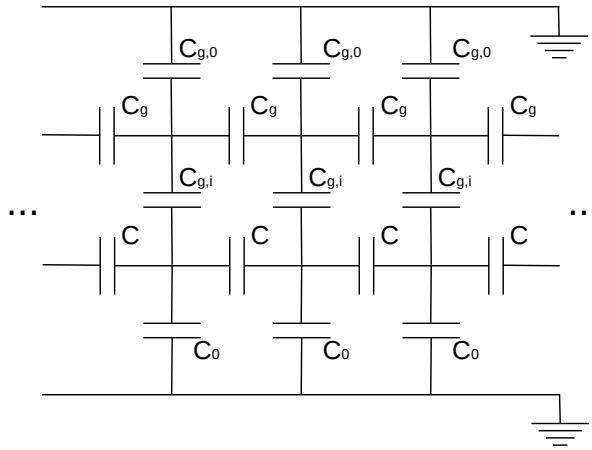


Figure 2.8: A simple capacitance model to illustrate the gate electrode concept. At the bottom, the usual infinite chain of islands is drawn. At the top, a similar chain of gate electrodes has been added, which is coupled to the islands in a simple one-to-one correspondence.

One possibility to separate the two screening lengths is sketched in Fig. 2.8: in addition to the islands with inter-island capacitances C and capacitances to ground C_0 , a set of gate electrodes has been placed on the substrate. The gates are coupled to each other by C_g and to ground by $C_{g,0}$, and each island is coupled to a corresponding gate electrode via $C_{g,i}$.

Suppose now that $C_0 \ll C_{g,i}, C_{g,0}$. Then C_0 can be neglected, and the ground capacitance is dominated by the gate electrodes. Suppose further $C_{g,i} \ll C_g, C_{g,0}$. If now a voltage is applied to the gate electrodes, the voltage distribution will be dominated by C_g and $C_{g,0}$, and the chain of islands can be ignored.

The screening of charge carriers on the islands is governed by $C/C_{g,i} =: \Lambda$, while the screening of a bias voltage depends on $C_g/C_{g,0} =: \Lambda_g$. As long as the limits $C_0 \ll C_{g,i}, C_{g,0}$ and $C_{g,i} \ll C_g, C_{g,0}$ are obeyed, Λ and Λ_g can be chosen independently.

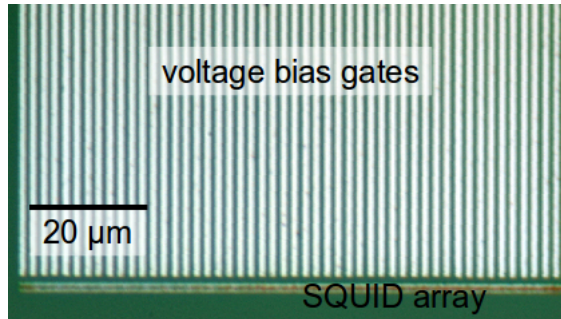


Figure 2.9: A Josephson junction array with voltage bias gates close by.

For the sake of simplicity, one gate electrode per island was discussed first. However, it is much easier to fabricate fewer, larger gate electrodes, as shown in Fig. 2.9. It is plausible that one benefits further from such a decision. The screening properties of the islands are not strongly affected by this design change, while immediately a longer bias voltage screening length is gained, which is understood as follows:

The voltage drops along the gate electrodes on the length of Λ_g . If there are n_i islands per gate, the effective voltage screening length is $n_i \Lambda_g$ in the island chain.

In order to test the approach, the capacitances between the islands and electrodes need to be calculated in a plausible geometry.

Finite element calculations

The capacitances between islands and gates were computed using the same software as in subsection 2.1.2, but now in a three-dimensional (3D) geometry. The model geometry is shown in Fig. 2.10.

The 3D geometry is chosen because unlike in the case of a continuous ground electrode, the electric field lines are not perpendicular to the

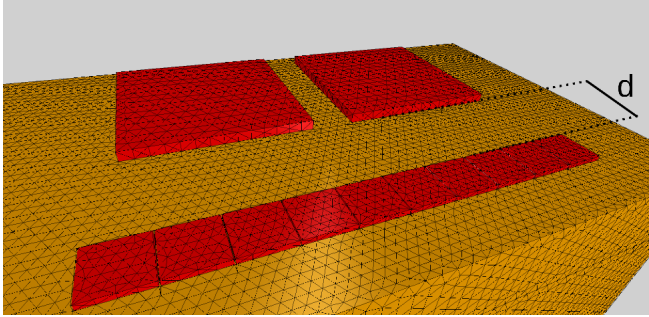


Figure 2.10: 3D Model and mesh of a simplified gate geometry. Two different distances d were simulated.

array. Instead, depending on the relative position of each island to the gate electrodes, the polarization of the dielectric has a different direction.

The oxide layer thickness is 400 nm. The islands are $(220 \text{ nm})^2$, with a distance of 5 nm between the islands. The islands' thickness in this model is 25 nm. The gates electrodes have a thickness of 50 nm, their size is $(900 \text{ nm})^2$. The distance between the gates is 225 nm.

The dimensions result in $n_i = 5$ islands per gate. Results are calculated using a distance between islands and gates d of 280 nm and 500 nm. They are shown in Fig. 2.11.

Algebraic calculations

In order to calculate voltage distributions in systems of electrodes, the best way to solve the system of linear equations is to find and invert the capacitance matrix (see e.g. ref [Max73]).

The capacitance matrix for a finite array of the type shown in Fig. 2.1 is:

$$\mathbf{C} = \begin{pmatrix} C & -C & 0 & \dots & 0 \\ -C & 2C + C_0 & \ddots & \ddots & \vdots \\ 0 & \ddots & \ddots & -C & 0 \\ \vdots & \ddots & -C & 2C + C_0 & -C \\ 0 & 0 & 0 & -C & C \end{pmatrix} \quad (2.8)$$

2 Charge transport through SQUID chains

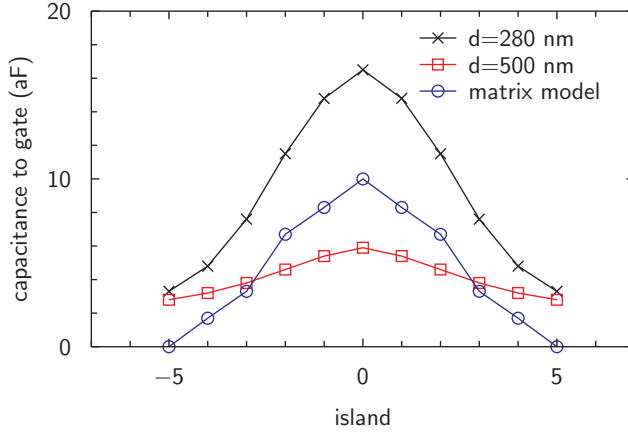


Figure 2.11: Resulting capacitances from the 3D FEM calculations. The blue dots show the capacitances used for the matrix calculations.

The diagonal contains the sum of all capacitances connected to a given electrode, while the coupling between individual electrodes is covered by entries of unequal indices.

At this point, the gate electrodes are included. For the calculation, the numerically backed up estimate of island-to-gate capacitances shown in Fig. 2.11 are used. The capacitances are chosen to resemble the numeric values, and to produce the same screening properties inside the array as in the continuous ground electrode case.

Every fifth island only couples to the electrode nearest to it (Fig. 2.12), with a capacitance $C_{g,i} = 10 \text{ aF}$. The four following islands have $(5/6)C_{g,i}$, $(4/6)C_{g,i}$, $(2/6)C_{g,i}$ and $(1/6)C_{g,i}$. They also couple to the following electrode, so that the total capacitance of one island to all gate electrodes is always $(6/6)C_{g,i}$. This scheme is illustrated in Fig. 2.12.

If we neglect the ground capacitance and couple the islands only to gate electrodes in this way, the part corresponding to the island chain will look very similar to Eq. 2.8:

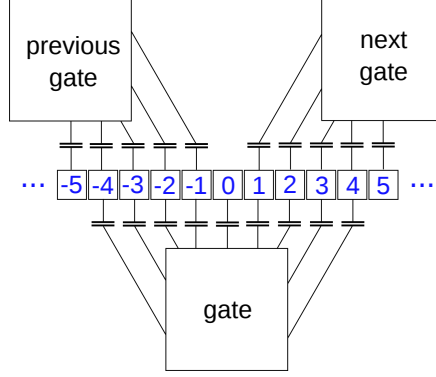


Figure 2.12: Each gate couples to nine islands in total. Every fifth island couples only to one gate, all the other islands couple to two.

$$\mathbf{C}_a = \begin{pmatrix} C + C_{g,i} & -C & 0 & \dots & 0 \\ -C & 2C + C_{g,i} & \ddots & \ddots & \vdots \\ 0 & \ddots & \ddots & -C & 0 \\ \vdots & \ddots & -C & 2C + C_{g,i} & -C \\ 0 & 0 & 0 & -C & C + C_{g,i} \end{pmatrix}$$

The total capacitance matrix takes the shape of a block matrix, with the uncoupled island chain \mathbf{C}_a and the uncoupled gates \mathbf{C}_g on the diagonal, and an interaction matrix \mathbf{C}_i on the off-diagonal.

$$\mathbf{C} = \begin{pmatrix} \mathbf{C}_a & \mathbf{C}_i^T \\ \mathbf{C}_i & \mathbf{C}_g \end{pmatrix}$$

Each gate electrode is connected to nine islands with a total capacitance of $5C_{g,i}$. That part therefore becomes:

$$\mathbf{C}_g = \begin{pmatrix} C_g + 3C_{g,i} & -C_g & 0 & \dots & 0 \\ -C_g & 2C_g + 5C_{g,i} + C_{g,0} & \ddots & \ddots & \vdots \\ 0 & \ddots & \ddots & -C_g & 0 \\ \vdots & \ddots & -C_g & 2C_g + 5C_{g,i} + C_{g,0} & -C_g \\ 0 & 0 & 0 & -C_g & C_g + 3C_{g,i} \end{pmatrix}$$

The interaction block is:

$$\mathbf{C}_i = \begin{pmatrix} C_{g,i} & \frac{5}{6}C_{g,i} & \frac{4}{6}C_{g,i} & \frac{2}{6}C_{g,i} & \frac{1}{6}C_{g,i} & 0 & 0 & \dots \\ 0 & \frac{1}{6}C_{g,i} & \frac{2}{6}C_{g,i} & \frac{4}{6}C_{g,i} & \frac{5}{6}C_{g,i} & C_{g,i} & \frac{5}{6}C_{g,i} & \\ 0 & 0 & 0 & 0 & 0 & 0 & \frac{1}{6}C_{g,i} & \\ \vdots & & & & & & & \ddots \end{pmatrix}$$

For the capacitance matrix calculations, GNU Octave⁵, is used.

The inter-island capacitance was set to be $C = 1$ fF, the inter-gate capacitance was $C_g = 50$ fF. The gates-to-ground capacitance was $C_{g,0} = 1$ fF.

The results are shown in Fig. 2.13. They are compared to calculations of screening in an array with normal ground electrode $C_0 = C_{g,i} = 10$ aF. The screening of a charge on one of the islands remains the same in both cases, while a bias voltage applied from one of the sides penetrates much further in the bias comb gated case.

⁵GNU Octave - A high-level interactive language for numerical computations, Version 3.2, <http://www.gnu.org/software/octave/>

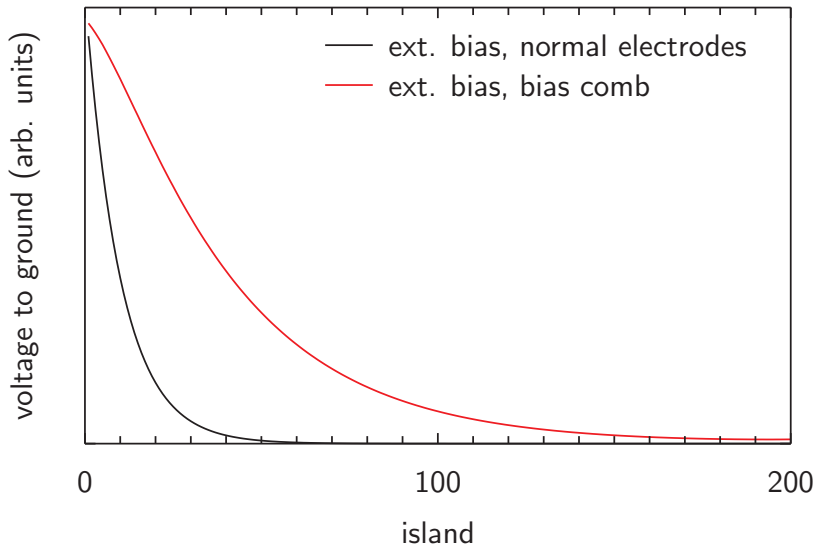


Figure 2.13: Results of the capacitance matrix calculations. The charge screening within the array remains unchanged, while the bias voltage penetrates much further into the array.

2.2 Coherent properties

Now that the electrostatics of our system are understood, tunneling can be introduced. Since the islands are superconducting, some properties of superconductors need to be recalled. The islands are coupled at two points by Josephson junctions, forming SQUIDs. Both concepts will be described in subsection 2.2.1. Transport through Josephson junctions is often accompanied by quasiparticle transport, discussed in subsection 2.2.2.

The basics of a quantum mechanical description of an ideal circuit are introduced (2.2.3), before showing the well-known RCSJ model of a real junction (2.2.4).

Charge and phase difference across a Josephson junction are conjugate variables. The small capacitances involved in the systems examined in this work shift the uncertainty towards the phase. The resulting equations are in many cases dual to the usual, large capacitance case (2.2.5). Chains of these small junctions show properties dual to those of long Josephson junctions, including the appearance of soliton-like excitations (2.2.6). The extent of the coherent properties in the small capacitance regime is limited by random background charges (2.2.7).

2.2.1 Superconductivity, Josephson junctions and SQUIDs

The subject of superconductivity and tunnel junctions has been exhaustively described in various textbooks⁶. Therefore, only a quick review of the properties necessary for this work will be provided.

Bardeen, Cooper and Schrieffer theory

Although superconductivity was known since Kamerlingh Onnes [Onn11] discovered it in 1911, the first successful microscopic theory was published 1957 by Bardeen, Cooper and Schrieffer ([BCS57], BCS theory).

In many solids, at sufficiently low temperatures, the electrons can develop a weak, long range attraction that is mediated by exchange of virtual phonons. In superconductors, the attraction is stronger than the Coulomb repulsion, which is screened by the surrounding charges. The

⁶The author used References [Lik86], [Sch97], [Tin04] and [IL08].

occupied fermionic electron states can bond to *cooper pairs*. Cooper pairs are bosonic particles and condense into a macroscopic quantum state.

For an excitation of an electronic degree of freedom in a superconductor in its ground state, a cooper pair must be broken up. The energy required for this is 2Δ , or Δ per electron. Δ is called the *superconducting gap*. The electronic excitation is a collective excitation of the solid that can have electron-like or hole-like properties. In this context, these excitations will be called *quasiparticles*.

As temperature is increased, cooper pairs break up by thermal excitation, and the size of the gap is reduced. If all cooper pairs are broken up, the gap is zero, and the superconductor changes to the normal state. The temperature at which this occurs is called critical temperature T_C , and according to BCS theory, it is related to the zero-temperature gap:

$$2\Delta_0 \approx 3.52 \cdot k_B T_C \quad (2.9)$$

All cooper pairs in a superconductor occupy the same macroscopic quantum state. Its wavefunction $\Psi(\vec{r})$ can be normalized such that gives the density of cooper pairs, $|\Psi(\vec{r})|^2 = n_{CP}$, which means:

$$\Psi(\vec{r}) = \sqrt{n_{CP}} \exp(i\theta(\vec{r})) \quad (2.10)$$

Near the phase transition of the superconductor, $|\Psi(\vec{r})|^2$ can be used in an expansion of the free energy. This is the basis of Ginzburg-Landau theory. $\Psi(\vec{r})$ is therefore often called the *Ginzburg-Landau order parameter*.

Flux quantization

Consider a superconducting loop in a magnetic field with vector potential \vec{A} . The current density inside the superconductor is

$$\vec{j}(\vec{r}) = q \langle \vec{v} \rangle_\Psi = q \Psi^* \vec{v} \Psi$$

Using the canonical momentum $m\vec{v} = (\vec{p} - q\vec{A})$ of a charged particle in an electromagnetic field and Eq. 2.10, one obtains

$$\vec{j} = \frac{n_{CP}q}{m} (\hbar\nabla\theta - q\vec{A})$$

Deep inside the superconductor, there is no magnetic field and no current, which means $\hbar\nabla\theta = q\vec{A}$.

The phase change of the order parameter must be single-valued, meaning that if we follow a closed path around the loop on the inside of the superconductor, the phase change acquired must be multiples of 2π :

$$\delta = \oint \nabla\theta \cdot d\vec{l} = 2\pi n$$

The magnetic flux through the loop is:

$$\int \vec{B} \cdot d\vec{f} = \int (\nabla \times \vec{A}) \cdot d\vec{f} = \oint \vec{A} \cdot d\vec{l} = \frac{\hbar}{q} \oint \nabla\theta \cdot d\vec{l}$$

Therefore, the flux through the loop must be quantized:

$$\int \vec{B} \cdot d\vec{f} = \frac{2\pi\hbar}{q} n$$

Since $q = 2e$, the flux is an integer multiple of

$$\Phi_0 = \frac{h}{2e} = 2.068 \cdot 10^{-15} \text{ Vs} \quad (2.11)$$

Φ_0 is called the *magnetic flux quantum*.

Josephson junction

If two electrodes of an identical superconductor are brought into close proximity, e.g. separated only by a nm-thick dielectric, the wave functions can overlap, coupling the two. This was first calculated by Josephson in 1962 [Jos62].

Let Ψ_1, Ψ_2 be the wave functions of the cooper pairs in the superconductors, and H_1, H_2 the corresponding Hamiltonians. In a perturbative approach, the coupling can be described by a small coupling constant T , and writing by the perturbed Schrödinger equations as:

$$i\hbar \frac{\partial \Psi_{1,2}}{\partial t} = H_{1,2} \Psi_{1,2} + T \Psi_{2,1}$$

Suppose a voltage U drops across the junction, and one can substitute the Hamiltonians by the corresponding energies:

$$i\hbar\dot{\Psi}_{1,2} = \frac{\pm qU}{2}\Psi_{1,2} + T\Psi_{2,1}$$

Inserting Eq. 2.10, one can derive equations for the cooper pair density and the phase of each superconductor:

$$\dot{n}_{\text{CP}1,2} = \pm \frac{2T}{\hbar} \sqrt{n_{\text{CP}1}n_{\text{CP}2}} \sin(\theta_2 - \theta_1)$$

$$\dot{\theta}_{1,2} = \frac{T}{\hbar} \sqrt{\frac{n_{\text{CP}2,1}}{n_{\text{CP}1,2}}} \cos(\theta_2 - \theta_1) \mp \frac{qU}{2\hbar}$$

If one defines a phase difference across the junction $\theta = \theta_2 - \theta_1$, it is easy to derive the *Josephson equations*:

$$I = I_C \sin(\theta) \tag{2.12}$$

$$U = \frac{\hbar}{2e} \dot{\theta} \tag{2.13}$$

In 1963 Ambegaokar and Baratoff[AB63] published calculations linking the critical current with the gap Δ and the normal state resistance R_n of the tunnel junction:

$$I_C(T) = \frac{\pi}{2e} \frac{\Delta(T)}{R_n} \tanh\left(\frac{\Delta(T)}{2 \cdot k_B T}\right) \tag{2.14}$$

Josephson energy and Josephson inductance

While the junction does not dissipate energy as long as the current stays below I_C , energy can be stored in it, as can be understood by the following calculation.

The work associated with changing the phase difference is (directly using Eq. 2.12, 2.13):

$$W = \int_{t_1}^{t_2} I \cdot U dt = \frac{\hbar I_C}{2e} \int_{t_1}^{t_2} \dot{\theta} \sin \theta dt$$

Substituting θ for t , one gets

$$W = \frac{\hbar I_C}{2e} (\cos \theta_1 - \cos \theta_2)$$

This can be seen as the result of the existence of a potential energy:

$$E(\theta) = E_J(1 - \cos \theta) \quad (2.15)$$

Here a characteristic energy scale of a Josephson junction was defined, the *Josephson energy*:

$$E_J = \frac{\hbar I_C}{2e} = \frac{\Phi_0 I_C}{2\pi} \quad (2.16)$$

Briefly look at the reaction of the Junction to an infinitesimal change in phase, $\theta \rightarrow \theta + \delta\theta$. The current will change by δI , resulting in:

$$I + \delta I = I_C \sin(\theta + \delta\theta)$$

Since $\delta\theta$ is infinitesimal, $\sin(\theta + \delta\theta) = \sin \theta + \cos(\theta)\delta\theta$, and $\delta I = I_C \cos(\theta)\delta\theta$. Using Eq. 2.13 and $\dot{\theta} = 0$, one gets:

$$U = \frac{\Phi_0}{2\pi} (\dot{\theta} + \delta\dot{\theta}) = \frac{\Phi_0}{2\pi} \frac{\delta I}{I_C \cos \theta}$$

By analogy to geometric inductances, a *Josephson inductance* is defined:

$$L_J(\theta) = \frac{L_J}{\cos \theta} = \frac{\Phi_0}{2\pi I_C} \frac{1}{\cos \theta} \quad (2.17)$$

DC SQUIDS

Consider two parallel identical Josephson junctions. First no magnetic flux penetrating the loop they form is assumed (see Fig. 2.14).

The phase difference across both branches, i.e. across both junctions, needs to be equal to the phase difference between the two conductors.

$$\delta_a^{JJ} = \delta_b^{JJ} = \phi_2 - \phi_1$$

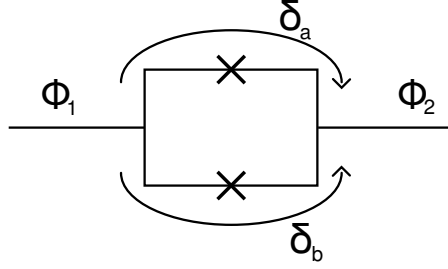


Figure 2.14: Phase differences in a DC SQUID.

If magnetic flux enters the ring, the phase difference across both junctions can no longer be equal. Instead, a phase difference of

$$\delta_b^{JJ} - \delta_a^{JJ} = \frac{2e}{\hbar} \phi = 2\pi \frac{\phi}{\Phi_0}$$

is acquired when going around the ring.

The total phase difference along one of the branches is a sum of the continuous phase change caused by the vector potential and the instantaneous jump across a Josephson junction:

$$\delta_{a,b} = \delta_{a,b}^{JJ} \pm \pi \frac{\phi}{\Phi_0}$$

The boundary condition of the phase in the conducting leads still applies. That means

$$\delta_a = \delta_b = \phi_2 - \phi_1$$

and therefore

$$\delta_a^{JJ} = (\phi_2 - \phi_1) - \pi \frac{\phi}{\Phi_0}$$

$$\delta_b^{JJ} = (\phi_2 - \phi_1) + \pi \frac{\phi}{\Phi_0}$$

The total current through the SQUID is a sum of the currents through the branches:

$$J = J_0 \left[\sin \left((\phi_2 - \phi_1) + \pi \frac{\phi}{\Phi_0} \right) + \sin \left((\phi_2 - \phi_1) - \pi \frac{\phi}{\Phi_0} \right) \right]$$

With the mathematical identity

$$\sin(\alpha + \beta) = \sin \alpha \cos \beta + \cos \alpha \sin \beta$$

one can write the current as:

$$J = \left(2J_0 \cos \frac{\pi\phi}{\Phi_0} \right) \sin(\phi_2 - \phi_1) = J_0(\phi) \sin(\phi_2 - \phi_1) \quad (2.18)$$

A flux dependent critical current $J_0(\phi)$ was defined. The device can be seen as a single Josephson junction with a tuneable critical current.

This device is an interferometer in the sense that it measures the phase difference acquired along the different branches. It is therefore called two-junction interferometer or, more catchy, a superconducting quantum interference device (SQUID). If one uses radio frequency (RF) techniques, a single junction loop is sufficient for measurements. Since the one-junction interferometer is called RF SQUID, the two-junction device is a DC SQUID.

Throughout this work, it will be assumed that the flux penetrating the loop is identical to the external flux, meaning the critical current can be tuned directly by the external flux. This approximation is only valid if the geometric inductance of the SQUID is much smaller than the Josephson inductance, usually measured as

$$\beta_L = \frac{L}{L_J} = \frac{2\pi I_C L}{\Phi_0} \quad (2.19)$$

As will be shown in section 4.2, this is the case for the SQUIDs in the examined arrays.

2.2.2 Quasiparticles

Excitations in a superconductor of single electronic character are called quasiparticles (QP). They can play an important role in single cooper pair devices.

Thermal equilibrium

According to BCS theory, a single electron excitation in the superconductor has the energy (see e.g. Ref. [Tin04]):

$$E_k = \sqrt{\Delta^2 + \xi_k^2} \quad (2.20)$$

ξ_k is the energy of the one-electron state k . If the superconductor is in thermal equilibrium, the occupation probability of the state k is the fermi function:

$$f_0(E_k/k_B T) = \frac{1}{1 + \exp(E_k/k_B T)} \quad (2.21)$$

Non-equilibrium quasiparticles

At low temperatures, when the thermal QP density is negligible, QP are often still observed. Since the low temperature setup is always connected to the high temperature lab, energy leakage creates QP that can take a considerable time to recombine, producing a steady state non-equilibrium QP density. Saira et al. [Sai+12] have strongly reduced the amount of QP in their system by taking very careful measures to shield their setup from stray microwave photons.

Trapping quasiparticles

In single cooper pair devices, the presence of a single quasiparticle can spoil the coherent properties of the single cooper pair tunneling. This is known as *quasiparticle poisoning*.

It has been shown by Court et al. [Cou+08] that it is possible to reduce the local quasiparticle density by attaching a normal metal to the superconductor. The metal is made weakly superconducting, this is known as the *proximity effect*. The gap Δ is smaller in the proximitized metal than in the superconductor. Quasiparticles can gradually relax to the gap edge and recombine, emitting an energy insufficient to break cooper pairs in the superconductor.

2.2.3 Quantum mechanics of an LC-circuit

For the following section it will be useful to know the Hamiltonian of an LC-circuit (see Ref. [IN91]), biased by a voltage source to voltage V . Let $U = Q/C$ be the voltage across the capacitor, e.g. the junction. One can define:

$$\varphi(t) = \frac{q}{\hbar} \int_{-\infty}^t dt' U(t') \quad (2.22)$$

φ is the *phase difference* across the junction. q can be e or $2e$, depending on the character of the conductor. The charging energy then becomes

$$E_c = \frac{Q^2}{2C} = \frac{C}{2} \left(\frac{\hbar}{q} \dot{\varphi} \right)^2 \quad (2.23)$$

The total phase difference ϕ is fixed by the external voltage $V = \hbar \dot{\phi}/q$. It is divided between capacitor and inductor, meaning the phase difference at the inductor is $\varphi - \frac{q}{\hbar} Vt$. Up to a factor of \hbar/q , this is the magnetic flux through the inductor, giving an inductive energy of:

$$E_l = \frac{1}{2L} \left(\frac{\hbar}{q} \right)^2 \left(\varphi - \frac{q}{\hbar} Vt \right)^2$$

The Lagrangian of this circuit is therefore:

$$\mathcal{L} = \frac{C}{2} \left(\frac{\hbar}{q} \dot{\varphi} \right)^2 - \frac{1}{2L} \left(\frac{\hbar}{q} \right)^2 \left(\varphi - \frac{q}{\hbar} Vt \right)^2$$

Transforming to Hamiltonian formalism, one finds that the charge on the junction and the phase are conjugate variables:

$$[\varphi, Q] = iq \quad (2.24)$$

The Hamiltonian is:

$$H = \frac{C}{2} \left(\frac{\hbar}{q} \dot{\varphi} \right)^2 + \frac{1}{2L} \left(\frac{\hbar}{q} \right)^2 \left(\varphi - \frac{q}{\hbar} Vt \right)^2 \quad (2.25)$$

It will be convenient to go to a rotating reference frame, with shifted variables $\tilde{\varphi}(t) = \varphi(t) - \frac{q}{\hbar}Vt$ and $\tilde{Q} = Q - CV$. The commutator remains $[\tilde{\varphi}, \tilde{Q}] = iq$, and the Hamiltonian becomes:

$$H = \frac{\tilde{Q}^2}{2C} + \frac{1}{2L} \left(\frac{\hbar}{q} \tilde{\varphi} \right)^2 \quad (2.26)$$

Quantum mechanics of a Josephson junction

If instead of a classical inductor and a classical capacitor, one takes a Josephson junction ($Q = 2e$), one has to replace the inductive energy by the Josephson energy.

$$H = \frac{C}{2} \left(\frac{\hbar}{q} \dot{\varphi} \right)^2 - E_J \cos(\varphi)$$

Because charge and phase are conjugate, Q can be replaced by $-i2e\partial_\varphi$. The Hamiltonian becomes:

$$H = -(E_C \frac{\partial^2}{\partial \varphi^2} + E_J \cos \varphi) \quad (2.27)$$

2.2.4 The RCSJ model

In order to describe a Josephson junction in the finite voltage state, the *RCSJ model* (resistively and capacitively shunted model, see e.g. ref [Tin04]) will be employed. An ideal Josephson junction, obeying equations 2.12 and 2.13, is shunted by a capacitor C , and a resistor R (see Fig. 2.15). The capacitor captures the capacitance between the superconducting electrodes, and the resistor models finite resistance, dissipation and voltage drop in case of a quasiparticle current.

If the junction is connected to a current source, the bias current is divided amongst the three parallel elements:

$$I_b = I_C \sin \phi + \frac{V}{R} + C \frac{dV}{dt}$$

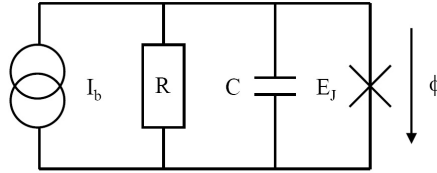


Figure 2.15: RCSJ model: An ideal junction is shunted by a resistor and a capacitor. From [GH10].

Applying the second Josephson equation, Eq. 2.13, the voltage can be eliminated:

$$I_b = I_C \sin \phi + \frac{\hbar}{2e} \frac{1}{R} \dot{\phi} + \frac{\hbar}{2e} C \ddot{\phi} \quad (2.28)$$

The tilted washboard potential

Suppose a potential U of a one-dimensional movement in coordinate ϕ , of the form:

$$U(\phi) = -E_J \cos \phi - \frac{I_b \hbar}{2e} \phi \quad (2.29)$$

Deriving a force from this acting a particle of mass $(\hbar/2e)^2 C$, the equation of motion is Eq. 2.28; the missing term $(\hbar/2e)^2 (1/R) \dot{\phi}$ can be interpreted as a drag force. The potential is shown in Fig. 2.16.

Depending on the bias current and the damping, the tilt of the potential can become so steep that the phase particle just slides down the washboard. The change in potential energy can be measured as a finite voltage drop.

Shapiro steps

If a Josephson junction is irradiated with microwave (MW) radiation of frequency f in a suitable frequency range, it is possible to *phase-lock* the junction: during each MW cycle, the phase particle changes its position

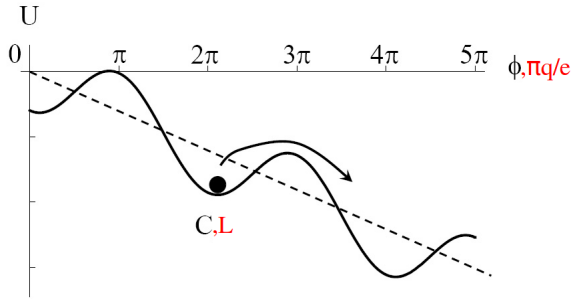


Figure 2.16: Tilted washboard potential: A phase particle of mass C / a quasi-charge particle of mass L move in a cosine potential, tilted by bias current/voltage. From [GH10], modified.

by the same integer number n of potential minima. The average voltage drop is then:

$$\langle V_n \rangle = n \frac{h}{2e} f$$

In a DC current-voltage measurement, the phase-locking takes the form of steps of constant voltage, known as *Shapiro steps* [Sha63]. In combination with a well defined frequency generator, this effect can serve to define a voltage standard independent of material parameters (see e.g. Ref. [Kau96]).

2.2.5 Phase-charge duality

As could be seen in the derivation of Eq. 2.24, phase and charge are conjugate variables. So far, the phase was treated as a well-defined, almost classical variable. This is a good description for relatively large junctions with small charging energies E_C . For smaller junctions, a full quantum mechanical description is necessary.

Bloch limit

Consider for a moment the case of $E_J \ll E_C$. The Josephson junction Hamiltonian (Eq. 2.27) looks like the Hamiltonian of a particle in free space, and the solutions are plane waves. In analogy to electrons in a metal, the E_J -part gives a periodic potential, and the eigenfunctions are Bloch states:

$$\psi_{nq}(\varphi + 2\pi) = \exp(iq\varphi/2e) \cdot \psi_{nq}(\varphi)$$

A quasi-charge q was defined in analogy to the quasi-momentum in a crystal. A Brillouin zone is formed with $-e \leq q \leq e$ (see Fig. 2.17). The energy is proportional to q^2 except for the edges of the Brillouin zone, where degeneracy is lifted, and a gap on the order of E_J is opened [Agr02].

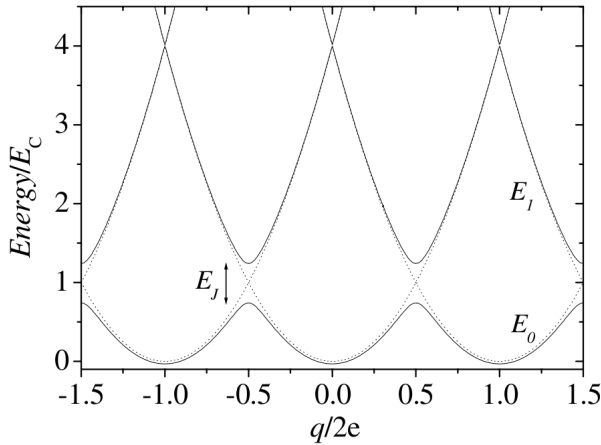


Figure 2.17: The Bloch limit. Quasi-charge bands are formed. For sufficiently large E_J , the lowest band can be approximated by a shifted, negative cosine. From Ref. [Agr02], modified.

Suppose the quasi-charge is changed slowly enough that the system always stays in the lowest band. The voltage drop across the junction can be calculated by the derivative of the energy of the lowest band, E_0 , with regard to quasi-charge. In the limit of negligible E_J , one gets a

sawtooth-function; for larger E_J , the voltage approaches a sine function. The exact shape can be found in Ref. [Agr02]. It will be written

$$V = V_C \text{saw}(q) \quad \text{or} \quad V = V_C \sin(q) \quad (2.30)$$

depending on the context. If the rather obvious equation is added:

$$I = \dot{q} \quad (2.31)$$

a set of equations dual to equations 2.12 and 2.13 is constructed.

The CJRL model

A junction in the Bloch limit can be described by a model dual to the RCSJ model: the capacitively shunted junction with a resistor and an inductor in series, in a voltage bias (see Fig. 2.18).

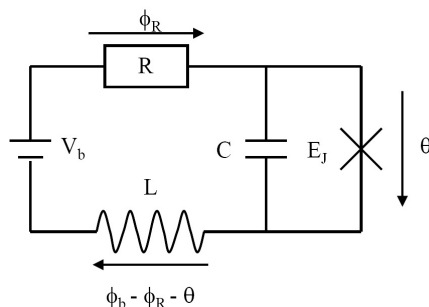


Figure 2.18: CJRL model: An ideal junction with its junction capacitance in series with a resistor and an inductor. From Ref. [GH10].

The voltage drop is divided amongst the components, leading to

$$V_b = V_C \sin \frac{\pi q}{e} + R\dot{q} + L\ddot{q} \quad (2.32)$$

This gives rise to a dual washboard potential (see Fig. 2.16), with the particle mass determined by L , and the quasi-charge as the spacial coordinate.

Guichard and Hekking [GH10] have predicted the emergence of current Shapiro steps, dual to the normal voltage Shapiro steps, in this regime. The experimental realization of this could be very useful for defining a quantum mechanical current standard in metrology.

2.2.6 Junction chains in the Bloch limit

So far, the equations governing a single junction in the Bloch limit were shown. In this subsection, an equation will be presented to describe a chain of such junctions, which will help to merge the electrostatic picture with the Josephson junction description. The equation is called sine-Gordon equation, because it is structurally similar to the Klein-Gordon equation⁷.

The sine-Gordon equation

Consider the model of a lossless electrodynamic *transmission line* (Fig. 2.19).

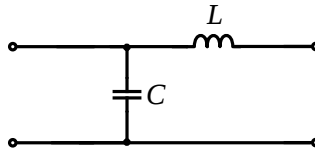


Figure 2.19: Transmission line element for deriving the simplified Telegrapher's equation.

Kirchhoff's law is applied to calculate currents and voltage drops in an infinitesimal part of the ideal line. This yields the Telegrapher's equation:

⁷The classical relativistic energy-momentum relation is $E^2 = p^2 c^2 + m^2 c^4$. In the non-relativistic limit, the correspondence transformation ($\hat{E} = i\hbar\partial_t$, $\hat{p} = -i\hbar\nabla$) yields the Schrödinger equation. Transforming the equation directly gives the Klein-Gordon equation:

$$\frac{1}{c^2} \partial_t^2 \varphi - \nabla^2 \varphi + \frac{m^2 c^2}{\hbar^2} \varphi = 0$$

$$\partial_x V = -l_0 \partial_t I$$

$$\partial_x I = -c_0 \partial_t V$$

l_0 and c_0 are linear densities of inductance and capacitance, respectively. From this, a wave equation for the voltage can easily be derived:

$$(l_0 c_0) \partial_t^2 V - \partial_x^2 V = 0$$

Assume a single Josephson junction (or a SQUID) obeys equations 2.30 and 2.31. A long array of these junctions can then be modeled similarly (see Ref. [HD96]). For this, an ideal Josephson junction is added in series with the inductor (Fig. 2.20).

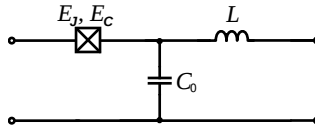


Figure 2.20: Josephson junction array element for deriving the charge sine-gordon equation.

The Telegrapher's equation has to be changed to:

$$\partial_x V = -l_0 \partial_t I - \frac{V_c \sin q}{c_0}$$

$$\partial_x I = -c_0 \partial_t V$$

Calculate the derivative:

$$\partial_x^2 I = -c_0 \partial_t \partial_x V$$

$$\partial_t \partial_x^2 q = \partial_t (-c_0 \partial_x V)$$

$$= \partial_t (c_0 l_0 \partial_t^2 q + c_0 V_c \sin q)$$

One arrives at a sine-Gordon equation with regard to the charge distribution:

$$c_0 l_0 \partial_t^2 q - \partial_x^2 q + c_0 V_c \sin q = 0 \quad (2.33)$$

Soliton solution of the Sine-Gordon equation

The simplified sine-Gordon equation is

$$\partial_t^2 \varphi - \partial_x^2 \varphi + \sin \varphi = 0$$

Claim: The soliton function

$$\varphi(x, t) = 4 \arctan \left(\exp \left(\frac{x - vt - x_0}{\sqrt{1 - v^2}} \right) \right) \quad (2.34)$$

solves the sine-Gordon equation.

Proof: First, substitute $\beta = \exp \left(\frac{x - vt - x_0}{\sqrt{1 - v^2}} \right)$ and use the angular relations

$$\sin 4\alpha = 8 \cos^3 \alpha \sin \alpha - 4 \cos \alpha \sin \alpha$$

$$\sin \alpha = \frac{\tan \alpha}{\sqrt{1 + \tan^2 \alpha}}$$

$$\cos \alpha = \frac{1}{\sqrt{1 + \tan^2 \alpha}}$$

Thus, it follows that:

$$\sin \varphi = \sin 4 \arctan \beta = \frac{4\beta(1 - \beta^2)}{(1 + \beta^2)^2}$$

Then replace $\frac{x - vt - x_0}{\sqrt{1 - v^2}} =: \alpha y$ and $\exp(\alpha y) =: x$. The second derivative of a function of x with regard to y is then

$$\left(\frac{d}{dy} \right)^2 f(x(y)) = \frac{d^2 f}{dx^2} \left(\frac{dx}{dy} \right)^2 + \frac{df}{dx} \frac{d^2 x}{dy^2}$$

Now, calculate the derivative of $\varphi(x(y)) = 4 \arctan x$, which yields $\frac{d^2}{dy^2} \varphi = \alpha^2 \frac{4x(1 - x^2)}{(1 + x^2)^2}$

The exponential function $\exp(\alpha y)$ acts under derivation like $\exp \left(\frac{x - vt - x_0}{\sqrt{1 - v^2}} \right)$ if you replace α with $\frac{1}{\sqrt{1 - v^2}}$ (with ∂_x) or $\frac{-v}{\sqrt{1 - v^2}}$ (with ∂_t).

Therefore φ solves the sine-Gordon equation.

Small soliton limit

In section 2.1, the tunneling of charges was neglected. As long as $E_C \gg E_J$, the picture remains valid. The soliton is the excess charge carrier together with the polarization of the neighboring islands. E_J can be treated as a perturbation. This regime has been discussed theoretically in Ref. [SEA09].

An intermediate regime was discussed by Rachel and Shnirman [RS09]. If $E_C > E_J > E_C/\Lambda$, the tunnel coupling between the islands is strong enough that cooper pair/ hole dipoles may temporarily form in proximity to an excess cooper pair. The charge is thus smeared over several islands.

Experimental evidence for charge solitons

In 1996, Haviland and Delsing [HD96] showed that the threshold voltage observed in their measurements, the voltage until which no transport was observed, could be predicted using the steady state solution of a sine-Gordon equation calculated for their array, indicating the existence of cooper pair charge solitons.

2.2.7 Random background charges

While the observation of the threshold voltage is consistent with the existence of charge solitons, the quantitative properties and reproducibility are severely influenced by randomly distributed background charges. These background charges can be observed by the static imposition of static charge offset, and by the dynamic properties, creating noise [JH00].

Single islands

It is generally believed that the origin of the background charges are traps for single electrons in the dielectric close to the small islands [Zor+96]. Zorin et al. measured the correlation of charge noise on two small metallic islands, 600 nm x 100 nm, in close proximity, 100 nm apart. The results are consistent with a model that locates the charge noise sources in the oxide layer covering their substrate.

Maisi et al. [Mai+09] measured the change of the offset charge of several single islands and found a drift by more than one elementary charge on the course of several days.

Arrays

A chain of islands is subject to a random distribution of background charges in the substate. If the offset induced on a single island is larger than one elementary charge, it is compensated by the tunneling of one electron or hole, which means one can immediately assume that each offset charge falls into the interval $[-e/2 : e/2]$ [JH00]. In an array, each charge is screened on the scale of Λ . Johansson and Haviland show that the free energy of an array can be minimized by additional tunneling of electrons, redistributing the charge. Depending on the screening length, this can have a considerable smoothing effect on the potential landscape.

2.3 Hopping transport

In this section, an incoherent tunneling model is introduced to predict the temperature- and coupling energy dependence of transport experiments reported in chapter 4, especially the zero bias conductance.

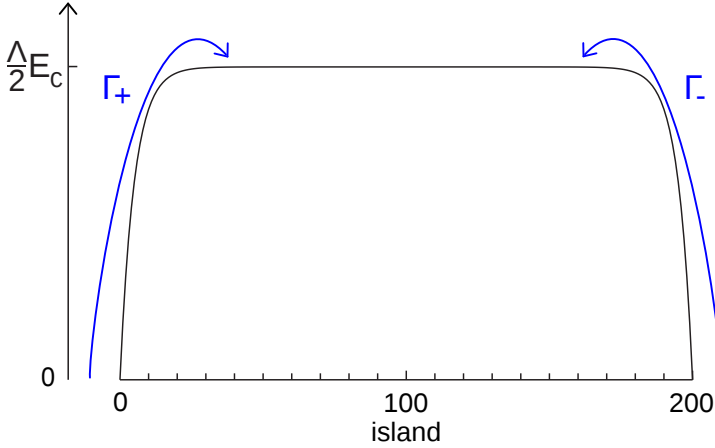


Figure 2.21: Energy scheme for the array model. The energy increases on a length scale of Λ islands to a total of $\Lambda E_C/2$. One can expect that the transport is limited by the rate of charges entering the array from either side, Γ_+ and Γ_- .

As a simplified picture, one might consider the following model. In subsection 2.1.1, it was shown that the total energy of an excess charge in a long array is $\Lambda E_C/2$ in the middle, but falls off exponentially at the sides (see Fig.2.21). One might therefore estimate the charge transport behavior by considering the limiting rates of charges entering the array from either side, for which thermal energy is required to overcome $E_A = \Lambda E_C/2$. The rates are Γ_+ and Γ_- . They are identical, except for an infinitesimal voltage V between the electrodes on the sides. The rates are:

$$\Gamma_+ \propto \exp\left(-\frac{(E_A - eV)}{k_B T}\right) \quad \Gamma_- \propto \exp\left(-\frac{E_A}{k_B T}\right)$$

The current is proportional to the difference of the rates:

$$\Gamma_+ - \Gamma_- = \Delta\Gamma \propto \left[\exp\left(\frac{eV}{k_B T}\right) - 1 \right] \exp\left(-\frac{E_A}{k_B T}\right)$$

This means that the zero bias differential conductance has this temperature dependence:

$$\left. \frac{\partial \Delta\Gamma}{\partial V} \right|_{V=0} \propto \frac{1}{k_B T} \exp\left(-\frac{E_A}{k_B T}\right)$$

This expression exhibits one maximum at $E_A = k_B T$. The temperature dependence of the conductance is shown in Fig. 2.22.

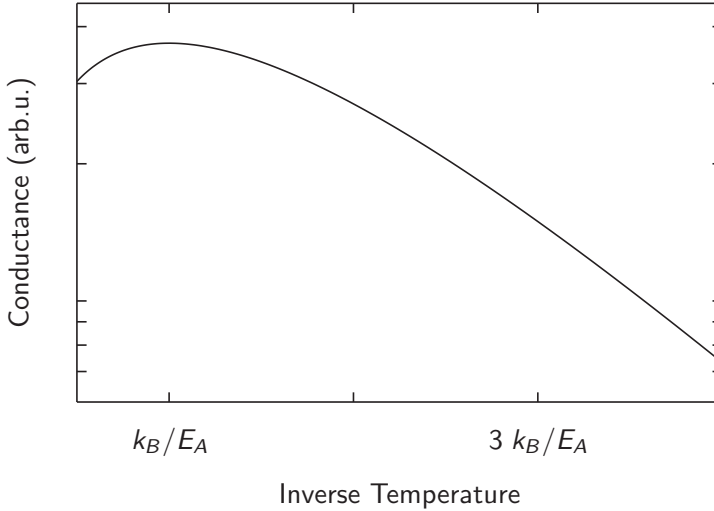


Figure 2.22: According to this simplified model, the zero bias differential conductance has one maximum at $E_A = k_B T$.

In the following subsections, these calculations are done more carefully. Subsection 2.3.1 derives a general hopping model for arbitrary site energies and general rates. Then, in subsection 2.3.2, a theory for charge tunneling through small junctions is reviewed. In subsection 2.3.3, that theory and a model for the site energies are used to build a specialized model of a small capacitance SQUID chain.

2.3.1 General hopping model of a long array

The model described here has been developed by N. Vogt and M. Marthaler in cooperation with the author. Details on the derivation can be found in the appendix A.

Assuming detailed balance for all carrier hopping rates between the islands, and that at most one extra carrier is in the array at any given time, a general description of the equilibrium transport can be formulated. In such a model, the net current through the array can be calculated by

$$I = -Ze(\Gamma_{n \rightarrow n+1}p_n - \Gamma_{n+1 \rightarrow n}p_{n+1}) \quad (2.35)$$

between any two islands, where Z is the carrier charge, the p are occupation probabilities, and Γ are the hopping rates.

The occupation probabilities and rates of neighboring sites are linked by the assumptions, leading to the following zero bias differential conductance:

$$g_0 = \frac{Z^2 e^2}{k_B T} \frac{1}{\sum_{n=1}^{N+1} \exp\left[-\frac{E_n}{k_B T}\right]} \left(\sum_{m=1}^{N+1} \frac{1}{\Gamma_{m-1,m}} \right)^{-1} \quad (2.36)$$

E_n are the corresponding site energies.

In the first term in the conductivity we approximate $\sum_{n=1}^{N+1} \exp\left[-\frac{E_n}{k_B T}\right] \approx 1$, which means that the empty state $E_n = 0$ is the one which is mostly occupied. The second term is mostly dominated by the rate $\Gamma_{n,n+1} = \exp(-E_n/k_B T)\Gamma_{n \rightarrow n+1}$ with the maximal energy E_{max} of the array. Therefore we can write the conductivity in the form,

$$g_0 = \frac{Z^2 e^2 \gamma}{(k_B T)^{1+\alpha}} e^{-E_{max}/k_B T}. \quad (2.37)$$

Since the rates themselves can have an explicit temperature dependence we allow for an additional exponent α in the temperature dependence of the prefactor.

As a first approximation, one would expect the thermally activated hopping conductance to exhibit $E_{max} \approx \Lambda E_C/2$.

2.3.2 Charge tunneling in ultrasmall junctions and P(E)

This section follows closely the publication by Ingold and Nazarov [IN91]. It will be reviewed for completeness.

A junction will be called ultrasmall in this context if its capacitance is in the order of femtofarads or below. For these junctions, the regime of $k_B T < E_C = q^2/2C$ becomes experimentally accessible.

Ideal voltage bias

What is the current through a tunnel junction that is connected to an ideal voltage source? Each charge tunneling will either gain or lose qV , depending on direction. For now, $q = e$ is taken. The total current is the difference of the currents passing through the junction from left to right and vice versa. Let $f(E)$ be the Fermi function of the left electrode:

$$I_{\rightarrow}(V) \propto \int dE (f(E) (1 - f(E + eV)))$$

$$I_{\leftarrow}(V) \propto \int dE ((1 - f(E)) f(E + eV))$$

This means one sums up all the probabilities to find an occupied state on one electrode and a corresponding free state on the other. Properly calculating the rates, the constants can be collected into a tunneling resistance R_T :

$$I(V) = \frac{1}{eR_T} \int dE [(f(E) (1 - f(E + eV))) - ((1 - f(E)) f(E + eV))]$$

Ideal current bias

Instead, consider an ideal current source pushing charge onto the junction at a steady, continuous rate. Tunneling, however, can only happen in quantized steps. A tunneling process is energetically favoured as soon as $\Delta E_C = Q^2/2C - (Q - e)^2/2C > 0$. If one defines a voltage across the junction as $U = Q/C$, that means a charge can only tunnel if $U > e/2C$. Note how this differs from the ideal voltage bias case.

Voltage bias with finite circuit resistance - the Coulomb blockade

In order to arrive at a more realistic model, an ideal voltage source is taken, and a large resistor is put in series with the junction (see Fig. 2.23). Switching on the voltage source, the junction is charged by a constant current which is determined by the serial resistor. If the voltage across the junction remains smaller than $e/2$, there will be no transport. Only external voltages above $e/2C$ will cause a current to flow, which will then be limited by the tunneling resistance as in the voltage biased case.

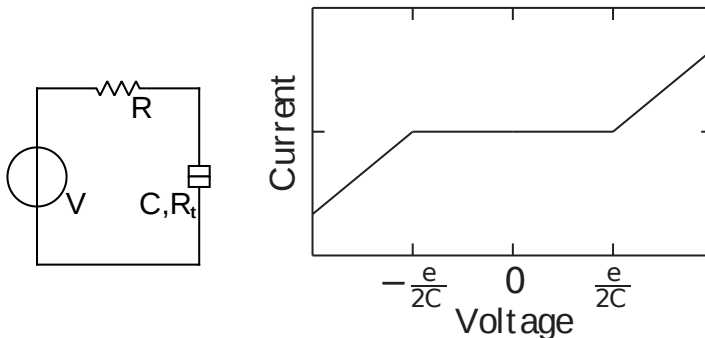


Figure 2.23: A voltage biased junction with a resistor in series to prevent instant recharging exhibits a coulomb blockade at zero temperature.

This absence of current below a threshold voltage is referred to as Coulomb blockade.

The fact that whether or not a Coulomb blockade is predicted depends on the environment considered shows that a generalized description of the environment is necessary for proper theoretical predictions.

Classic charge relaxation

Without tunneling, the junction can be described classically as a capacitor in series with its environment, which will be described by its impedance $Z(\omega)$. The equilibrium state in case of a voltage bias is a charge of $Q_e = CV$ on the capacitor. Suppose the capacitor is excited to a charge Q_0 at $t = 0$. It can be shown (e.g. in Laplace space) that the charge relaxation is described by

$$Q(t) = Q_e + (Q_0 - Q_e)R(t)$$

with a charge relaxation function $R(t)$ such that:

$$\int_0^\infty dt e^{-i\omega t} R(t) = \frac{C}{i\omega C + Z^{-1}(\omega)} =: C \cdot Z_t(\omega) \quad (2.38)$$

It can be shown that the $Z_t(\omega)$ defined here is the effective impedance as seen from the tunnel junction.

System Hamiltonian - quasiparticles

An arbitrary environment with impedance $Z(\omega)$ will cause dissipation. The usual way of describing a dissipative quantum system is to include extra degrees of freedom into the Hamiltonian, a set of harmonic oscillators. Recall the Hamiltonian of an LC resonator, defined in Eq. 2.26. It can be modified to include environmental LC degrees of freedom, coupled to the junction phase:

$$H_{\text{env}} = \frac{\tilde{Q}^2}{2C} + \sum_{n=1}^N \left[\frac{q_n^2}{2C_n} + \left(\frac{\hbar}{e} \right)^2 \frac{1}{2L_n} (\tilde{\varphi} - \varphi_n)^2 \right]$$

For a complete description, the quasiparticles on both electrodes need to be included:

$$H_{\text{qp}} = \sum_{k\sigma} \epsilon_k c_{k\sigma}^\dagger c_{k\sigma} + \sum_{q\sigma} \epsilon_q c_{q\sigma}^\dagger c_{q\sigma}$$

k and q are wave vectors on the left and right electrodes, ϵ are the energies, σ denotes the spin. The c, c^\dagger are fermionic ladder operators.

Tunneling is described by the tunneling Hamiltonian, coupling both electrodes:

$$H_T = \sum_{kq\sigma} T_{kq} c_{q\sigma}^\dagger c_{k\sigma} + h.c.$$

The total Hamiltonian becomes⁸:

$$H = \tilde{H}_{qp} + H_{env} + \tilde{H}_T$$

Tunneling rates and environment

The tunneling rates can be calculated using the golden rule:

$$\Gamma_{i \rightarrow f} = \frac{2\pi}{\hbar} |\langle f | \tilde{H}_T | i \rangle|^2 \delta(E_i - E_f)$$

To calculate the total rate $\vec{\Gamma}(V)$, all the rates weighted by the occupation probabilities have to be summed. The subspace of environmental states is traced out, giving a rate of:

$$\begin{aligned} \vec{\Gamma}(V) = & \frac{1}{e^2 R_T} \int_{-\infty}^{\infty} dE dE' f(E) [1 - f(E')] \\ & \cdot \int_{-\infty}^{\infty} \frac{dt}{2\pi\hbar} \exp\left(\frac{i}{\hbar}(E - E' + eV)t\right) \langle e^{i\tilde{\varphi}(t)} e^{-i\tilde{\varphi}(0)} \rangle \end{aligned} \quad (2.39)$$

R_T is a constant to collect all constant terms.

It is possible to rewrite the fourier transform part into:

$$\vec{\Gamma}(V) = \frac{1}{e^2 R_T} \int_{-\infty}^{\infty} dE dE' f(E) [1 - f(E')] P(E - E') \quad (2.40)$$

The influence of the environment is enclosed into $P(E)$, defined as:

$$P(E) = \frac{1}{2\pi\hbar} \int_{-\infty}^{\infty} dt \exp\left(J(t) + \frac{i}{\hbar}Et\right) \quad (2.41)$$

with the correlation function $J(t) = \langle [\tilde{\varphi}(t) - \tilde{\varphi}(0)]\tilde{\varphi}(0) \rangle$.

⁸The tilde denotes the fact that the influence of the voltage has to be taken care of, similar to the transition from Eq. 2.25 to 2.26.

The correlation function can be related to the temperature, written as $\beta = 1/k_B T$, and the effective impedance Z_t :

$$J(t) = 2 \int_0^\infty \frac{d\omega}{\omega} \frac{\text{Re}Z_t(\omega)}{R_K} \left\{ \coth\left(\frac{1}{2}\beta\hbar\omega\right) [\cos(\omega t) - 1] - i \sin(\omega t) \right\}$$

High impedance environment

In the case of very high ohmic damping, $Z(\omega) = R$, $R \gg R_K$, the effective impedance becomes

$$\text{Re}Z_t(\omega) = \frac{R}{1 + (\omega RC)^2} \rightarrow \frac{\pi}{C} \delta(\omega)$$

From this, the following expression for $P(E)$ can be derived:

$$P(E) = \frac{1}{\sqrt{4\pi E_C k_B T}} \exp\left[-\frac{(E - E_C)^2}{4E_C k_B T}\right] \quad (2.42)$$

System Hamiltonian - cooper pairs

Instead of the quasiparticle excitations and the tunnel hamiltonian, the total Hamiltonian now consists of the environment and the Josephson energy:

$$H = H_{\text{env}} + E_J \cos(2\varphi) = H_{\text{env}} + \left(\frac{E_J}{2} e^{-2i\varphi} + H.c.\right)$$

The Josephson term describes the tunneling of cooper pairs, since $e^{-2i\varphi}$ is a propagator for the charge.

Cooper pair tunneling rates

Performing similar steps to trace out the environment, Eq. 2.39 has to be changed into:

$$\vec{\Gamma}(V) = \frac{E_J^2}{\hbar^2} \int_{-\infty}^{\infty} dt \exp\left(\frac{2i}{\hbar} eVt\right) \langle e^{2i\tilde{\varphi}(t)} e^{-2i\tilde{\varphi}(0)} \rangle$$

The rate is rewritten as

$$\vec{\Gamma}(V) = \frac{\pi}{2\hbar} E_j^2 P(2eV) \quad (2.43)$$

with a modified $P(E)$:

$$P(E) = \frac{1}{2\pi\hbar} \int_{-\infty}^{\infty} dt \exp \left[4J(t) + \frac{i}{\hbar} Et \right] \quad (2.44)$$

2.3.3 Incoherent tunneling model of a long array

This subsection describes the application of $P(E)$ theory to the general hopping model of subsection 2.3.1, and the application of quasiparticle rates. For a more detailed derivation, see appendix A.

The site energies and the rates of the model are depicted in Fig. 2.24.

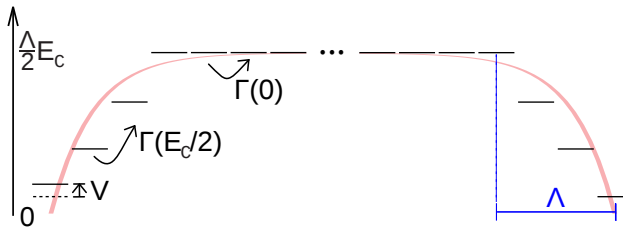


Figure 2.24: Level scheme for the array model. The energy increases linearly on a length of Λ islands. $\Gamma(\delta E)$ are the hopping rates, depending on the site energy difference.

The zero bias conductance then takes the form:

$$g_0 = \frac{Z^2 e^2}{k_B T} \left[1 + N' e^{-\Lambda \frac{E_c}{2k_B T}} + 2 \sum_{m=1}^{\Lambda-1} \left(e^{-m \frac{E_c}{2k_B T}} \right) \right]^{-1} \times \frac{\Gamma(0) \Gamma(\frac{E_c}{2})}{(\Lambda + e^{\frac{E_c}{k_B T}} \Lambda) \Gamma(0) + (N - 2\Lambda) \Gamma(\frac{E_c}{2})} \quad (2.45)$$

$$N' = (N - 2\Lambda - 1) \quad (2.46)$$

where N' is the number of sites with the energy $E = \Lambda E_c/2$ in the bulk and $\Gamma(0)$ and $\Gamma(E_c/2)$ are the rates corresponding two the hopping rates between neighbouring sites that correspond to the two Energy differences $\delta E = E_{n+1} - E_n$ between neighbouring sites that occur in this model: $\delta E = 0$ and $\delta E = E_c/2$.

Cooper pair tunneling

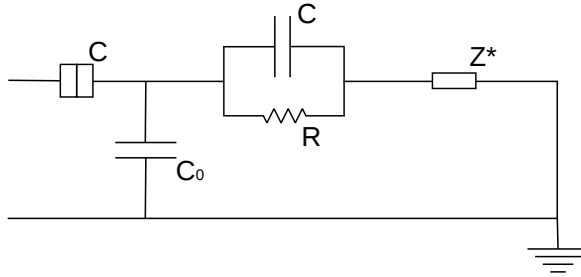


Figure 2.25: Impedance model. The junction is shown on the left. On both sides, it sees an effective impedance Z^* . An analytic expression can be found for Z^* .

If one wants to apply $P(E)$ theory for the array transport, the environment impedance of a junction within the array needs to be estimated.

The circuit environment is shown in Fig. 2.25. Similar to the effective capacitance of section 2.1.1, an analytic expression can be found for Z^* :

$$\frac{1}{Z^*(\omega)} = i\omega C_0 + \left(\frac{R}{1 + i\omega RC} + Z^*(\omega) \right)^{-1}$$

This is solved by:

$$Z^*(\omega) = \frac{R}{2(1 + i\omega CR)} \left(\sqrt{1 + 4 \cdot \frac{1 + i\omega CR}{i\omega C_0 R}} - 1 \right)$$

For small $1/\omega R$, the factor on the right can be approximated as 2Λ .

$$\frac{1}{Z^*(\omega)} \approx \frac{1}{\Lambda R} + \frac{i\omega C}{\Lambda}$$

The effective impedance $Z_t(\omega)$ from the Junction's perspective, as defined in Eq. 2.38, is then

$$Z_t(\omega) = \frac{1}{i\omega C + 1/(\Lambda R) + i\omega C/\Lambda}$$

which is taken as motivation to assume the high impedance Gaussian form of $P(E)$ from Eq. 2.42.

Then, for the Cooper-pair tunnelling, one can assume:

$$\Gamma_{n \rightarrow n+1} = \frac{E_J^2 \pi}{\hbar} P(\delta E) = \frac{E_J^2 \pi}{\hbar \sqrt{4\pi E_C k_B T}} \exp \left[-\frac{(\delta E - E_C)^2}{4E_C k_B T} \right] \quad (2.47)$$

Equilibrium quasiparticles

Suppose the above mechanism of Cooper pair transport is not the only charge transport mechanism. A likely candidate for a mechanism independent of the Josephson coupling is the charge transport by equilibrium quasiparticles.

From the semiconductor model of quasiparticle tunneling, the following tunneling rate through a single junction is derived (see e.g. Ref. [Tin04]):

$$\Gamma(\delta E) = \frac{1}{e^2 R_T} \int_{-\infty}^{\infty} N_1(E) f(E) N_2(E + \delta E) [1 - f(E + \delta E)] dE$$

For a BCS density of states and $\delta E \ll \Delta$, the quasiparticle rate can be approximated as:

$$\Gamma(\delta E) \approx \frac{\Delta}{e^2 R_T} \exp\left(-\frac{\Delta}{k_B T}\right) \quad (2.48)$$

3 Fabrication methods

Est autem Alchimia (ut more loquamur humano) casta meretrix, quae amatores plures habet, sed delusis omnibus in nullis unquam pervenit amplexus. Ex stulris facit insanos, ex divitibus pauperes, ex philosophis fatuos, ex deceptis loguacissimos deceptores.^a

^aAlchemy, however, is a chaste prostitute, who has many lovers but disappoints all and grants her favors to none. She transforms the haughty into fools, the rich into paupers, the philosophers into dolts, and the deceived into loquacious deceivers.

Johannes Trithemius
Annalium Hirsaugensium Tomi II, first printed 1690

This chapter describes the steps that were necessary to fabricate the nanostructures for the experiments presented in chapter 4.

The connection from the macroscopic world, with its soldered cables and wires that the experimentalist can still handle manually, to the truly nanoscopic world that even a good microscope can not properly resolve, is usually produced with optical tools. Those steps will be described in section 3.1.

In order to observe single charge effects, $E_C = q^2/2C > k_B T$ must be achieved. Under typical experimental conditions, this means capacitances on the order of a femtofarad are needed. Since the typical capacitance of a Aluminum/Aluminum oxide/Aluminum capacitor is $45 \text{ fF}/\mu\text{m}^2$ (see e.g. Ref. [HD96]), the resolution needs to be considerably better than a micron.

True sub-micron resolution is hard to achieve by optical means, simply because of the natural limitation by the wavelength of the photon, which

is quite tricky to overcome¹. The nanostructuring is therefore done with high energy electrons in the kilovolt range. A method to fabricate small tunnel junctions of Aluminum and Aluminum Oxide using electron-beam lithography is presented in section 3.2. That section also contains a short review of an experiment that has been performed during the time of this work. It examines the dependence of the superconducting critical temperature, and therefore of the superconducting gap, on the film thickness of thin Aluminum films.

¹Using ultraviolet light and special techniques to increase numerical aperture, the wavelength limitation can be stretched, as modern semiconductor technology demonstrates.

3.1 Optical lithography

In this section, the methods that were used to fabricate the leads to the nanostructures will be described. A photomask was produced by laser lithography (subsection 3.1.1). The pattern on the mask was transferred (subsection 3.1.2) to a substrate, where metal was selectively deposited (subsection 3.1.3).

The more technical process step descriptions and parameters have been put into the appendix C.

3.1.1 Photolithography mask fabrication

For photomask fabrication, commercial photomask blanks were used. The mask blanks were sheets of quartz, covered with a thin layer of chromium².

Resists and developers

A *photoresist* is a material that is sensitive to exposure to certain types of light. After exposure, a selective solvent, the *developer* for a given resist, can be used to dissolve parts of the resist. A *positive* resist becomes soluble during exposure, while the unexposed resist is left unchanged during development. For a *negative* resist, it is the opposite.

Resists can be applied to a substrate in a process called *spin coating*[Law88]. The substrate is rotated at several thousand rounds per minute, and a resist solution is put onto its surface. The centrifugal force of the rotation distributes the resist casting solution, until a thin film remains. The film thickness is uniform over most of the substrate's surface, and it can be controlled by choosing the spinning speed:

$$h = k/\sqrt{\omega}$$

h is the layer thickness, ω the angular velocity, and k is a constant depending on solid concentration and solution viscosity.

²Mask dimensions: 4 inch x 4 inch with a thickness of 0.09 inch from MBWhitaker & Associates

3 Fabrication methods

The substrate is dried, removing the remaining casting solvent, and the resist is ready for exposure.

For all experiments in direct writing of microstructures, the commercially available resist S 1805³ was used. The mask blanks (see below) came precoated with 530 nm of AZ 1518⁴, which was used in that case. Both are positive resists, and we used MF-319⁵ photoresist developer for both.

Direct Laser lithography

A Heidelberg Instruments DWL66 laser writer was used to pattern the photomask blanks. We chose a configuration that combined high resolution with high writing speed, fabricating masks with large working areas with a resolution of 2 micron within reasonable times.

The direct laser writing process is depicted in Fig. 3.1.

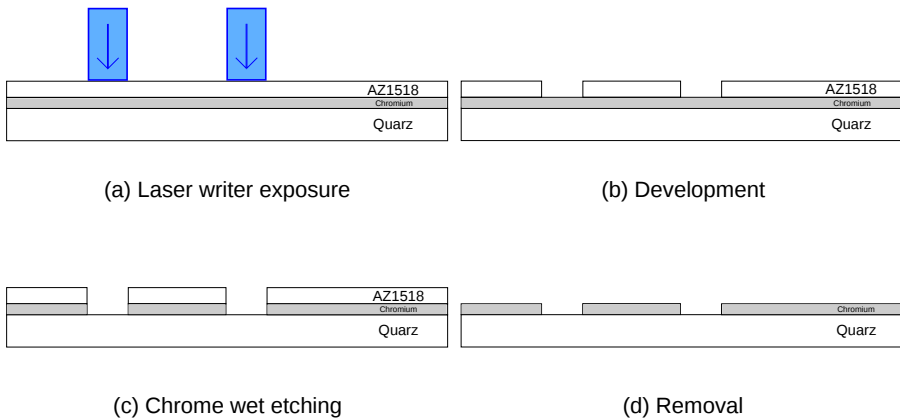


Figure 3.1: Photomask fabrication process steps: a) A mask blank is exposed to the DWL66 laser. b) Since AZ 1518 is a positive resist, the photoresist developer removes the resist from the exposed areas. c) The chromium layer is etched away in a wet chemical process. d) The remaining AZ 1518 is removed using Piranha solution.

³Shipley MICROPOSIT S1805 PHOTO RESIST

⁴AZ Electronic Materials AZ1518

⁵Shipley MICROPOSIT MF-319 DEVELOPER

Post-development

After development, the masks were exposed to a wet chemical etchant to remove the chromium in the exposed areas.

Before the masks could be used for pattern transferring, the remaining resist had to be stripped off. We found that the best way to do this is with *Piranha solution*, a mixture of sulfuric acid and hydrogen peroxide (see Fig. 3.1).

3.1.2 Pattern transfer

Substrates and chips

As a *substrate* we used p-doped 2 inch silicon wafers. The silicon was covered with an oxide layer of 400 nm by thermal oxidation. We divided each wafer into *chips*, normally square pieces of substrate in sizes of $(8 \text{ mm})^2$ to $(1 \text{ cm})^2$. If $(8 \text{ mm})^2$ are chosen, 21 chips fit onto one 2 inch wafer and may be processed in parallel.

Lift-off optimized resist stack

The process of depositing material on a prepatterned substrate and removing the parts that were deposited onto the resist covered areas is called a *lift-off*. For the lift-off fabrication of the leads for this work, a special resist stack process was developed.

The substrate is first covered with a Copolymer resist (see section 3.2), and then with the S 1805 photoresist.

The device for aligning a mask to a substrate and for exposing it to light is called a *mask aligner*. In our case, a SUSS Mask Aligner MA6 containing an intensity controlled mercury lamp was used. The mask is brought in contact with the top resist layer, which is then exposed to a fixed amount of light in the areas of mask transparency.

After exposure and development of S 1805, the Copolymer layer is etched with an oxygen plasma, turning the photoresist into an offset evaporation mask (Fig. 3.2).

3 Fabrication methods

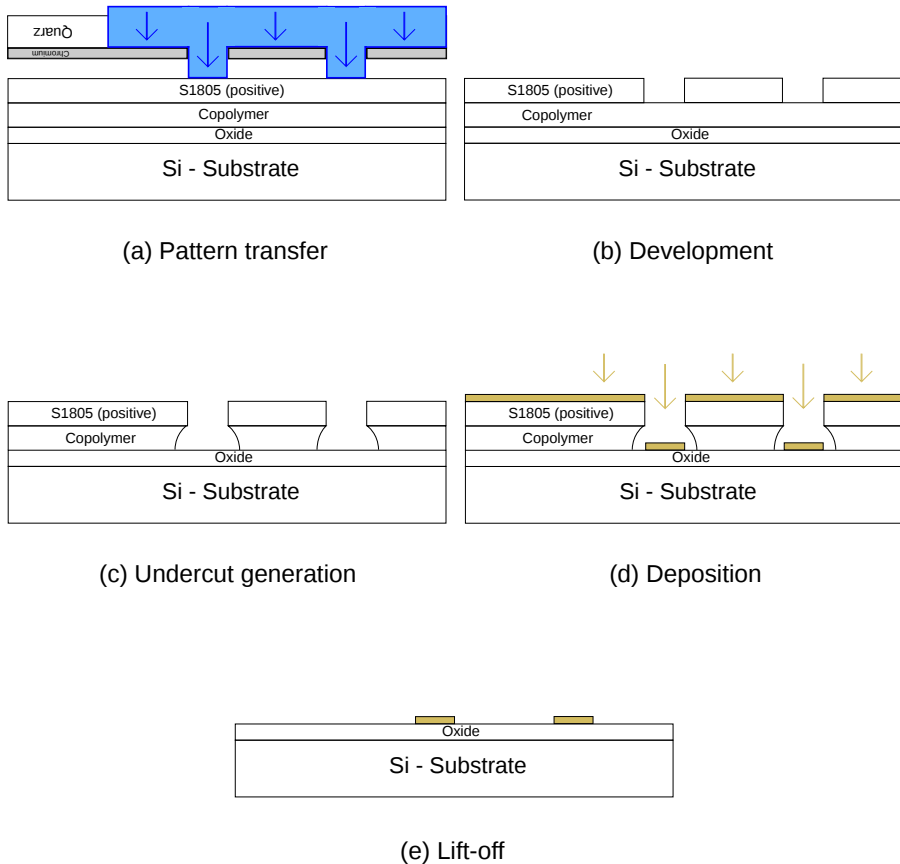


Figure 3.2: a) The mask is pressed (soft contact) against the substrate the pattern is transferred to. The whole area is illuminated. Note that the mask is flipped, which means that the pattern written to the mask has to be the mirror image of the desired result pattern. b) The exposed areas are dissolved by the developer, since S 1805 is a positive resist. c) For a good lift-off, an undercut under the patterned evaporation mask is vital. The underlying Copolymer is etched away in an oxygen plasma. d) The desired metal is evaporated, here: a thin Titanium film as a sticking layer, then 20 nm of AuPd alloy. e) The resist stack and the unwanted metal are removed using heated acetone.

3.1.3 Thin film metal deposition

Evaporation

For material deposition, we used *physical vapor deposition* (PVD). Details can be found in Ref. [Mat98].

The bond pads and leads were fabricated in a Lesker PVD 75 electron beam PVD machine. In electron beam PVD, the target material is heated locally by a beam of kiloelectronvolt electrons.

The PVD 75 offers the advantage of having several different evaporation targets that can be changed without breaking the chamber's vacuum.

Lift-off

The resist is removed with a suitable solvent. This is facilitated by the under-etched bottom layer of the resist stack, avoiding complications from metal-covered resist flanks.

3.1.4 Bond pads and leads design

The actual leads design for contacting our Aluminum nanostructures had to meet several conditions:

1. *Bond pads* are necessary to connect the leads to the macroscopic world. They need to be thick enough to survive the bonding process, and are preferably made of a noble metal not to oxidize when exposed to air.
2. The leads must be suitable to allow a thin layer of Aluminum to contact them. That means they also need to be unoxidized and not tending to form unwanted alloys when in contact with Aluminum. They must be thin enough so that the thin Aluminum layers can overcome the flanks and form a continuous film from the top of the leads to the surface of the substrate.
3. The material must form a detectable contrast when looked at with a scanning electron microscope (SEM), in order to allow alignment in the nanostructuring steps.

Material choice

Most of the material conditions are met by Gold. It is noble, and has heavy nuclei that are easily distinguished from Silicon (substrate) and Carbon (e-beam resist) in the SEM. The leads, however, can not be made of pure Gold, since it tends to form islands instead of continuous films. It is also known to form a highly resistive Aluminum-Gold alloy locally.

Both limitations can be overcome if the Gold is alloyed with Palladium. We chose to make our leads of 90% Gold and 10% Palladium (weight) (AuPd).

To enhance surface adhesion of the deposited gold or alloy, a thin Titanium *sticking layer* (a few nanometers) is evaporated as an in-situ first step, using the multi-target capabilities of the PVD 75.

Layers design

The requirements on the thickness remain incompatible. We chose to solve this by making the leads and the bond pads in subsequent lithography steps. The bond pads and alignment marks are present in both layers, while the leads near the nanostructure sights exist only in the first layer and can be made thin enough.

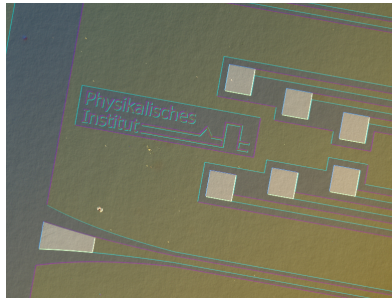


Figure 3.3: Bond pads and leads after lift-off. Grey: uncovered substrate. Dark yellow: thin Gold-Palladium layer with ground plane, DC leads (right) and microwave lead (bottom). Bright yellow: thick Gold bond pads.

3.2 Junction lithography

In this section, the methods we used to produce small (in the sense of subsection 2.3.2 and Ref. [IN91]) Josephson junctions (JJ) will be described. The last section presents an experiment on the dependence of the superconducting critical temperature of Aluminum on the film thickness.

Details of the processes can be found in the appendix D.

3.2.1 Electron beam lithography

In electron beam (e-beam) lithography, free electrons are created, accelerated and guided by electric and magnetic fields, very similar to the working principle of a scanning electron microscope (SEM). In fact, it is possible to turn an SEM into a lithography machine with a few modifications. The lithography machine we used was a Zeiss Supra 55VP, equipped with a Raith ELPHY pattern generator.

Details about electron beam lithography can be found in Ref. [MR97].

The de Broglie wavelength of a non-relativistic electron with kinetic energy eU is

$$\lambda = \frac{hc}{\sqrt{2eU \cdot m_0 c^2}}$$

An acceleration voltage U of 1 kV already produces electrons of $\lambda \approx 40$ pm, which is by far small enough to produce submicron structures. In reality, the beam diameter is usually limited by properties of the electron optics of the used SEM: electrons of slightly different velocity are diffracted differently (chromatic aberration), and the magnetic lenses are far from perfect (spherical aberrations) [MR97].

Similar to optical lithography, resists have been developed and are commercially available. A very common example is Polymethyl methacrylate (PMMA), which is used in bulk as acrylic glass. It is a positive resist for e-beam lithography.

Matters are turned more complicated compared to optical lithography by the fact that the high energy electrons create a large amount of secondary electrons in the substrate material. In addition to the dose

of high energy electrons exposing an area about the size of the electron beam itself, a micrometer-size area receives an exposure to the secondary electrons.

Resist system

We used the resist system described in Ref. [HHJ81]: a bilayer of

1. Polymethyl methacrylate (PMMA) and
2. a copolymer of methyl methacrylate and methacrylic acid (P(MMA- MAA), Copolymer).

The resist stack and the principle behind it are shown in figures 3.4 and 3.5. The Copolymer has a higher sensitivity, so the area made soluble by exposure to secondary electrons is higher than the area made soluble in the PMMA layer.

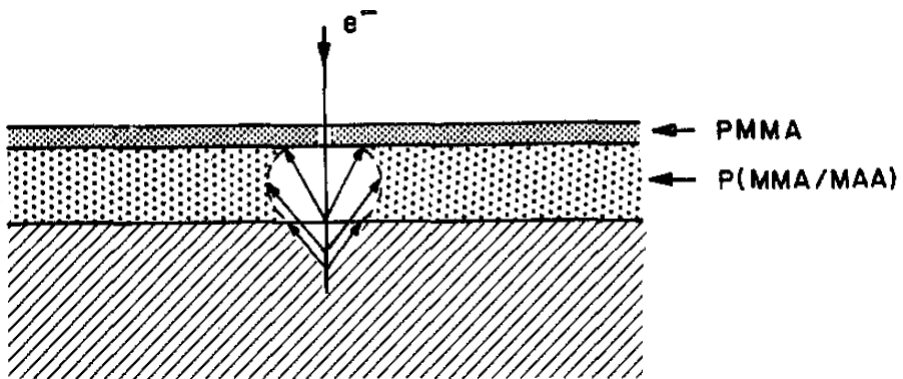


Figure 3.4: Multilayer stack, from Ref. [HHJ81]. Some secondary electrons are scattered back and expose the bottom layer, which is more sensitive than the top layer.

The developer chosen was a commercially available mixture of methyl isobutyl ketone (MIBK) and isopropanol 1:3, Allresist AR 600-56 (E 56 for short). It develops both layers in one development step.

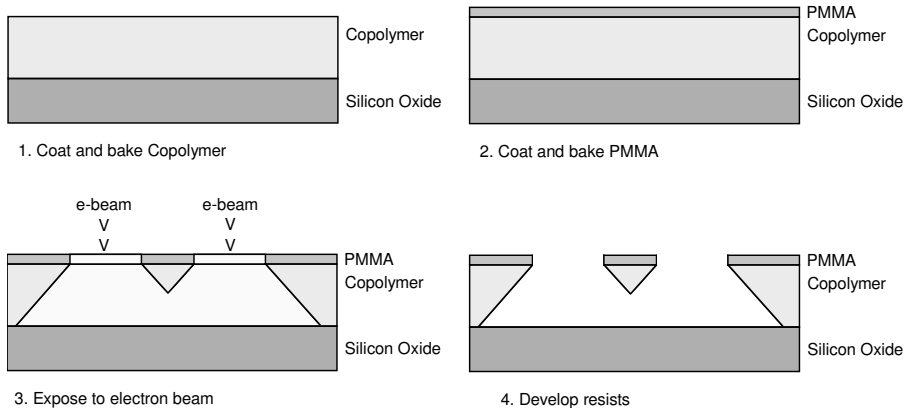


Figure 3.5: Bilayer resist application: Each layer is spin-coated on, and dried on a hotplate separately. Exposure and development: While only small structures in the top layer receive critical dose, much larger parts in the bottom layer do. After development, a Dolan bridge (picture 4, top center) is left. It is, of course, connected to resist parts in the back and the front of this segment.

A considerable undercut is created. It can be used for a single layer lift-off deposition, and we did for the Aluminum films we made for the experiments reported in subsection 3.2.4. However, if the undercut is large enough, it can be used for a process called shadow evaporation, as described in subsection 3.2.2.

Single layer Aluminum deposition

The Aluminum nanostructures were fabricated by *thermal evaporation* in a modified Oelikon Leybold Univex 300. A tungsten boat source is filled with Aluminum pieces and heated by a current. The deposition rate is measured by monitoring the resonance frequency change of a quartz crystal mounted in close proximity to the samples. Parts of a chip can selectively be shielded from deposition.

3.2.2 Shadow evaporation of Al/AlO_x/Al junctions

If the undercut generated by the patterning process is large enough, it is possible to tilt the sample for evaporation, as opposed to depositing the evaporated material perpendicularly to the substrate surface. By tilting, one shifts the position of the directly exposed areas on the surface. This is illustrated in Fig. 3.6.

The undercut of neighboring exposed top parts can overlap. Free-hanging parts of the top resist layer are created. They are called *Dolan bridges*, named after the author of references [Dol77] and [DD88].

The additional degree of freedom, i.e. the tilting angle, becomes interesting if one chooses to deposit material several times, at different angles. It is then possible to create quite complicated structures in a single patterning step. By overlapping parts of the deposited areas, nanoscale contacts can be created, e.g. superconductor- normal metal junctions.

If a layer of Aluminum is deposited, and then oxidized by exposure to gaseous Oxygen, it can be partially covered by a second layer of Aluminum, thus forming a Josephson junction. This is illustrated in 3.6.

The thickness of the oxide layer can be controlled by choosing the Oxygen pressure and the duration of the oxidation. Since the critical current density depends exponentially on the thickness of the insulator, the properties of the junctions can be tuned over a considerable range.

The full shadow evaporation process is shown in figures 3.5 and 3.6.

Most shadow evaporated nanostructures are designed such that only one of the shadows of a top layer structure is used. The other either ends up as a large overlapping second layer, or unused finger electrodes or islands. The former usually creates junctions so large they can be treated as giant electric shorts, while the latter do nothing except introducing small extra capacitances to the structures.

Some designs, however, manage to use both shadows. One example will be described in the following subsection. It is the design that has been used to create the periodic SQUID chains that were the subject of the experiments reported in chapter 4.

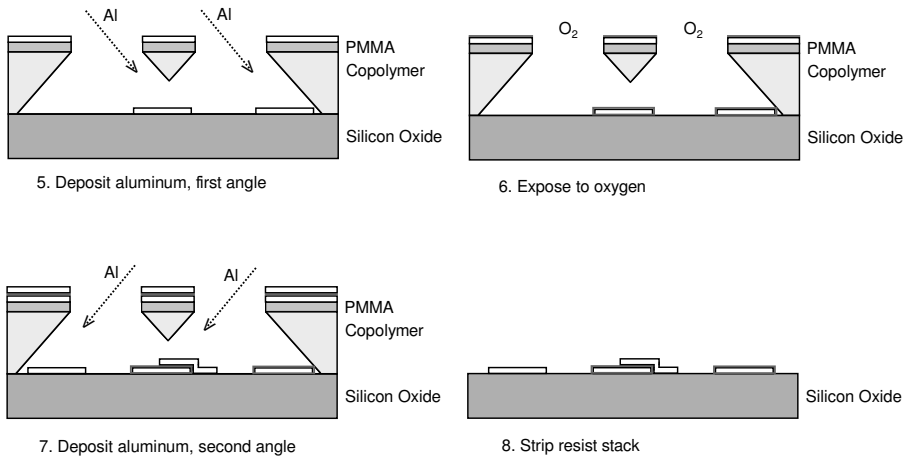


Figure 3.6: Shadow evaporation: the top layer structures serve as an evaporation mask. The sample is tilted, so the material (Al) is partially deposited underneath the resist. The resulting structures are oxidized. The sample is tilted to a different angle, so the evaporation mask is projected to a different location on the sample. The second layer of material may overlap with the oxidized surface of the first layer, forming tunnel contacts / Josephson junctions. The resist and all the material deposited on top of it is removed (lift-off).

3.2.3 Fabrication of periodic SQUID chains

To fabricate a periodic chain of Aluminum islands connected by Josephson junctions, one can use shadow evaporation in the following way: pattern a periodic chain of identical rectangles in the bilayer resist, such that the rectangles are longer than the distance between them, and the distance is short enough to result in overlapping undercuts. The result is a continuous line of uncovered substrate at the bottom, and a periodic chain of bridges crossing it.

Using this chain of Dolan bridges, one can deposit a chain of Aluminum islands along the line of uncovered substrate. If one chooses the angles correctly, it is possible to deposit the second layer such that the second set of islands is created in the gaps between the first set of islands. Because

the rectangles are longer than the distance between them, the second set of islands will overlap with the first set.

If instead of rectangles, a pattern shaped like a chain of Is (also called dog bones) is used, the islands can be made to overlap at two positions with uncovered substrate in the middle, creating a SQUID loop. This is made clear by Fig. 3.8.

The choice of the correct angle is crucial to achieving a truly symmetric chain of SQUID loops. For that, the thickness of the bottom resist layer has to be known precisely. If there is either an uncertainty in controlling the angle, or an uncertainty of the resist thickness, an asymmetry may result, which is examined in the following.

Asymmetry considerations

As it is easy to derive from Eq. 2.18, the external flux φ modulates the effective coupling energy from island to island, according to $E_J(\varphi) = 2E_J^0 \left| \cos\left(\frac{\pi\varphi}{\Phi_0}\right) \right|$, where E_J^0 is the Josephson energy of an individual junction and Φ_0 is the magnetic flux quantum. The asymmetry affects this in two ways: it changes the SQUID loop size A_L and thereby the amount of flux for a given magnetic field ($\varphi \rightarrow \varphi_{1,2}$), and it changes the junction size A_J and thereby the single junction coupling energy ($E_J^0 \rightarrow E_{J1,2}^0$):

$$E_{J1,2}(\varphi_{1,2}) = 2E_{J1,2}^0 \left| \cos\left(\frac{\pi\varphi_{1,2}}{\Phi_0}\right) \right|$$

We will describe the asymmetry by a dimensionless parameter a , such that if \overline{A}_L is the average loop size, the actual loop sizes are

$$A_{L1,2} = (1 \pm a)\overline{A}_L$$

For each nanometer of loop length increase, the junctions of the SQUID become shorter by a nanometer. That means the junction area is

$$A_{J1,2} = (1 \mp a)\overline{A}_J$$

The magnetic flux through a loop is

$$\varphi_{1,2} = B \cdot A_{L1,2} = B \cdot (1 \pm a)\overline{A}_L = (1 \pm a)\bar{\varphi}$$

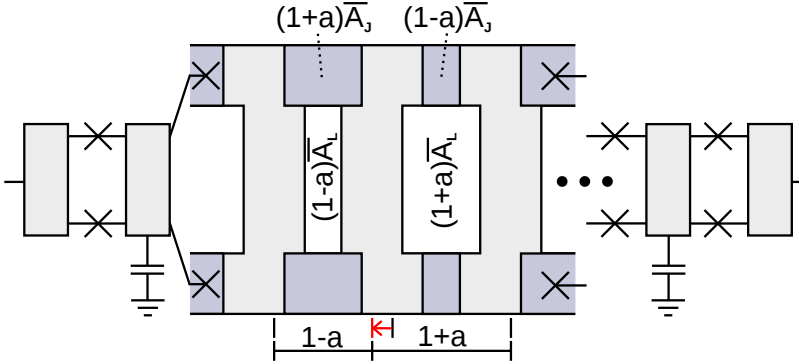


Figure 3.7: The SQUID chain in case of a slight asymmetry. The exemplary SQUID on the left has a smaller loop and bigger junctions. It is the other way round for the SQUID on the right.

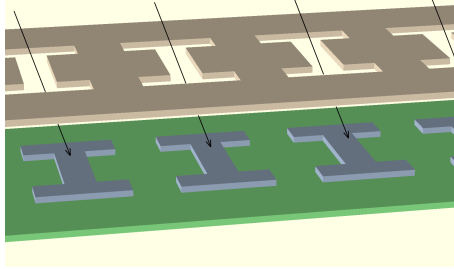
where the magnetic flux density B is controlled by our coil. We have defined an average flux per loop $\bar{\varphi}$. The Josephson energy of a single junction is

$$E_{J1,2}^0 = \frac{\Phi_0 I_{C1,2}}{2\pi} = \frac{\Phi_0 A_{J1,2} i_C}{2\pi} = \frac{\Phi_0 (1 \mp a) \bar{A}_J i_C}{2\pi} = (1 \mp a) \bar{E}_J^0$$

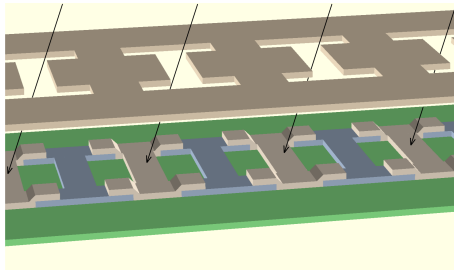
with critical current density i_C , critical currents $I_{C1,2}$, and a newly defined average Josephson energy \bar{E}_J^0 .

Now we can write the Josephson energy of a SQUID as

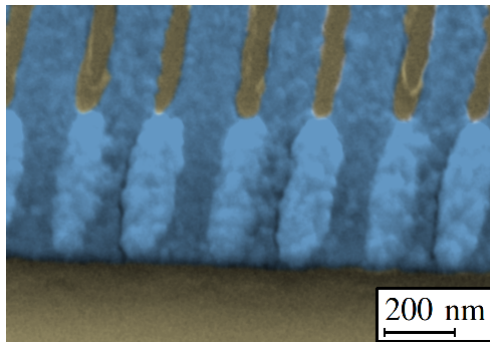
$$E_{J1,2}(\bar{\varphi}) = 2(1 \mp a) \bar{E}_J^0 \left| \cos \left(\frac{\pi(1 \pm a)\bar{\varphi}}{\Phi_0} \right) \right| \quad (3.1)$$



(a) The evaporation mask is suspended above the substrate by the undercut second layer (not shown).



(b) If the correct angles are chosen, the junctions and loops are of equal size.



(c) Colored electron micrograph of a periodic nano-SQUID chain, fabricated as a test structure.

Figure 3.8: Shadow evaporation of periodic SQUID chains.

3.2.4 Aluminum T_C dependence on the film thickness

It has been known for some time (see Ref. [MT71]) that the superconducting gap of thin Aluminum films depends on the thickness in an unusual way: the gap increases as film thickness decreases. This seems to be due to the increasing influence of surface superconductivity [SGW74].

The fact that the gap can be tuned by film thickness can be used to trap quasiparticles [Fer+06], similar to the normal metal QP traps described in subsection 2.2.2.

Since the exact size of the gap depends on the circumstances of film deposition, an experiment was carried out to determine the thickness dependence in our case⁶.

Fabrication

The Aluminum structures were designed to utilize the AuPd leads chips that had been designed with Josephson junction arrays in mind. All leads to a given site on the chip were used to ensure the possibility of 4-point measurements. Per site, four Aluminum stripes were made.

The width of the Aluminum stripes is 300 nm. We fabricated Aluminum stripes of 20 nm and 40 nm thickness on the same chip. The stripes were defined by e-beam lithography during the same writing step, as reported in the previous subsections and appendices C and D. To produce structures of different thickness, each site was exposed to the evaporated Aluminum separately while the other was covered by a shadow mask.

A picture of the finished structures can be seen in Fig. 3.9.

Measurement

The sample chip was cooled down in a ³He refrigerator. Temperature was controlled by electric heating. The control loop produced fluctuations of about 25 mK.

A four-point measurement setup was chosen. A Keithley 2636 A Source Meter was used to supply a current through the thin Aluminum stripe. The

⁶The experiment has been reported as part of the Bachelor thesis of H. Zwickel, see Ref. [Zwi12].

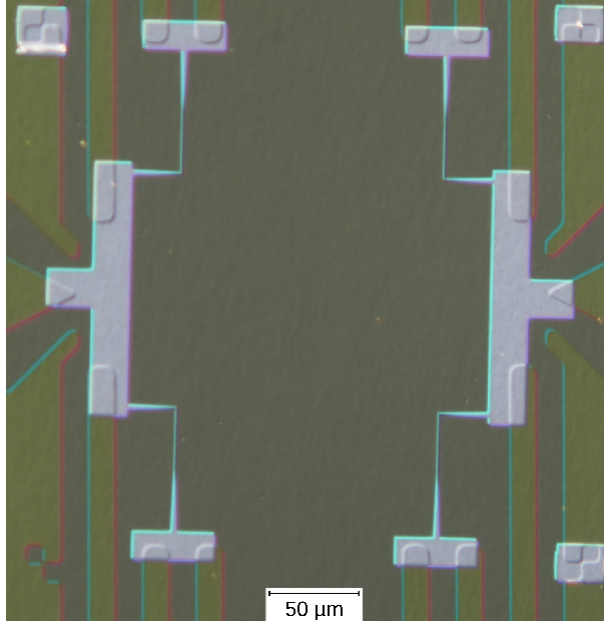


Figure 3.9: Aluminum nanostructures for the T_C experiment. The darkest areas are uncovered substrate, dark yellow are the AuPd contact lines, bright grey is Aluminum. Per writefield four 300 nm wide Aluminum strips were created. In the corners, the resist was developed because it was viewed with the SEM during alignment.

voltage drop was measured with a HP 34401A multimeter. The voltage resolution of the setup was $1 \mu\text{V}$.

For each layer thickness sample, two stripes were selected, contacted and measured. The maximum current the stripe could carry before a voltage drop was detected was determined at various temperatures between 300 mK and 1.4 K. The maximum current approaches zero as the temperature approaches T_C .

Result

The results of the measurement are shown in Fig. 3.10(a).

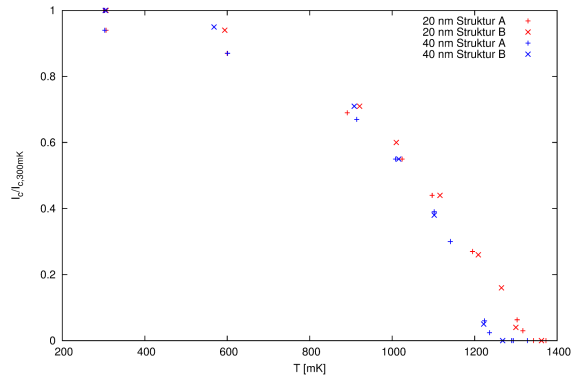
The transition temperature of the structures of the same size is very similar, while the film thickness clearly influences the transition. The thinner film has a measurably higher critical temperature.

For both thicknesses, a critical temperature has been extrapolated from the data. Based on different electron-phonon interactions at the surface and in the bulk, Sixl et al. [SGW74] have used the following equation for $T_C(d)$:

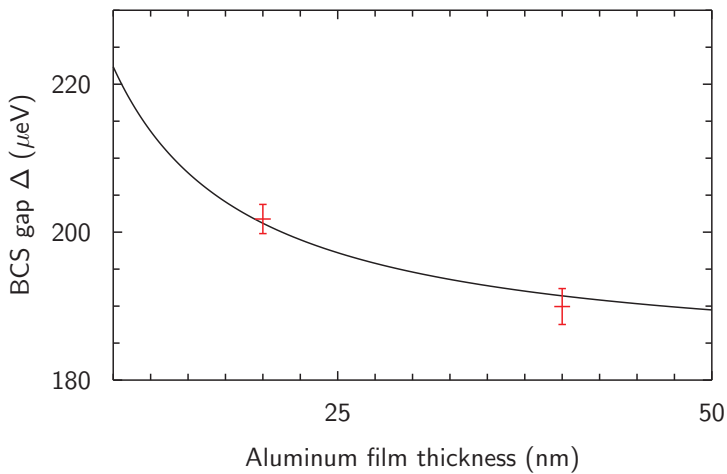
$$T_C(d) = T_{C,0} \exp\left(\frac{k}{d}\right) \quad (3.2)$$

With $T_{C,0} = 1.2 \text{ K}$ and $k = 2 \text{ nm}$, our results are well described. Using the BCS relation (Eq. 2.9) between T_C and Δ and Eq. 3.2, we can estimate the gap of an Aluminum film of a given thickness prepared under similar conditions (see Fig. 3.10(b)).

3 Fabrication methods



(a) Normalized maximum supercurrent through the Aluminum stripes at different temperatures. The maximum current through the 40 nm stripes drops at significantly lower temperatures. From Ref. [Zwi12].



(b) Superconducting gap depending on the Aluminum thickness. In addition to the two resulting points, the prediction by Sixl et al. is shown for a characteristic length $k = 2$ nm.

Figure 3.10: Results of the thickness dependent T_c experiment

4 Measurements

Remember kids, the only difference between Science and screwing around is writing it down.

Adam Savage, MythBusters

In this chapter, the charge transport measurements that were conducted during this work are presented.

In order to observe charging effects in superconducting nanostructures, the energy fluctuations in the electric and thermal environment must be smaller than the charging energy. In section 4.1, our low temperature setup and the low-noise electrical measurement instrumentation are described.

The current-voltage characteristics of the examined samples differ in some details, but they share some general properties which are shown in section 4.2. Some of these properties - namely, the behavior at large voltages - is used to estimate the charging energy of the islands and the Josephson energy of the SQUIDs.

This work focuses on the conductance of Josephson junction chains in the Coulomb blockade regime. Applying a voltage in the millivolt range to the chains activates a charge transport mechanism that is shown to be the result of incoherent tunneling. Section 4.3 reviews previous results on this, and shows this regime to exist in the sample that is examined in section 4.5.

In subsection 3.2.4, a significant dependence of the superconducting gap of Aluminum on the film thickness is shown. In section 4.4, measurements of an array that employs this property are presented.

Charge transport in a Coulomb blockaded array can be activated by thermal fluctuations. Section 4.5 deals with the length-, temperature- and coupling strength dependence of the thermally activated zero bias. The model presented in section 2.3 is used to interpret the results.

4 Measurements

Some of the results presented in section 4.3 and section 4.5 have been published elsewhere [Zim+13].

Section 4.6 presents a set of measurements exploring the dependence of the zero bias conductance on flux noise. External flux noise is applied, and the change in conductance analyzed.

4.1 Experimental setup

4.1.1 Low temperature environment

All experiments took place inside an antique Kelvinox dilution refrigerator. In several steps, the temperature is lowered first from room temperature to the temperature of liquid Nitrogen and liquid Helium at ambient pressure (77 K and 4.2 K). Then it is lowered further to the temperature of liquid Helium at low pressure – by evaporating ^4He from the so-called 1 K pot – to around 1.5 K. Finally, a dilution refrigeration unit lowers the temperature to the minimum temperature the cryostat can reach, typically between 15 to 20 mK. A review of the working principle of a dilution refrigerator can be found in [Lou79].

For the measurements reported in section 4.5, the temperature of the dilution stage has to be controlled. This is achieved by heating the stage by sending a current through a resistor that is thermally coupled to the mixing chamber of the refrigerator. The dilution unit is kept running normally.

The temperature of the mixing chamber is continuously measured by monitoring the calibrated resistance of a Ruthenium Oxide thermometer installed there. The resistance is measured using a Picowatt AVS47 AC resistance bridge. The heating power dissipated at this stage is controlled by a voltage applied from a NI USB 6259 digital-to-analogue converter (DAC), through low pass filters.

The temperature is controlled by a computer program that reads out the AVS bridge and controls the DAC. It implements the well established method of proportional-integral-derivative (PID) controlling¹. Temperature stabilization was better than $\Delta T_{\text{RMS}}/T = 0.1\%$ for all reported measurements.

The temperature control for this setup was implemented and tested during the time of this work. Some technical notes on the details can be found in the appendix B.

¹For a review of the method, see e.g. Ref. [Ast95].

4.1.2 Wires and filters

To contact the samples, preexisting DC lines to the mixing chamber stage were used. These lines are low-pass filtered both at room temperature and at the 1K stage. At the room temperature stage, commercially available π -filters² are installed on the measurement lines. These filters reduce electromagnetic noise from the room temperature environment.

At the 1K stage, T-type RC low-pass filters with a bandwidth of 40 kHz are inserted into all the lines. The resistors add up to a total resistance of about 500 Ω per line. At this point, the charge carrier temperature is reduced to the temperature of the 1K stage, and thermal noise from the room temperature cable is filtered.

At the mixing chamber stage, additional custom low-pass metal powder filters[LU08] are installed. The powder filters have a -3 dB cutoff frequency of 1 MHz. They prevent high frequency noise, that may have passed through the lumped element filters, from influencing the sample.

To estimate the Nyquist noise (see Ref. [Nyq28]) at the sample, it is assumed each line has a resistance of 50 Ω at 300 K. That noise is filtered by the T-type RC filter at 1.5 Kelvin. The noise voltage is $U_{\text{noise}}^{300\text{ K}} = \sqrt{4k_B T R \Delta f} \approx 0.2\ \mu\text{V}$.

Neglecting the capacitance of the T filter, a worst case estimate of the thermal noise from the 500 Ω at 1.5 K is to assume that it is only limited by the powder filters. Then, the noise voltage is $U_{\text{noise}}^{1.5\text{ K}} \approx 10\ \text{nV}$. This much lower than the room temperature noise, and it is neglected.

The resistance of a typical array is 1 M Ω or more, so the thermal noise current is on the order of 0.2 pA.

Between the filters and connection points, associated line pairs are realized as twisted pairs, to reduce electromagnetic interference. An overview over the wiring and filtering can be seen in Fig. 4.1.

4.1.3 Instruments

All measurements reported in sections 4.2 through 4.5 were performed with the setup shown in Fig. 4.1. The bias voltage is controlled by

²Type SCI 52-970-209-TB0 9724, 3 dB cut-off at 700 kHz

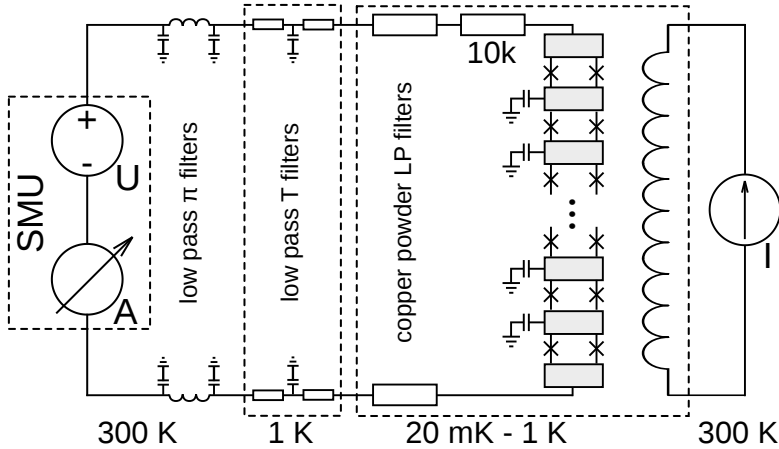


Figure 4.1: Experimental setup: A source-measurement unit is used to supply the voltage bias to the sample and simultaneously measure the current. The signal is low-pass filtered symmetrically at different stages. A magnetic flux bias is supplied to the SQUIDs from a separate current source.

a source-measurement unit (SMU)³ which also measures the resulting current. The second channel of the SMU is used to control the flux bias coil. The setup is capable of measuring currents up to a resolution of $I_{\text{RMS}} \approx 200$ fA.

³Keithley Model 2636A Dual-channel System SourceMeter

4.2 Sample characterization

In this section, typical charge transport properties of SCJJAs are described⁴. A method to estimate microscopic properties from the large bias current-voltage characteristics is described, and the samples are introduced.

4.2.1 Typical current-voltage characteristics

Depending on the number of SQUIDs and the ratio of Josephson energy E_J to charging energy E_C , the arrays typically exhibit a macroscopic Coulomb blockade (CB), see Fig. 4.2 and e.g. Ref [HD96]. The longer the array and the lower the E_J/E_C ratio, the more pronounced this feature becomes. Under favorable conditions, the voltage range in which no measurable current flows reaches several millivolts. Transport can be activated by thermal fluctuations (G_T), as is discussed in detail in section 4.5.

Above a switching voltage V_{sw} , the arrays switch from the CB state to a branch of finite conductance [HD96]. At low temperatures and very low external voltage noise, a hysteresis can be observed: once on the branch of finite conductance, the array will remain conducting even at voltages below V_{sw} , and return to the CB state only if the voltage is lowered below a retrapping voltage V_{re} . The hysteresis in the samples IFP11-N has been analyzed in Ref. [Fie11].

In some arrays, the branch of finite conductance above V_{sw} exhibits a constant differential conductance (G_V) over a considerable voltage range. The dependence of this conductance on the external flux has been observed by R. Schäfer et al. [Sch11] and it has been shown to be proportional to E_J^2 . Section 4.3 reports measurements that confirm those findings.

As the voltage is increased further, the differential conductance decreases, and the absolute conductance rises very slowly. At sufficiently low effective E_J (approaching a flux bias of $\Phi_0/2$), a sudden increase in conductance can be seen at a voltage of about $2N\Delta/e = V_{gap}$. It is associated with a voltage drop across each junction large enough to generate

⁴An overview can be found e.g. in Ref. [Fie11].

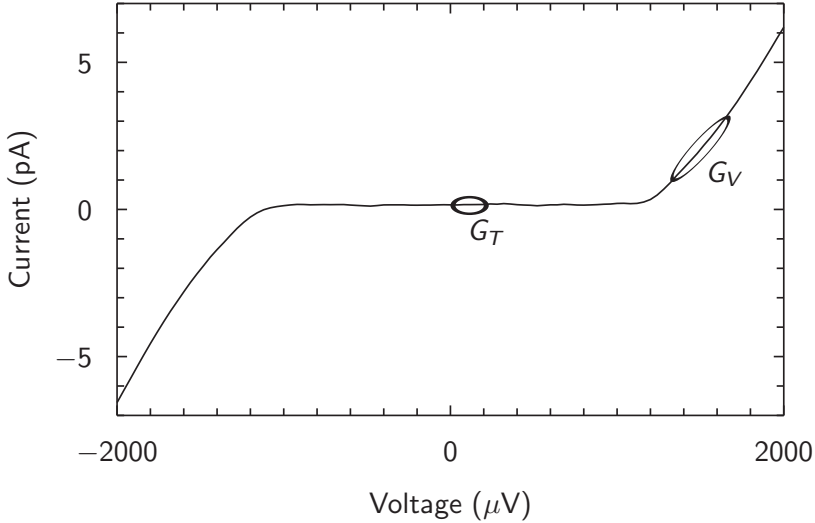


Figure 4.2: IV of IFP11-255 at an external flux of about $\Phi_0/2$ per SQUID, measured at base temperature. The regions of voltage-activated conductance G_V and of thermally activated conductance G_T are marked.

quasiparticles. In the case of significantly different Δ in the two shadow evaporation layers, this property is modified, as is reported in section 4.4.

Above the gap voltage, one always finds a flux-independent branch of constant differential conductance $R_{t,N}$. It appears to be the high-voltage limit, as it always continues up to the highest voltages applied. A least square fit of this region is shown in Fig. 4.3. The curve differs from classical ohmic behavior by a small offset voltage V_{off} . It is this behavior at high voltages that is used to estimate the microscopic properties of each sample, as is described in the following subsection.

4.2.2 Charging energy and tunneling resistance estimation

Estimation from the high voltage properties

In the limit of high voltages and (relatively) high currents, all junctions are in the resistive state, and the voltage drop is uniformly distributed along the array. Since the voltage is larger than the gap voltage on each

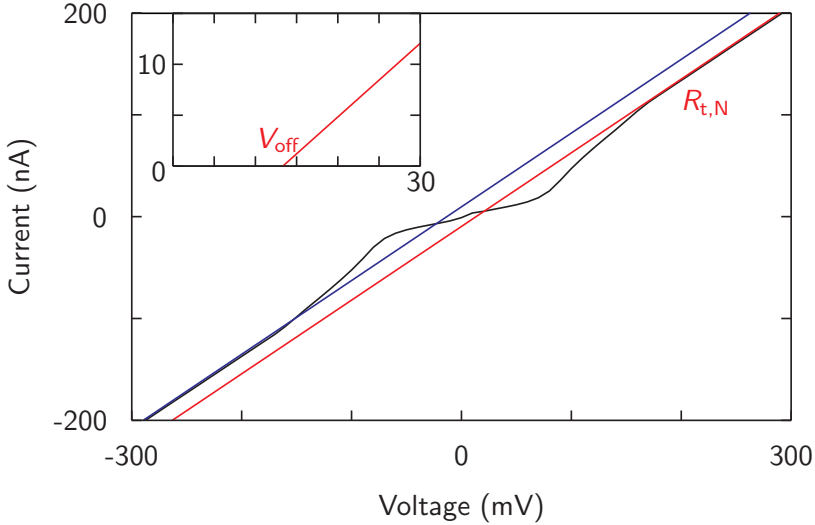


Figure 4.3: Large voltage bias behavior of sample IFP11-255. Characteristics were measured at base temperature. Inset: the linear fit of the high voltage conductance reveals an offset voltage V_{off} .

junction, transport is governed by quasiparticles. This is in agreement with the fact that no flux dependence can be observed at these voltages.

For this estimation, the transport of quasiparticles across a series of uniformly biased small capacitance tunnel junctions is assumed to follow the model described in subsection 2.3.2. That means that one can interpret the observed resistance $R_{t,N}$ as the sum of the individual normal tunneling resistances, $R_{t,N} = N \cdot R_t$. The offset voltage V_{off} is the sum of the individual charging voltages, $V_{\text{off}} = N \cdot e/2C$, necessary to charge the individual junction capacitance C .

Now it is straightforward to derive the quasiparticle charging energy E_C^{qp} and the initial Josephson energy E_J^0 . The charging energy is simply

$$E_C^{\text{qp}} = \frac{e^2}{2C} = \frac{e \cdot V_{\text{off}}}{N} \quad (4.1)$$

To estimate the initial Josephson energy, Eq. 2.14 is employed, connecting the normal tunnel resistance with the junction's critical current:

$$I_c(T) = \frac{\pi}{2e} \frac{\Delta(T)}{R_n} \tanh\left(\frac{\Delta(T)}{2 \cdot k_B T}\right)$$

At low temperatures ($T \ll T_c$) one can approximate $\Delta(T) \approx \Delta(0)$, which allows:

$$\begin{aligned} \tanh\left(\frac{\Delta(T)}{2 \cdot k_B T}\right) &\approx \tanh\left(\frac{\Delta(0)}{2 \cdot k_B T}\right) \approx \tanh\left(\frac{T_c}{T}\right) \approx 1 \\ \Rightarrow I_c(T) &\approx I_c(0) = \frac{\pi}{R_n} \frac{\Delta(0)}{2e} \end{aligned}$$

The Josephson energy is then:

$$E_J^0 = \frac{\Phi_0}{2\pi} I_C \approx \frac{\Phi_0}{2\pi} I_C(0) = \frac{R_Q}{2} \frac{\Delta(0)}{R_n} \quad (4.2)$$

$R_Q = \frac{h}{4e^2} = 6.45 \text{ k}\Omega$ is the resistance quantum.

Charging energy estimation by junction size

An alternative method to estimate the SQUID charging energy is by measuring the junction size, and multiplying it by a specific capacitance from literature. The junction size can be determined from SEM pictures of control structures with a reasonable accuracy. For junctions tens of μm^2 big, a specific capacitance of $c_s = (45 \pm 5) \text{ fF}/\mu\text{m}$ is reported. However, for ultrasmall junctions on the order of $0.01 \mu\text{m}$,

$$c_s \approx 200 \text{ fF}/\mu\text{m}$$

seems to be a much better approximation [WH01]. Since the junctions examined in this work are of that size, that value will be used for the estimation.

4.2.3 Overview of samples

The array parameters, estimated as described above, are shown in table 4.1.

Soli06a and b

Four arrays were fabricated on one chip with $N=255$ SQUIDs each. Two were measured in the course of this work. The coulomb blockade is pronounced without the application of magnetic flux.

The junction area is estimated as $0.01 \mu\text{m}^2$.

KTH2011chip1

The sample KTH2011chip1 has a total of 2888 SQUIDs. During shadow evaporation, the thickness of the Aluminum layers was chosen to be different, 12 nm and 24 nm. According to Fig. 3.10(b), this corresponds to gaps of $215 \mu\text{eV}$ and $195 \mu\text{eV}$, a notable difference.

The junctions have an area of $0.1 \mu\text{m} \cdot 0.2 \mu\text{m}$.

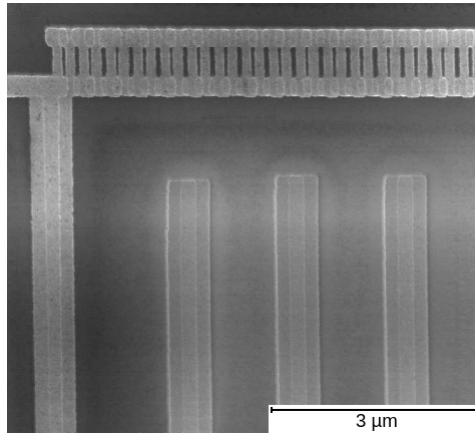


Figure 4.4: SEM micrograph of sample KTH2011chip1. A bias comb was placed next to the array.

KTH2011chip1 was fabricated with a bias comb. A micrograph of it is shown in Fig. 4.4. The distance between gates and array is 1120 nm, the distance between the gates is 900 nm. Each gate is $w = 700$ nm wide.

From the numerical simulations of the capacitances in subsection 2.1.2, one can estimate the inter-gate capacitance per unit length as

$$C_g/l \approx 35 \text{ aF}/\mu\text{m}$$

If the capacitance of the gate electrodes to ground is estimated as the capacitance of a plate capacitor, $C_{g,0}$ per unit length is

$$C_{g,0}/l \approx \epsilon_0 \epsilon_r w/d = 0.15 \text{ aF}/\mu\text{m}$$

since the chip is $500 \mu\text{m}$ thick.

The capacitance between the gate electrode and the center island is, from the calculations in subsection 2.1.3, estimated to be

$$C_{g,i} \approx 1.5 - 3 \text{ aF}$$

With a ratio of islands to gate electrodes of $n_i = 8$, the effective bias voltage screening length is:

$$n_i \Lambda_g = n_i \sqrt{C_g/C_{g,0}} \approx 120$$

Since it is much smaller than the total array length, no significant effect can be expected.

IFP11-N

A set of arrays has been fabricated on the same chip with the same design parameters, only differing in the number of junctions. The longest two exhibit a Coulomb blockade at sufficient magnetic flux. The lengths are $N=59$ and $N=255$. Two additional arrays of $N=39$ and $N=19$ have also been fabricated on that chip, but are not subject of this work. The junction area is estimated to be $A_J = 0.018 \mu\text{m}^2$. The fabrication and characterization of this sample has been described in Ref. [Fie11].

| Sample | N | R_N (M Ω) | E_J^0 (μ eV) | E_C^{qp} (μ eV) | E_C^a (μ eV) | CB at E_J^0 ? | E_J^m (μ eV) |
|--------------|------|---------------------|---------------------|------------------------|---------------------|-----------------|---------------------|
| IFP-Soli06a | 255 | 3.534 | 47 | 216 | 20 | yes | 47 |
| IFP-Soli06b | 255 | 1.44 | 114 | 96 | 20 | yes | 114 |
| KTH2011chip1 | 2888 | 4.780 | 390 | 11 | 10 | no | - |
| IFP11-255 | 255 | 1.122 | 117 | 37 | 11 | no | ≤ 16 |
| IFP11-59 | 59 | 0.195 | 160 | 29 | 11 | no | ≤ 3 |

Table 4.1: The samples and parameters used for the presented measurements. N is the number of islands, R_N the high bias voltage differential resistance at base temperature. E_J^0 is the Josephson energy without an external magnetic field, and E_C^{qp} the quasiparticle charging energy; both are estimated from the high bias properties. E_C^a is the charging energy estimated from the junction area. In some cases an external magnetic field was used to reach the Coulomb blockade regime; then E_J^m is the estimated effective Josephson energy range.

4.2.4 Estimation of the SQUID inductance

In section 2.2.1, it was shown that the DC SQUIDs can be regarded as tuneable single Josephson junctions, with a critical current tuneable from twice the single junction's I_C to zero. This approximation only holds if the geometric inductance of the loop is much smaller than the Josephson inductance, or $\beta_L \ll 1$ (see Eq. 2.19).

As an example, β_L is estimated for the sample IFP11-255. The geometric inductance is estimated to be $L = 23 \text{ pH}^5$.

Since $E_J = 117 \text{ } \mu\text{eV}$, the total critical current is $I_C = 2\pi E_J / \Phi_0 = 58 \text{ nA}$. This means:

$$\beta_L = \frac{2\pi I_C L}{\Phi_0} = 4 \cdot 10^{-3} \ll 1$$

The kinetic inductance per square (see e.g. Ref. [Sch97]) of a thin film is $L_{\text{sq}}^K = 4\pi\lambda^2/d$. $\lambda = 50 \text{ nm}$ is the London penetration depth of Aluminum, and d is the film thickness, 30 nm in this case. This means $L_{\text{sq}}^K = 105 \text{ fH}$, so with a an estimated number of 32 squares, one arrives at

$$L^K = 3.4 \text{ pH}$$

which is an order of magnitude lower than the geometric inductance, and can safely be ignored.

⁵S. Butz used FastHenry, a free inductance calculation tool from MIT. The SQUID geometry was estimated from SEM images to be $320 \text{ nm} \times 1700 \text{ nm}$ outer size, $80 \text{ nm} \times 1360 \text{ nm}$ inner size, layer thickness 30 nm .

4.3 Voltage-activated conductance

Above a flux-dependent switching voltage, the SQUID arrays exhibit a regime of constant differential conductance G_V (see Fig. 4.2). Schäfer et al. [Sch11] have investigated the dependence of G_V on the external flux, from which the dependence on the effective Josephson energy of the SQUIDs can be calculated. G_V has been determined for various external flux values, spanning more than $3\Phi_0$.

As shown in Fig. 4.5, the conductance has a \cos^2 flux dependence:

$$G_V \propto \cos^2(\pi\phi/\Phi_0) \quad (4.3)$$

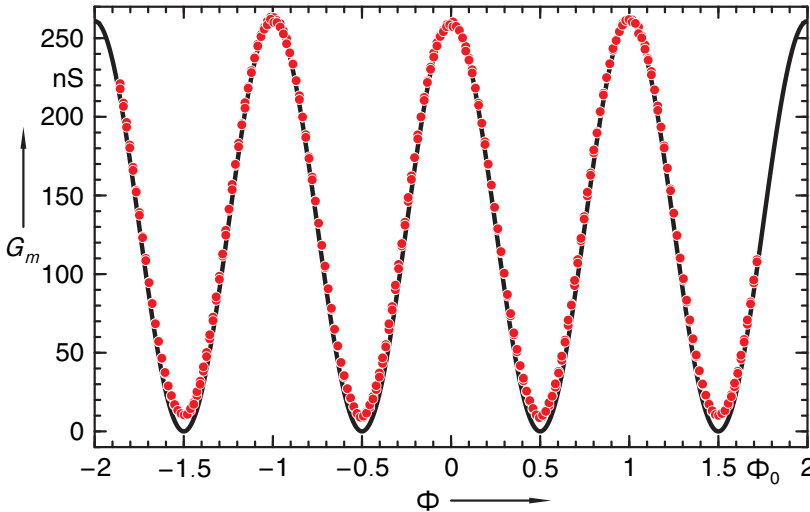


Figure 4.5: Flux dependence of the voltage-activated conductance, courtesy of R. Schäfer [Sch11].

It follows directly from Eq. 2.18 that:

$$G_V \propto E_J^2 \quad (4.4)$$

In the spirit of Eq. 2.43, this can be interpreted as a signature of incoherent tunneling of Cooper pairs in the array. Since the voltage distribution

in the case of finite voltage and finite current is non-trivial, detailed calculations are challenging. This can be taken as further motivation for zero bias voltage conductance measurements, which are more accessible theoretically.

4.3.1 Sample IFP11-255

The regime of constant differential conductance G_V was measured in sample IFP11-255. For all values of external flux, the sample exhibits a constant differential conductance in the bias voltage range of 1.3 - 1.7 mV (Fig. 4.6). G_V was calculated by a least square fit of the IV in that range.

The amount of flux penetrating each SQUID for a given magnetic field can be estimated by the loop area. Once the flux dependence of G_V is established, the more precise way to determine the amount of flux per SQUID is to find the minimum of G_V . In this and the following chapters, all flux values have been calculated in this fashion.

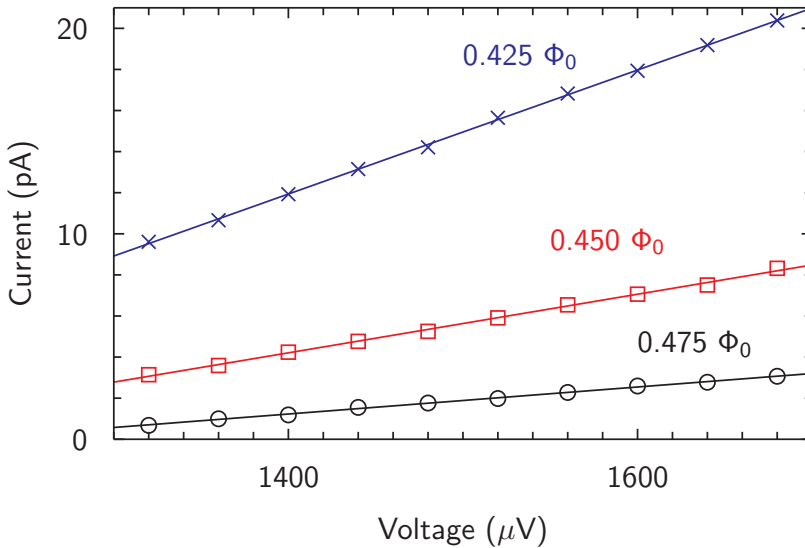


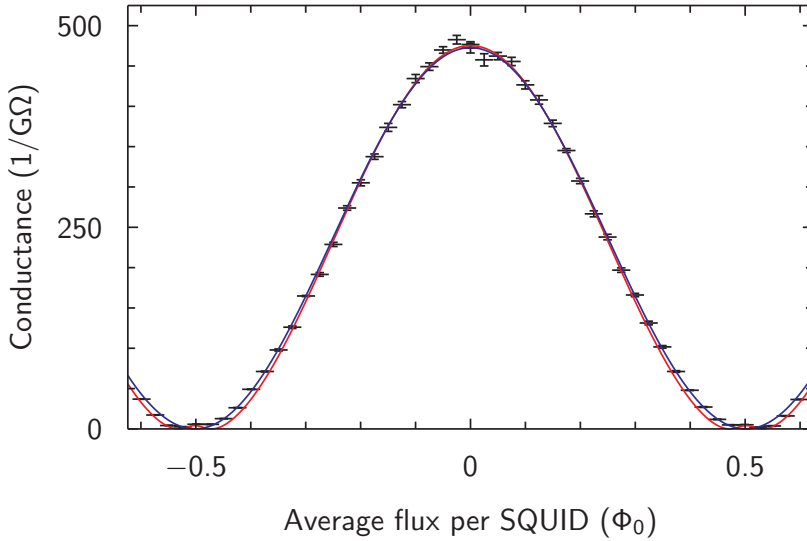
Figure 4.6: In the bias voltage range of 1.3 - 1.7 mV, sample IFP11-255 exhibits a constant differential conductance. This range is used to determine G_V .

The resulting flux-dependent conductance $G_V(\phi)$ is shown in Fig. 4.7(a). G_V clearly follows Eq. 4.4. A closer look at the minimum reveals a double-minimum structure (Fig. 4.7(b)). The double-minimum can be reproduced qualitatively by assuming an asymmetry $a = 0.06$ according to Eq. 3.1. However, since the quantitative agreement of the asymmetric fit is not better than the symmetric one, all further analysis will assume the symmetric case.

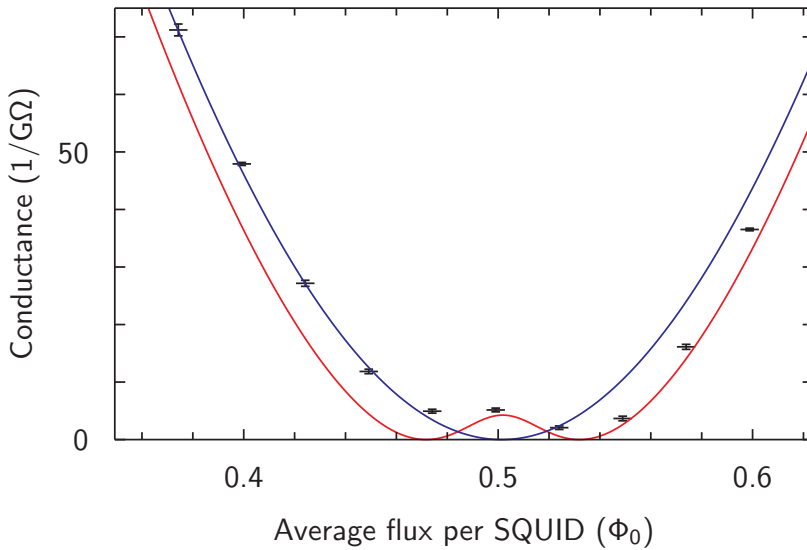
4.3.2 Sample KTH2011chip1

The KTH2011chip1 sample exhibits a Coulomb blockade for flux biases larger than $0.44\Phi_0$. As is shown in Fig. 4.8, the voltage at which a constant differential G_V can be observed is higher than in the previously discussed samples. The voltage range of 3 mV to 5 mV was taken for the least square fit of G_V . One might speculate that this effect is connected to the larger effective bias voltage screening length (see subsection 4.2).

At external fluxes of less than $0.4\Phi_0$ per SQUID, the conductance is larger than estimated by the \cos^2 -fit of the Coulomb blockaded regime (see Fig. 4.8). This indicates that the coupling between the islands is approaching a regime of coherent transport, as might be expected for the quite large $E_J(\varphi = 0)/E_C$ ratio.



(a) Voltage-activated conductance, total



(b) Voltage-activated conductance, minimum

Figure 4.7: Voltage-activated conductance G_V of sample IFP11-255. A least-square fit with an odd/even asymmetry ($a = 0.06$, red) and without an asymmetry (blue) are shown.

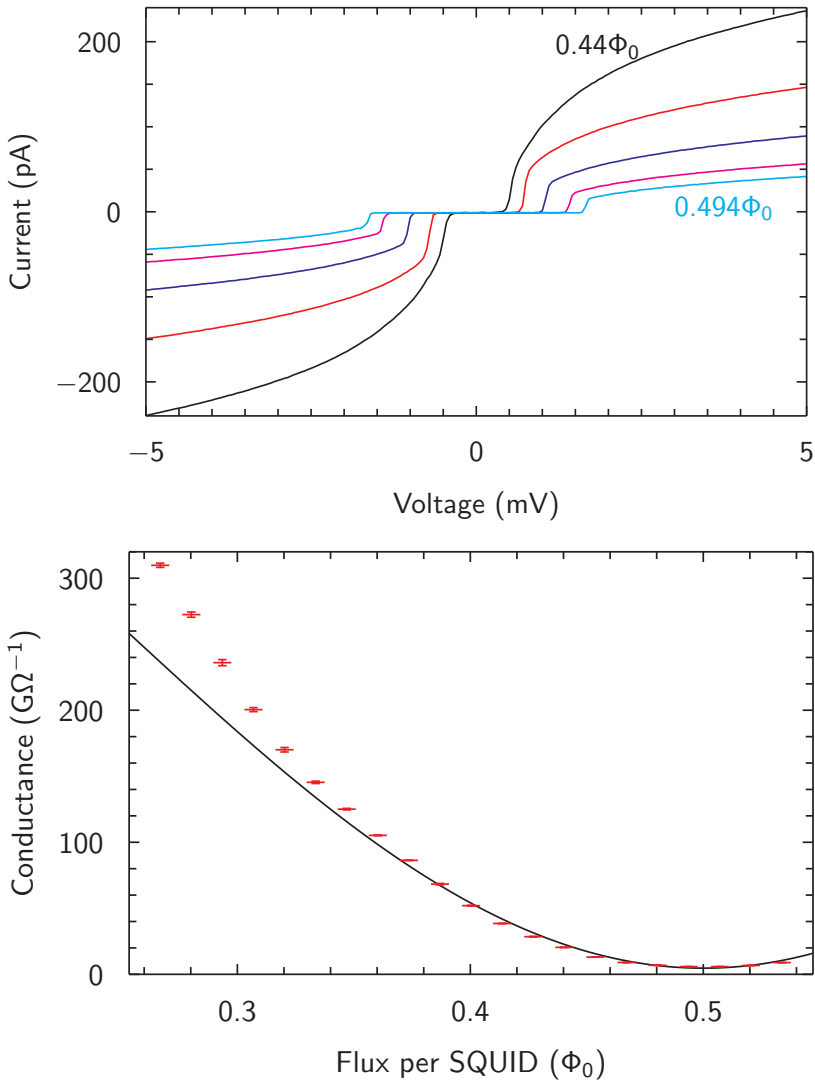


Figure 4.8: At sufficiently large external flux, the sample KTH2011 is Coulomb blocked. Near $\Phi_0/2$, G_V follows the \cos^2 dependence. With increasing E_J , the conductance is larger.

4.4 Dual gap feature

The sample KTH2011 has been designed with very different superconducting gaps in the two Aluminum layers, using the dependence of the gap on the film thickness.

In a voltage-biased bulk SIS contact, a quasiparticle current is created once the bias voltage reaches $(\Delta_1 + \Delta_2)$. Then, the energy is large enough to produce a hole-like quasiparticle in one electrode and an electron-like in the other. Therefore one expects to see a gap feature at:

$$V_{\text{gap}} = N \cdot (\Delta_1 + \Delta_2)/e = 2N \cdot (\bar{\Delta})/e \quad (4.5)$$

Suppose $\Delta_1 < \Delta_2$. Ramping up the voltage, the voltage $V_1 = 2N\Delta_1/e$ is reached before V_{gap} . At that voltage, every other island is supplied enough energy to break cooper pairs. The quasiparticles generated by this would preferably tunnel in the direction of the voltage drop, giving rise to a quasiparticle current. A quasiparticle current can be expected to be independent of the external flux.

Current-voltage curves were measured at bias voltages in the range 600 to 1000 mV, varying the external flux.

Results

Fig. 4.9(a) shows the high bias voltage characteristics of the sample. Above 860 mV, the transport is completely independent of the external flux. The linear branch is switched to a flux-dependent voltage.

Depending on the flux bias, a second flux-independent branch can be reached. Switching occurs at 720 mV for all $\phi_{\text{ext}} < 0.2\Phi_0$. The lower voltage flux-independent branch changes into the high voltage limit branch at 775 mV.

The lower voltage branch has a total differential resistance of 2.0 M Ω , and an offset voltage of 478 mV. For the higher voltage branch, one finds a resistance of 4.78 M Ω and an offset voltage of 31 mV.

The gap voltage is taken to be the $\Phi_0/2$ -limit of the gap feature switching (see Fig. 4.9(b)), which is 855 mV. The average gap is, according to Eq. 4.5:

$$\bar{\Delta} = 148\mu\text{eV}$$

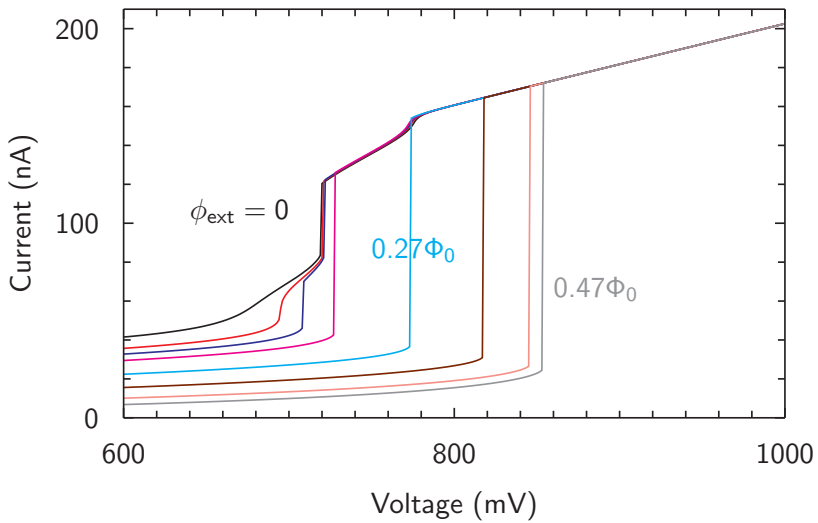
Assuming that the first switching voltage, 720 mV, corresponds to $V_1 = 2N\Delta_1/e$, one arrives at $\Delta_1 = 125\mu\text{eV}$, and immediately $\Delta_2 = 171\mu\text{eV}$.

Discussion

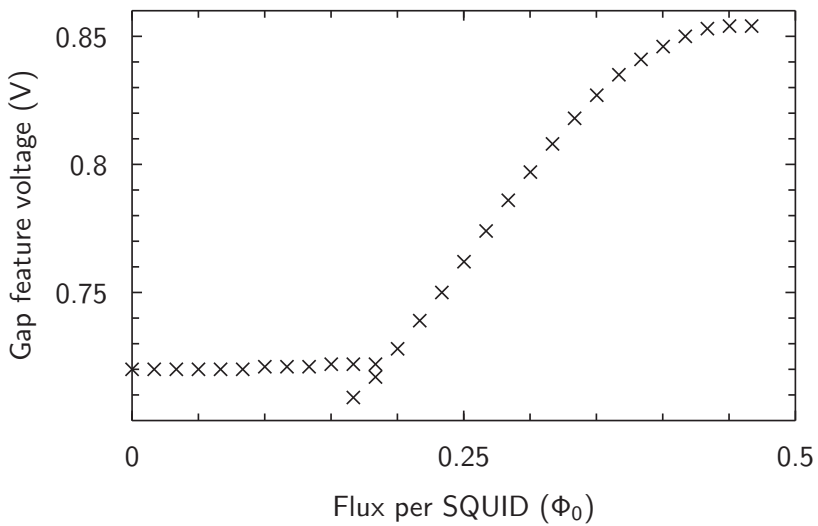
From the high voltage limit branch, a tunneling resistance of $R_t = 1.66\text{ k}\Omega$ and a quasiparticle charging energy of $E_C^{\text{qp}} = 11\mu\text{eV}$ had already been extracted. This charging energy agrees with the estimate extracted from the junction area.

The second branch shows a differential resistance that is roughly half of that of the high voltage limit. Its offset voltage, $V_{\text{of}} = 165.5\ \mu\text{V} \cdot N$, is much larger than even the Cooper pair charging energy of each junction. It coincides with about once the gap energy per island.

All the observations agree with the assumption that the feature is the result of the dual gap.



(a) Large bias voltage regime



(b) Gap feature switching voltage

Figure 4.9: Large bias properties of the very long bias comb sample; Gap feature switching voltage of the very long bias comb sample

4.5 Thermally activated conductance

In section 2.3 a model is derived to predict the zero bias conductance of chains of small SQUIDs. This subsection presents the results of a series of experiments measuring that zero bias conductance, varying both the conductance and the external flux, i.e. the effective Josephson energy.

4.5.1 Method for nonlinear conductances

In order to measure the zero bias conductance, a linear fit of the conductance around zero bias is computed:

$$I(V) \approx G_T \cdot V \quad (4.6)$$

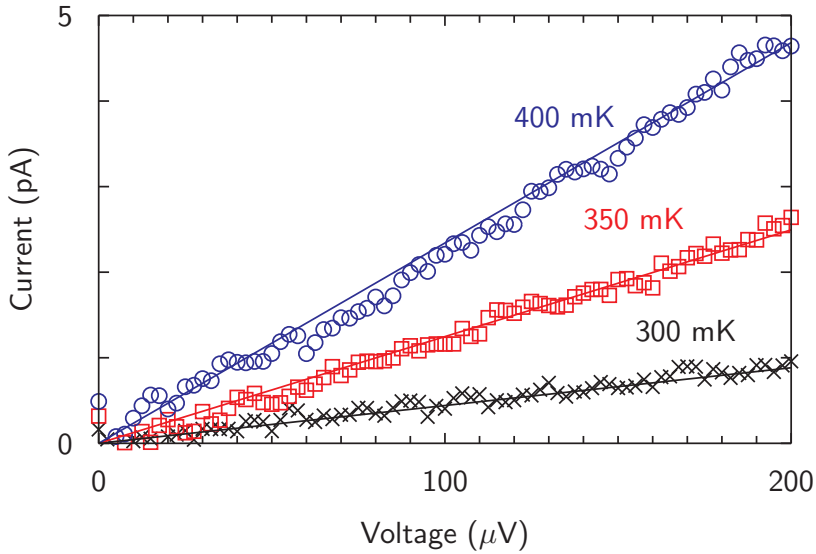
At higher temperatures – above 300 mK – this method produces good results (see Fig. 4.10(a)). As the temperature is lowered, the current detection limit of the setup makes it more and more challenging to determine the conductance.

The detection sensitivity can be increased by including a wider voltage range into the fit. Since the conductance is not strictly linear over the full base temperature Coulomb blockade voltage range, the increase of the fit range could potentially lead to impaired results.

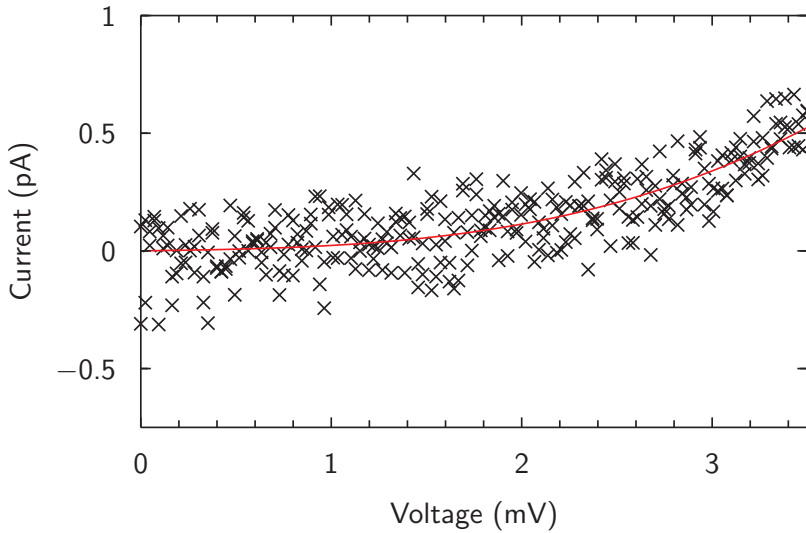
To circumvent the nonlinearity, a minimally nonlinear term is added to the fitting function. The current response to the voltage has to be symmetric with respect to the origin, so the smallest order polynomial nonlinearity is cubic:

$$I(V) \approx G_T \cdot V + \alpha \cdot V^3 \quad (4.7)$$

As an example, the IV of Soli06A at 300 mK and the fit according to Eq. 4.7 are shown in Fig. 4.10(b).



(a) Linear fit



(b) Cubic fit

Figure 4.10: a) Thermally activated conductance G_T of sample IFP11-255 near full suppression ($0.475\Phi_0$). In this voltage range and this noise ratio, the zero bias voltage can be determined accurately by a linear fit (Eq. 4.6). b) Cubic fitting of G_T (see Eq. 4.7). The IV was measured on Soli06a at 300 mK.

4.5.2 Measurement results

In sample IFP11-N, G_T is measured in both arrays at varied external flux. A good way to visualize the results of the G_T measurements is to show them in an Arrhenius plot (Fig. 4.12).

In an Arrhenius plot, the Arrhenius-like temperature dependence $G \propto \exp(-E_A/k_B T)$ takes the shape of a straight line. It is possible to characterize the temperature dependence of a given process by comparing it with the Arrhenius-like activation behavior. Any temperature dependence stronger than Arrhenius is called *super-Arrhenius*, any weaker dependence is called *sub-Arrhenius*, as is illustrated in Fig. 4.11.

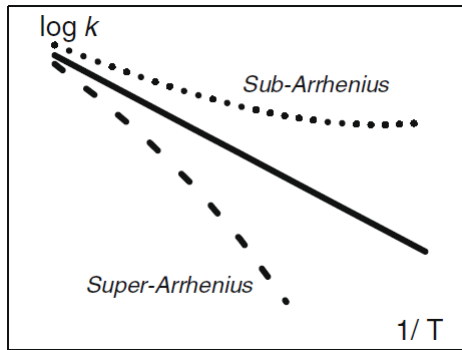


Figure 4.11: Terminology. Any temperature dependence stronger than Arrhenius is called super-Arrhenius, any weaker dependence is called sub-Arrhenius. From Ref. [Nis+09].

Temperature-independent plateau

At low temperatures, the conductance of both arrays saturates to a constant. The flux-dependent low temperature conductance is shown in Fig. 4.13. It is much more pronounced in the case $N=59$, but also clearly visible in the $N=255$ sample. The constant conductance depends strongly on the effective Josephson energy. For the longer array, the effect gets suppressed below our detection capabilities at lower Josephson energies.

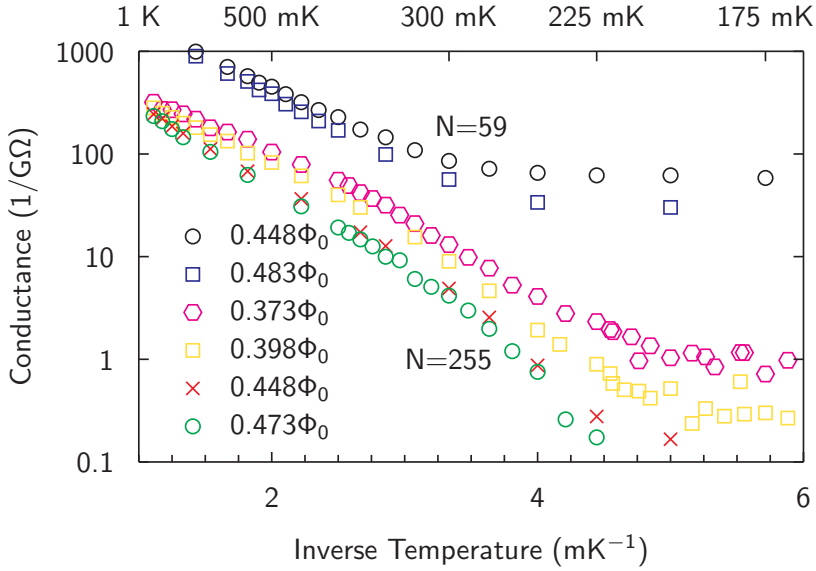


Figure 4.12: Arrhenius plot of G_T of both IFP11 samples, selected flux values. At low temperatures, a flux-dependent plateau forms. The N=255 data shows a clear super-Arrhenius curvature.

This process might be attributed to a remanent superconducting coupling over the full length of the array. This hypothesis is consistent with both the length dependence and the strong E_J dependence of this phenomenon.

Another possible explanation is low frequency noise coupling in from the contact electrodes. Such an effect could be stronger with better carrier mobility, and much more pronounced if the array is only several Λ long.

Temperature dependent part

At sufficiently high temperatures (between 200 and 300 mK) another mechanism begins to dominate transport. Since the low-temperature plateau conductance is two orders of magnitude smaller in IFP11-255, this mechanism is much better observed there.

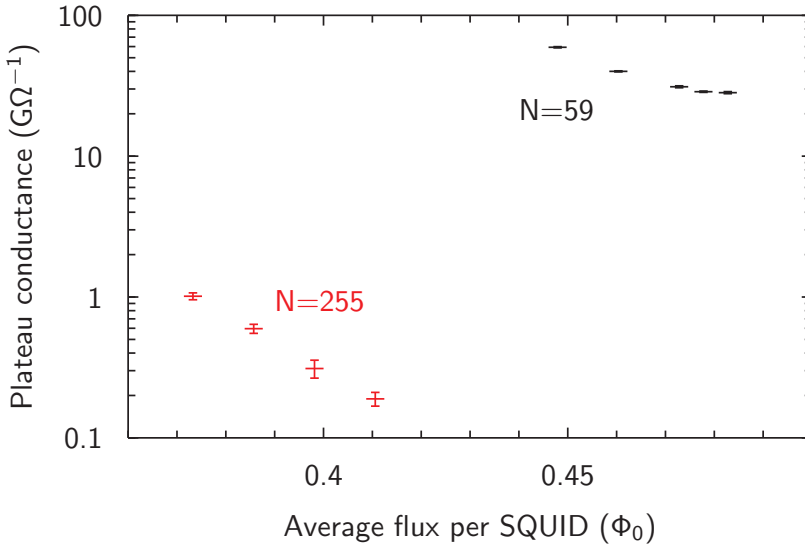


Figure 4.13: Temperature-independent conductance plateau. In the longer array, it is exponentially suppressed.

Close to full suppression, G_T shows a clear super-Arrhenius curvature. At higher temperatures, the relative dependence of G_T on the flux decreases.

Instead of analyzing this family of temperature dependence curves, it is useful to plot the same data in a different way: the temperature is fixed, and the flux dependence of G_T at that temperature is analyzed.

4.5.3 Analysis by flux dependence

Fig. 4.14 shows G_T measurements at different temperatures, varying the magnetic flux. As a first approximation, one would expect the conductance to approach zero when the flux bias in the SQUIDs reaches $\Phi_0/2$. However, at finite temperatures, the conductance is not fully suppressed, and there remains a residual conductance $G_0(T)$ at $\Phi_0/2$, which increases with increasing temperature.

After subtracting $G_0(T)$, the remaining flux-dependent conductance can be described by using Eq. 4.3, revealing a quadratic dependence of G_T on E_J . The flux-dependence of the conductance reduces to two functions, separating a flux-independent contribution from the E_J^2 -dependent part:

$$G_T(\varphi, T) = E_{J,0}^2 \cos^2\left(\frac{\pi\varphi}{\Phi_0}\right) \gamma(T) + G_0(T) \quad (4.8)$$

where G_0 is a conductance, and γ has the dimensions $\Omega^{-1} \cdot \text{eV}^{-2}$. $E_{J,0}$ is the Josephson energy at zero flux.

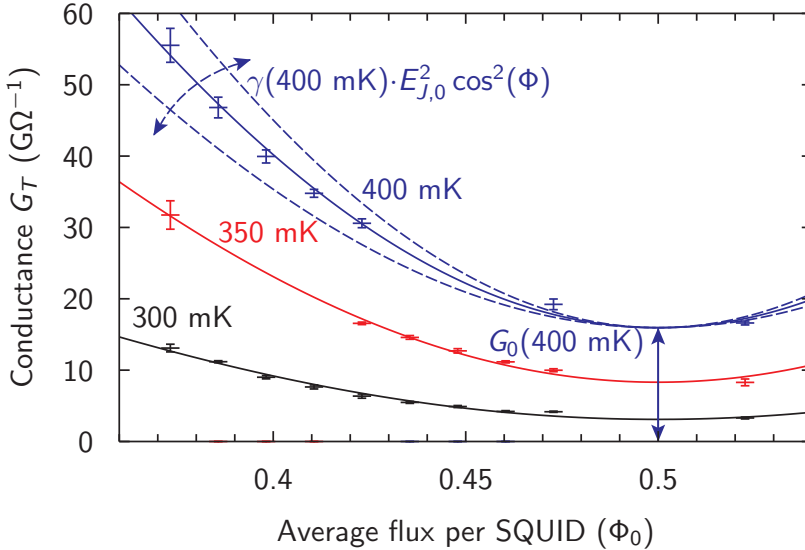


Figure 4.14: Thermally activated conductance in the small voltage bias limit (G_T , $N=255$). The dependence on the external flux has been fit according to Eq. 4.8. G_0 is determined by the offset of the conductance at $\Phi_0/2$, and γ captures the magnitude of the E_J^2 -dependent contribution.

Results – E_J^2 -dependent

Fig.4.15 shows the data separated according to Eq. 4.8. Now, both the general and the specialized theory can be applied to describe the data.

A least square fit of $\gamma(T)$ according to Eq. 2.37 reveals an energy of $E_{\max} = 229 \mu\text{eV}$, and a prefactor temperature dependence of $\alpha = 2.5$. The resulting energy agrees well with our estimate of the array charging energy of $\Lambda E_C/2 = 220 \mu\text{eV}$.

Eq. 2.37 introduces two free fit parameters, the prefactor amplitude and temperature dependence. With the additional assumptions of subsection 2.3.3, an analytic expression for the rates is found, and the conductance can be fit with only the constrained parameters E_C and $E_{J,0}$.

$\Lambda = 10$ is assumed. The least square fit of the N=255 array data results in a Cooper pair charging energy of $E_C = 41.5 \mu\text{eV}$, and a zero flux Josephson energy of $E_J = 468 \mu\text{eV}$, which is both well within the estimated array parameters.

Both fits are shown in Fig. 4.15.

Results – flux-independent

In the case of the flux-independent contribution $G_0(T)$, α is zero. For the N=59 array, we get $E_{\max} = 180 \mu\text{eV}$. The N=255 array is best fit with $E_{\max} = 210 \mu\text{eV}$. These energies are comparable to both the activation energy in the flux-dependent contribution, and to the quasiparticle gap of thin film Aluminum, $\Delta = 200 \mu\text{eV}$.

For the explicit rates model, $\Lambda = 10$ is maintained and the usual thin film Aluminum gap of $\Delta = 200 \mu\text{eV}$ is assumed. The charging energy is set to $E_C = 10.4 \mu\text{eV}$, which is 1/4 of the Cooper pair charging energy.

The only free fit parameter is the tunnel resistance. It is fit as $R_{T,255} = 14.81 \Omega$ and $R_{T,59} = 29.59 \Omega$, which is much lower than expected.

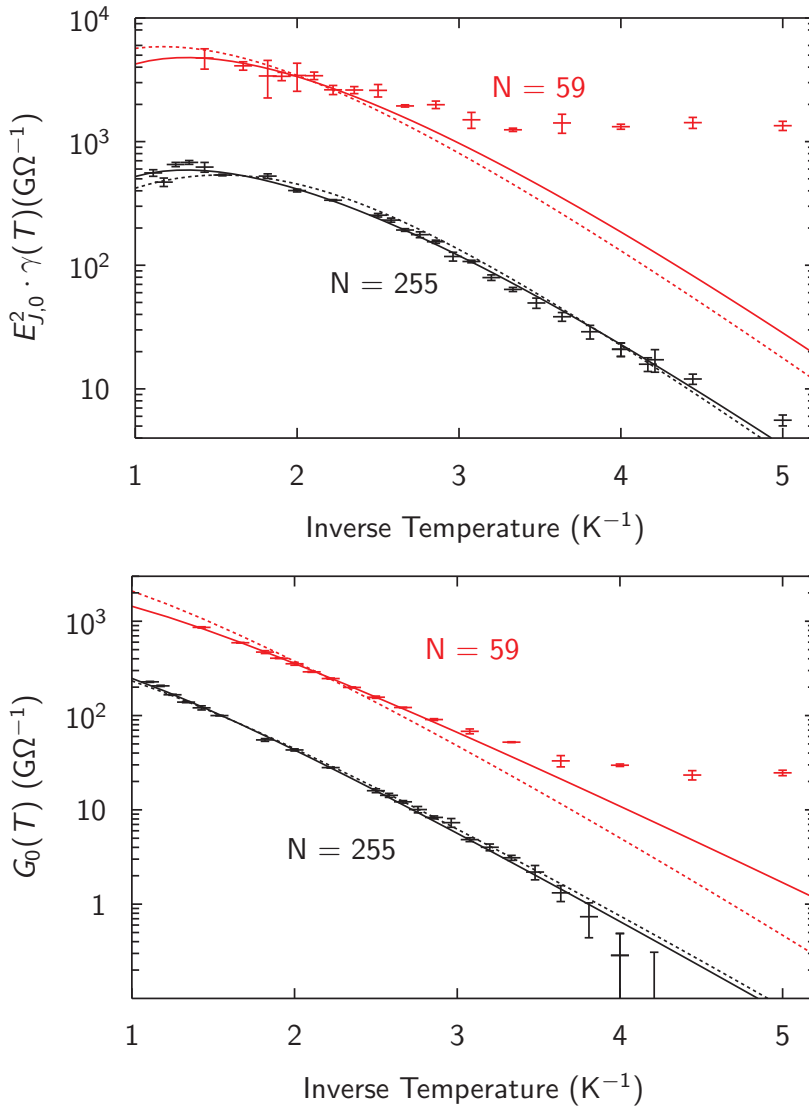


Figure 4.15: Temperature dependence of the two components of G_T of IFP11-N. Continuous lines represent the general model, dashed lines represent the P(E)-derived model.

4.5.4 Additional data

Additionally, the thermally activated zero bias conductance is measured in the two IFP-Soli06 samples. Since the flux dependence of the conductance is not tested, a separation according to Eq. 4.8 can not be applied. A fit of the general model would have too many free fit parameters and is not attempted.

With the application of the explicit rates, the number of parameters is reduced. The data and the fit results are shown in Fig. 4.16. $\Lambda = 10$ and $\Delta = 200 \mu\text{eV}$ is assumed.

In sample IFP-Soli06a, which has a relatively low conductivity, the least square fit gives $R_t = 356.6\Omega$, $E_C^{\text{CP}} = 95.2 \mu\text{eV}$ and $E_J = 303.3 \mu\text{eV}$. For sample Soli06b, the results are $E_C^{\text{CP}} = 68.1 \mu\text{eV}$, $R_t = 215.4\Omega$ and $E_J = 658.6 \mu\text{eV}$.

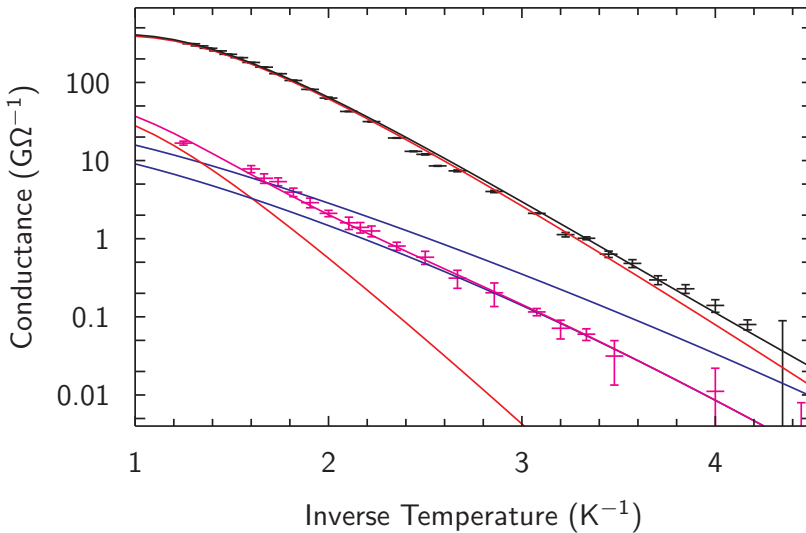


Figure 4.16: Thermally activated zero bias conductance (G_T) of samples IFP-Soli06a (magenta) and IFP-Soli06b (black). The conductance has been fit to the P(E)-derived model, with an E_J^2 -dependent contribution (red) and with equilibrium quasiparticles (blue).

4.5.5 Discussion

The main motivation for measuring the thermally activated zero bias conductance is to get a quantitative handle on the transport properties of the arrays. Even with a very general approach to the hopping rates, one gets good quantitative data on the average energy of a carrier within the array. Good agreement with the area-based estimate of the single junction charging energy is achieved.

Encouraged by the quadratic E_J dependence of both G_V and G_T , the P(E) theory can be used to quantitatively explain the transport data. It then covers the dependence of the zero bias conductance on E_J , T and N – albeit, in the case of the number of SQUIDs, only for two array lengths.

In all four arrays examined, the Josephson energy is estimated higher by the zero bias transport fit than by the normal state resistance. Both methods agree in the order of magnitude. The method that was used to determine R_N might have oversimplified the physics of long array conductance, or indeed the physics of Josephson junctions. The microscopic properties of highly resistive Josephson junctions are discussed in Ref. [Gre+11].

The tunneling resistance R_t derived from the assumption that G_0 is solely the result of equilibrium quasiparticles is much too low, meaning the current is much larger than a more realistic estimate of R_t would predict. This can have several reasons:

- The equilibrium quasiparticle rate (Eq. 2.48) is only estimated roughly, the actual semiconductor model contains a prefactor of order unity that needs to be calculated more carefully.
- At higher temperatures the assumption of only one charge carrier at any time may break down, rendering the calculation inaccurate.
- A number of reasons could cause Cooper pair transport at an average flux per SQUID of $\Phi_0/2$, including local flux noise, global flux noise and a spread in junction or loop size.

The two IFP-Soli06 samples were designed to have identical parameters. From the high bias behavior, some deviation were to be expected. The observed behavior might be explained by a slightly thicker oxide barrier

4 Measurements

in IFP-Soli06a. Then, E_C would be a little higher than for the thinner barrier. Since the critical current depends exponentially on the thickness, a stronger variation in E_J is not surprising.

4.6 Analysis of flux noise influence

Trying to identify the flux dependence in sample IFP-Soli06b, it is found that the conductance increases with increasing coil current. Strong heating of the cryostat can be excluded, since the temperature at the sensor does not rise.

A possible explanation is that with increasing coil current, a local noise source gets stronger, and that in this sample, the local noise is more important for the thermally activated conductance than the Josephson coupling. Fluctuations in the coil current itself would cause a homogeneous flux noise in each of the SQUIDs.

In order to investigate this effect, the setup is modified to intentionally impose homogeneous flux noise to the array.

Instead of showing the flux, the x-axis remains in the experimental form of coil current, since direct effects of the current in addition to the effects of flux are considered. $\Phi_0/2$ per SQUID is expected at around 100 mA of coil current.

4.6.1 Setup modifications

The current for the coil is supplied by a custom current source, which is voltage controlled via the SMU. A transformer is added in series to the flux biasing circuit (see Fig. 4.17). The DC current flux bias properties are left unchanged. However, an arbitrary RF-signal can now be added to the coil, imposing a homogeneous flux noise on the array.

An arbitrary waveform generator⁶ (AWG) is used to generate white noise. Since all circuit elements are linear, the added flux noise at the array scales linearly with the noise amplitude of the AWG.

4.6.2 Results

Low temperature results

At 100 mK without external flux, the array is Coulomb blockaded, no conductivity can be measured at zero bias. As the coil current is increased,

⁶Agilent 33210A Function / Arbitrary Waveform Generator, 10 MHz

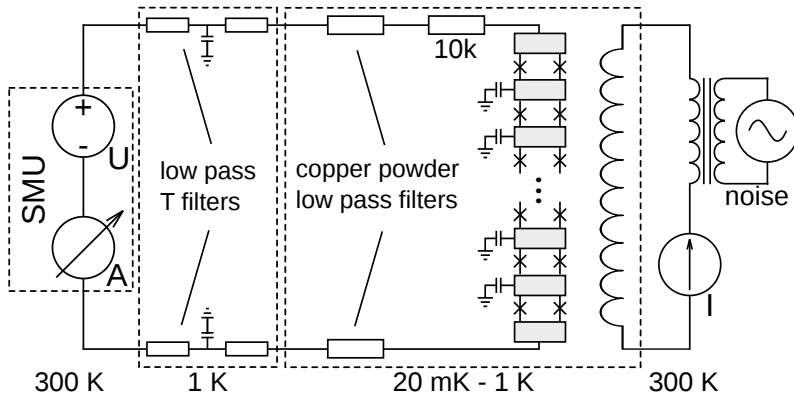


Figure 4.17: Coil current noise setup: in order to test the influence of uniform flux noise on charge transport, a simple modification of the setup was implemented. The DC coil current could be controlled in the same way as before. Noise was added to the coil current inductively.

a detectable zero bias conductance appears at high coil currents (Fig. 4.18, no extra noise). With increasing extra noise, the conductance rises, and becomes detectable at ever lower coil currents.

For a given level of added noise, the rise of the conductance with temperature is exponential:

$$G(I_{\text{coil}}) = G^{(0)} \cdot \exp(\eta \cdot I_{\text{coil}})$$

$G^{(0)}$ and η depend on the amplitude of the additional noise, as shown in Fig.4.19.

The effect of the added coil current noise is qualitatively the same as the effect of the coil current itself. This can be taken as evidence of a preexisting noise on the coil current with a significant influence on the zero bias conductance.

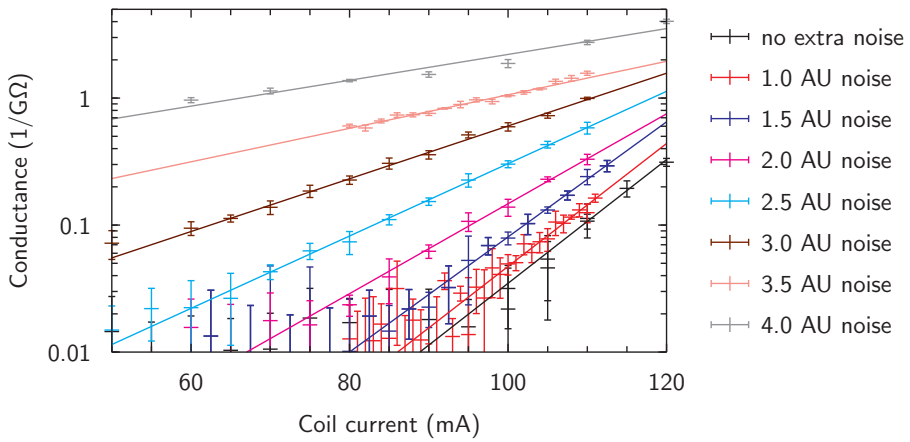


Figure 4.18: Flux noise response of the zero bias conductance at 100 mK. Without flux noise, the conductance rises with increased coil current, whereas from previous experiments, a drop in conductance is expected. $\Phi_0/2$ per SQUID is reached around 100 mA of coil current. Adding noise to the coil current increases the conductance in qualitatively the same way.

4 Measurements

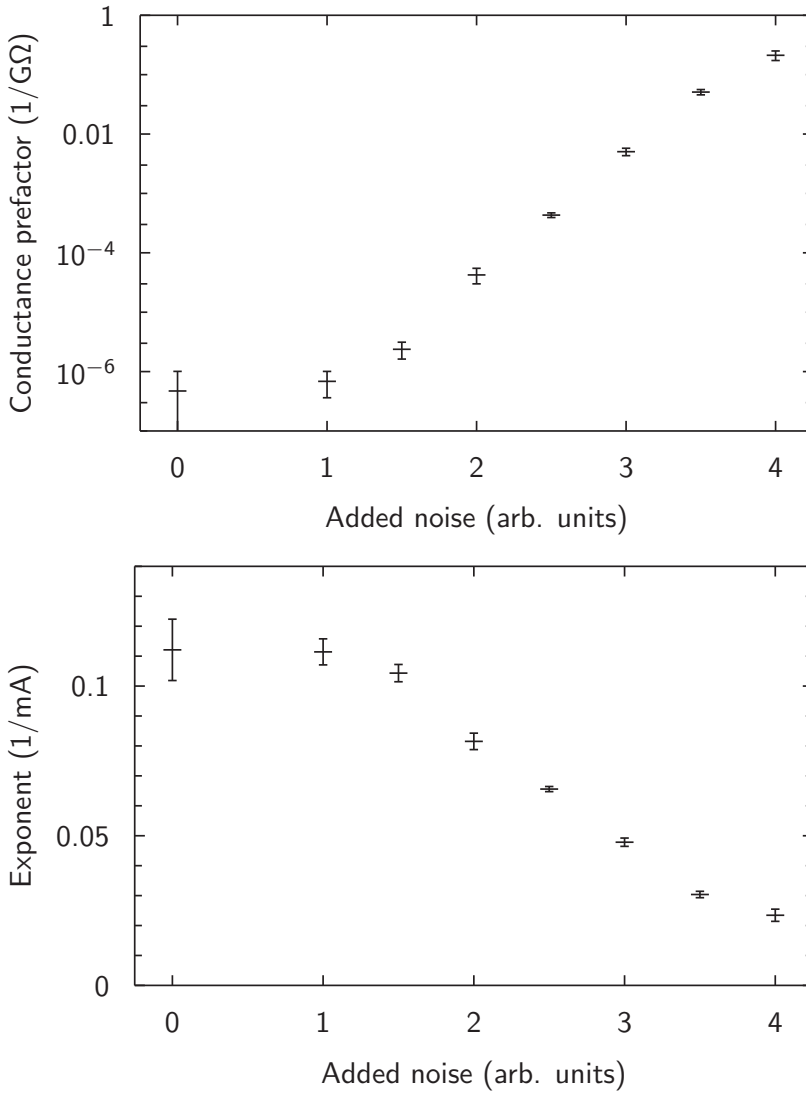


Figure 4.19: Low temperature (100mK) noise dependence. The conductance depends exponentially on the coil current, $G(I_{\text{coil}}) = G^{(0)} \cdot \exp(\eta \cdot I_{\text{coil}})$. $G^{(0)}$ and η change with the amplitude of the added noise. A saturation can be observed, indicating preexisting coil current noise.

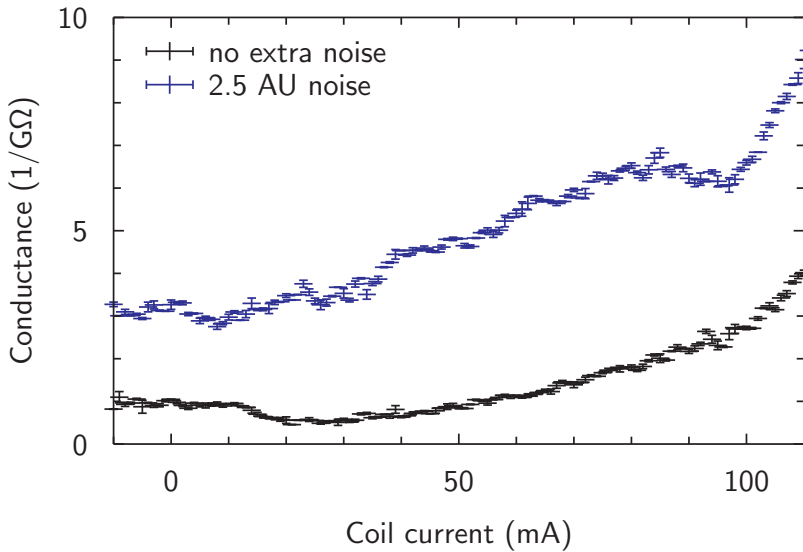


Figure 4.20: Effect of added coil current noise on the conductance at 300mK. As in the low temperature measurements, the conductance rises with coil current. At elevated noise levels, a dip appears.

Results at elevated temperatures

The noise influence is measured at 300 and 400 mK to study the effect at elevated temperatures. At these temperatures, a conductance is measurable for all coil currents. The results are shown in Figs. 4.20 and 4.21.

At 300 mK without extra noise, the current qualitatively behaves similar to the low temperature behavior.

At 300 mK with added noise, as well as at 400 mK with and without noise, a parabolic dip appears in the conductance, reminiscent of the parabolic flux dependence in samples IFP11-255 and IFP11-59.

4.6.3 Discussion

At low temperatures, the effect of adding noise and of increasing the coil current are qualitatively the same. Raising the temperature also increases

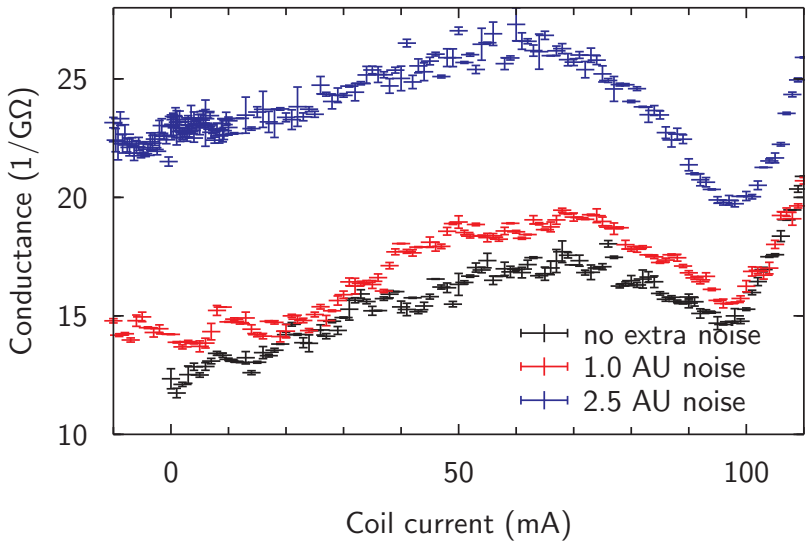


Figure 4.21: Effect of added coil current noise on the conductance at 400mK. Superimposed with the rise with coil current, a pronounced dip appears in the conductance at $\Phi_0/2$.

the conductance in a similar way. In the low temperature regime, all three seem to add up and increase the conductance. Without a better theoretical idea of the microscopic mechanism, the interplay of the three is hard to interpret.

In the low temperature regime, the Josephson energy appears to have no influence on transport. At elevated temperature and/or noise levels, the expected quadratic dependence begins to show.

The individual charging energies of the junctions in this sample are considerably larger than in IFP11-255 and IFP11-59. One might speculate that under the influence of disorder, the carrier mobility is very low at low temperatures. Only by real or effective thermal activation do the carriers move at all, and only at sufficiently high mobility does the Josephson tunneling come into play.

5 Outlook

My mother made me a scientist without ever intending to. Every other Jewish mother in Brooklyn would ask her child after school: So? Did you learn anything today? But not my mother. "Izzy" she would say, "did you ask a good question today?" That difference – asking good questions – made me become a scientist.

Isidor Isaac Rabi
[She88]

Starting from the presented results, a number of paths may be taken to improve the understanding of long 1D SCJJAs.

Clearly, further research is necessary to understand the interplay of different sources of fluctuations in the activation of the zero bias conductance.

The P(E)-derived hopping model should be modified to account for the presence of offset charges. For this one needs to know the amplitude of the offset charges. It could be estimated by calculating the equilibration effects of charge redistribution, similar to the approach of Ref. [JH00]. The model might be expanded to finite voltages, so that additional properties of the current-voltage characteristics can be predicted.

To test the existing model experimentally, a set of experiments may be conducted that varies the screening length Λ or the superconducting gap Δ while leaving the junction parameters identical. Following subsection 2.1.2, it can be estimated that the screening length can be changed from $\Lambda = 9$ to $\Lambda = 11$ by varying the ground electrode distance from $d = 0.6 \mu\text{m}$ to $d = 2.8 \mu\text{m}$. To vary the superconducting gap, the results from subsection 3.2.4 predict a change of the gap from $\Delta = 190 \mu\text{eV}$ to $\Delta = 210 \mu\text{eV}$ when the Aluminum layer thickness is lowered from 40 nm to 15 nm. These changes do not seem very large, but the model predicts a significant change in G_T , as is shown in Fig. 5.1.

Following subsection 2.1.3, one expects very interesting properties from an array with a voltage bias comb such that $n_i \Lambda_g > N > \Lambda$. With slight modifications, the existing hopping model may be used to predict the current-voltage characteristics of such an array.

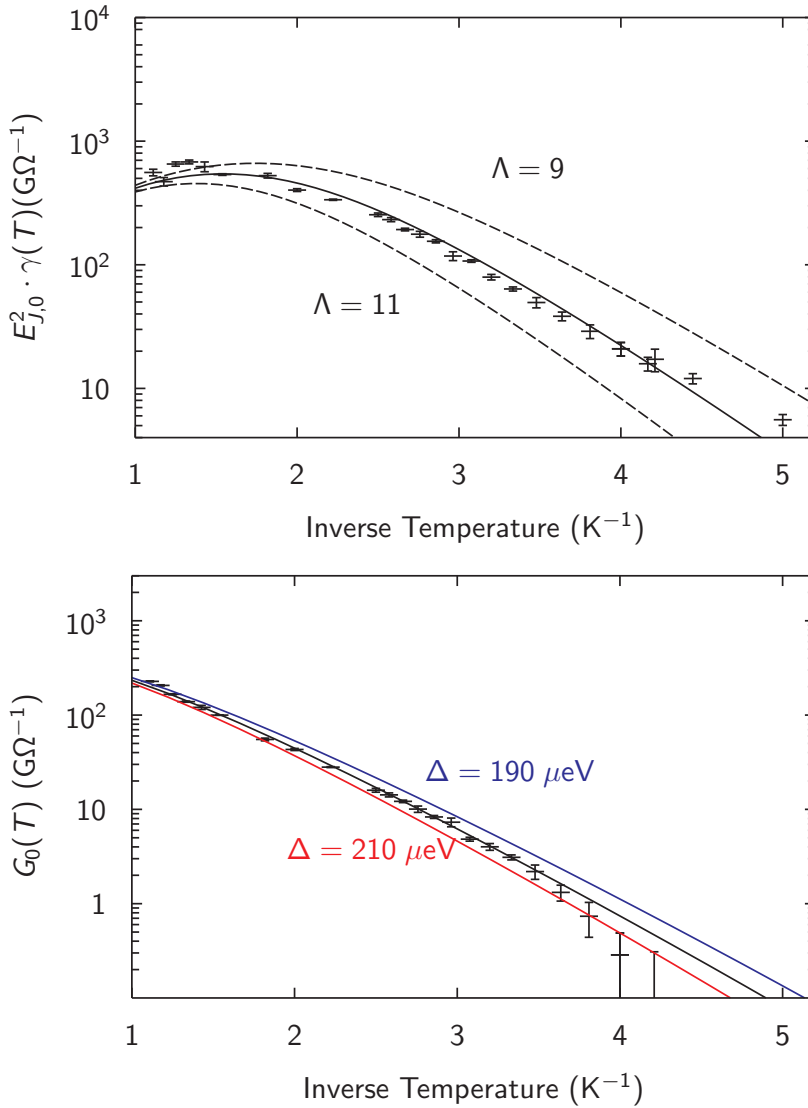


Figure 5.1: Fabricating a set of arrays with identical junction parameters, but with a different screening length Λ (top) or with different superconducting gaps Δ (bottom), should – according to the P(E)-derived model – lead to detectable changes of the thermally activated zero bias conductance G_T . This way, the model can be tested.

6 Conclusion

Nothing is so fatal to the progress of the human mind as to suppose that our views of science are ultimate; that there are no mysteries in nature; that our triumphs are complete, and that there are no new worlds to conquer.

Humphry Davy
(as quoted by David Knight[Kni98])

In this thesis, the attempt is made to gain a quantitative understanding of the charge transport through long one-dimensional arrays of small capacitance Josephson junctions (long 1D SCJJAs). Calculations and experimental results are presented to close the gap between theory and experiment.

It is shown that the current-voltage characteristics of long 1D SCJJAs are the results of complex processes, and no consistent model exists to fully explain the charge transport.

If a voltage is applied to a Coulomb-blockaded array, the voltage drops to ground on a length scale of Λ . The non-uniform voltage distribution in the static limit might be used to describe charge injection into the array, but no force is applied to charges in the middle of a long array. Increasing the bias voltage, the gap voltage may be reached locally, leading to quasiparticle transport in addition to or instead of Cooper pair transport. Additionally, there is an unknown amount of offset charge on each island, inhibiting charge transport in the case of small Josephson coupling.

This thesis presents several paths to improve upon the existing understanding of long 1D SCJJAs.

First, the physical foundations are discussed. Viewing the Josephson coupling as a perturbation, the electrostatic properties are used to determine the charging energy scale. A scheme is presented and calculated to separate the charge screening length Λ from the bias voltage penetration

length. This could lead to a new mode of Cooper pair transport – with a constant force acting on the Cooper pairs – that is much easier to model.

After the physics of superconductivity and tunneling are introduced, a charge carrier hopping model is presented to describe the thermally activated zero bias conductance. In a generalized form, it already grants access to the array charging energy $\Lambda E_C/2$, provided the rates do not depend on the temperature too strongly.

Inspired by the P(E) theory of Ingold and Nazarov, explicit expressions for the hopping rates are presented, assuming that the array itself provides a high impedance environment for each small junction.

Then, an overview of the fabrication process of the long 1D SCJJAs is given. An experiment is shown that confirms the dependence of the superconducting gap of thin film Aluminum on the film thickness. The parameters of the dependence for films fabricated with the presented methods are estimated.

The setup for the charge transport experiments is presented. A method to estimate the array properties from the high bias voltage features in the current-voltage curve is shown. From – so far unpublished – previous experiments it has already been known that the voltage-activated conductance G_V depends on E_J quadratically, which is confirmed and used as a sensitive calibration method for the external flux. For large ratios of E_J/E_C , the conductance is shown to deviate from the E_J^2 -dependence towards higher values.

Then, a feature of the current-voltage curve of a sample with islands of alternating thicknesses is analyzed. It is shown to be qualitatively consistent with the assumption of alternating gaps in the islands, and the occurrence of two distinct switching events during a single voltage ramp.

Measurements of the thermal activation of the zero bias conductance G_T are shown. A method is presented to extract G_T from current-voltage measurements. In an experiment with varying external flux, it is shown that G_T has a flux-independent part, and that the flux-dependent part depends on E_J quadratically. The two contributions have a different temperature dependence. From the flux-dependent part, a value for $\Lambda E_C/2$ is calculated that agrees well with previous estimates. With the P(E)-derived hopping model, the flux-dependent transport can be fit quantitatively. The flux-independent data can be fit qualitatively as quasiparticle trans-

port, but the observed conductance is underestimated by the model. G_T data from additional arrays is shown. The P(E)-derived hopping model can be used to describe these measurements as well.

Then, the influence of external flux noise on the zero bias transport is analyzed. It is shown that the existing coil current noise, the added flux noise and the thermal fluctuations have the same type of influence on the conductance. This means that parts of the flux-independent transport shown in the previous section may be the result of flux noise.

Finally, possible steps to test and to proceed from the presented results are shown.

A Full derivation of the incoherent tunneling model

The model described here has been developed by Vogt and Marthaler in cooperation with the author.

General model

In the regime of very low transport currents we can assume that on average there is less than one excess charge-carrier in the linear array.

In this case the array can be modelled by a master-equation for the probability p_n that the charge-carrier is on the n -th island or outside the array (p_{N+1}). The general form of the master-equation is given by:

$$\dot{p}_n = -\Gamma_{n \rightarrow n+1} p_n - \Gamma_{n \rightarrow n-1} p_n \quad (\text{A.1})$$

$$+ \Gamma_{n-1 \rightarrow n} p_{n-1} + \Gamma_{n+1 \rightarrow n} p_{n+1} \quad (\text{A.2})$$

$$\dot{p}_1 = -\Gamma_{1 \rightarrow 2} p_1 - \Gamma_{1 \rightarrow N+1} p_1$$

$$+ \Gamma_{N+1 \rightarrow 1} p_{N+1} + \Gamma_{2 \rightarrow 1} p_2$$

$$\dot{p}_{N+1} = -\Gamma_{N+1 \rightarrow 1} p_{N+1} - \Gamma_{N+1 \rightarrow N} p_{N+1}$$

$$+ \Gamma_{N \rightarrow N+1} p_N + \tilde{\Gamma}_{1 \rightarrow N+1} p_1$$

The rate $\Gamma_{n \rightarrow m}$ is the rate of a charge carrier hopping from island n to m (see Fig. 2.24). Assuming that detailed balance holds for all equilibrium rates we can define,

$$\Gamma_{n,n+1} = e^{-\frac{E_n}{k_B T}} \Gamma_{n \rightarrow n+1} = e^{-\frac{E_{n+1}}{k_B T}} \Gamma_{n+1 \rightarrow n} \quad (\text{A.3})$$

$$\bar{p}_n = e^{\frac{E_n}{k_B T}} p_n, \quad (\text{A.4})$$

with the on-site-energies of the charge-carriers E_n . The voltage-bias driving the current is accounted for by modifying the equilibrium rate of the charge-carriers leaving the array from the first island:

$$\frac{\tilde{\Gamma}_{1 \rightarrow N+1}}{\Gamma_{N+1 \rightarrow 1}} = e^{-\frac{ZeV}{k_B T}} \frac{\Gamma_{1 \rightarrow N+1}}{\Gamma_{N+1 \rightarrow 1}}, \quad (\text{A.5})$$

where Z is the charge of the charge-carrier in multiples of the elementary charge. A charge-carrier entering the array on the voltage biased side gains an energy of ZeV . We assume that despite the non-equilibrium situation the forward and backward rates between neighbouring sites are in detailed balance. Consequentially the ratio of the tunneling rates in and out of the array has to be modified by an exponential factor in Eq. A.5 that takes into account the energy the charge-carriers gain by entering the array. A current is driven through the system because the energy of the empty array is only elevated to $E_{n+1} = ZeV$ with respect to the first site. With respect to the site N the energy of the empty state is taken to be $E_{N+1} = 0$.

The condition for a steady-state-solution of Eq. A.3 is given by

$$\begin{aligned} 0 &= -\Gamma_{n-1,n} \bar{p}_n - \Gamma_{n,n+1} \bar{p}_n + \Gamma_{n-1,n} \bar{p}_{n-1} + \Gamma_{n,n+1} \bar{p}_{n+1} \\ 0 &= -\Gamma_{N+1,1} \bar{p}_1 - \Gamma_{1,2} \bar{p}_1 + \Gamma_{N+1,1} \bar{p}_{N+1} + \Gamma_{1,2} \bar{p}_2 \\ 0 &= -e^{-\frac{ZeV}{k_B T}} \Gamma_{N+1,1} \bar{p}_{N+1} - \Gamma_{N,N+1} \bar{p}_{N+1} \\ &\quad + \Gamma_{N+1,1} \bar{p}_1 + \Gamma_{N,N+1} \bar{p}_N, \end{aligned}$$

This set of equations can be solved for arbitrary rates Γ and energy levels E_n as long as the detailed balance between the rates is valid.

$$\begin{aligned} p_n &= \frac{1}{N_{norm}} e^{-\frac{E_n}{k_B T}} \\ &\times \left(\sum_{m=1}^n \frac{1}{\Gamma_{m-1,m}} + e^{-\frac{2eV}{k_B T}} \sum_{m=n+1}^{N+1} \frac{1}{\Gamma_{m-1,m}} \right) \\ N_{norm} &= \sum_{n=1}^{N+1} e^{-\frac{E_n}{k_B T}} \left(\sum_{m=1}^n \frac{1}{\Gamma_{m-1,m}} + e^{-\frac{2eV}{k_B T}} \sum_{m=n+1}^{N+1} \frac{1}{\Gamma_{m-1,m}} \right) \end{aligned}$$

Since we are in the steady state the current can be calculated from any two neighbouring islands

$$I = -Ze (\Gamma_{n \rightarrow n+1} p_n - \Gamma_{n+1 \rightarrow n} p_{n+1}) \quad (\text{A.6})$$

from which we obtain the zero bias differential conductance

$$\begin{aligned} g_0 &= \frac{Z^2 e^2}{k_B T} \lim_{V \rightarrow 0} \frac{1}{N_{norm}} \\ &= \frac{Z^2 e^2}{k_B T} \frac{1}{\sum_{n=1}^{N+1} \exp\left[-\frac{E_n}{k_B T}\right]} \left(\sum_{m=1}^{N+1} \frac{1}{\Gamma_{m-1,m}} \right)^{-1}. \end{aligned} \quad (\text{A.7})$$

In the first term in the conductivity we approximate $\exp\left[-\frac{E_n}{k_B T}\right] \approx 1$, which means that the empty state $E_n = 0$ is the one which is mostly occupied. The second term is mostly dominated by the rate $\Gamma_{n,n+1} = \exp(-E_n/k_B T) \Gamma_{n \rightarrow n+1}$ with the maximal energy E_{max} of the array. Therefore we can write the conductivity in the form,

$$g_0 = \frac{Z^2 e^2 \gamma}{(k_B T)^{1+\alpha}} e^{-E_{max}/k_B T}. \quad (\text{A.8})$$

Since the rates themselves can have an explicit temperature dependence we allow for an additional exponent α in the temperature dependence of the prefactor.

Special array model

To compare the differential conductance g_0 (Eq. A.7) with experiments we have to specify the Energies E_n and the rates $\Gamma_{n \rightarrow n+1}$ of the setup. In an empty Josephson-junction-array the energy of an additional charge-carrier increases from $E = 0$ at the ends of the array to $\Lambda \frac{E_c}{2}$ in the bulk of the array on the lengthscale Λ , where E_c is the charging energy of the single charge carrier

$$E_c = \frac{Z^2 e^2}{2C}. \quad (\text{A.9})$$

We approximate this behaviour with a model where the energies E_n increase linearly from the ends of the array on Λ sites to the bulk value (see Fig. 2.24). In this model the zero bias differential conductance Eq. A.7 takes the form

$$g_0 = \frac{Z^2 e^2}{k_B T} \left[1 + N' e^{-\Lambda \frac{E_c}{2k_B T}} + 2 \sum_{m=1}^{\Lambda-1} \left(e^{-m \frac{E_c}{2k_B T}} \right) \right]^{-1} \times \frac{\Gamma(0) \Gamma\left(\frac{E_c}{2}\right)}{2 \sum_{m=0}^{\Lambda-1} e^{m E_c / 2k_B T} \Gamma(0) + (N' - 1) e^{\Lambda E_c / 2k_B T} \Gamma\left(\frac{E_c}{2}\right)} \quad (\text{A.10})$$

$$N' = (N - 2\Lambda + 2) \quad (\text{A.11})$$

where N' is the number of sites with the energy $E = \frac{\Lambda}{2} E_c$ in the bulk and $\Gamma(0)$ and $\Gamma\left(\frac{E_c}{2}\right)$ are the rates corresponding two the hopping rates between neighbouring sites that correspond to the two Energy differences $\delta E = E_{n+1} - E_n$ between neighbouring sites that occur in this model: $\delta E = 0$ and $\delta E = \frac{E_c}{2}$.

In the first factor the bulk contribution proportional to N' is suppressed due to the thermal activation factors $\exp(-E_n/k_B T)$. The bulk contributes significantly to this factor when we reach the limits of the assumption of a single charge carrier in the array we used to obtain the master equation. When the thermal activation factors are comparable to $\frac{1}{N}$ we start to see a non-neglectabel probability of more than one charge-carrier in the array.

B Technical notes on temperature control

The PID control software was programmed by H. Rotzinger. Due to hard- and software limitations, it was programmed to run on a computer independent from the measurement setup. Communication with the measuring computer is accomplished via network.

When using AVS47 or a similar device in combination with automated temperature control, it is important to consider the fact that the resistance of the measurement resistor changes over several orders of magnitude. If this necessitates a change of the resistance bridge range, problems in keeping the temperature stable often arise.

Good PID control parameters have to be determined experimentally for a given temperature range. For the dilution refrigerator used for the reported experiments, a set of good parameters is shown in Fig. B.1.

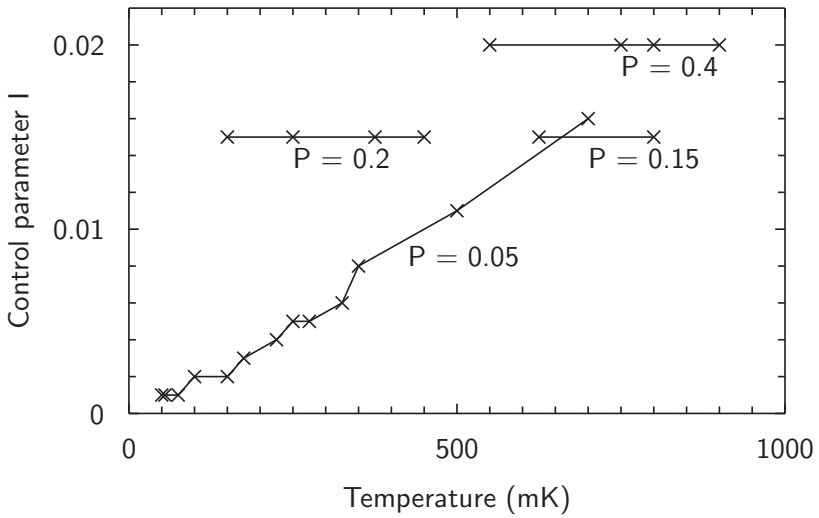


Figure B.1: Stable PID parameters: When using the TIP temperature control script, finding optimal control parameters is a matter of trial and error. The differential component was not used, so $D=0$. A good set of parameters minimizes control oscillations and settling time after a change in target temperature.

C Photolithographic fabrication process details

These are the fabrication recipes as experimentally determined during the course of this work. They have been used for the experiment reported in Ref. [Zwi12].

An overview of the general procedure, as well as the full name of substances and devices, can be found in section 3.1.

C.1 Mask fabrication

Pattern preprocessing

Our default design file format was *GDS*. It was loaded into the software Genisys Layout Beamer (LB), and exported into the Autocad format *DXF*, which the DWL 66 accepted for further processing. In case of multiple layer design files, the LB software proved very useful for arranging, marking and (if necessary) inverting the layer designs.

For our chain of lift-off processes, the design needs to be non-inverted, but mirrored on one axis, as can be easily understood following section 3.1.

Laser lithography

For the direct writing of patterns, we used a Heidelberg Instruments DWL66 direct laser writer equipped with a HeCd-Laser ($\lambda=442\text{nm}$).

The mask blanks we bought came precoated with 530 nm of AZ1518 positive photoresist, which we used. Alternatively, masks can be covered with the S1805 by ourselves, if special care is taken fixing the mask in the spin coater (much higher mass than the usual wafers!). The S1805 process is described below.

We used the 10 mm write head in bidirectional mode. Optical filters of 30% and 10% (i.e. a total of 3%) were inserted into the laser beam line.

The energy setting can be adapted to account for photon proximity effect in the case of a high percentage of exposed area. Development is identical to the process described below, except for the time.

| Head | Filters | Energy | Defoc | Develop |
|-------|---------|--------|-------|---------|
| 10 mm | 3% | 80-90% | 3700 | 50 s |

Chromium wet etching

The buffered etching solution Chrome Etch 18 was bought and used. The properly developed and dried mask blank is put into Etch 18 and agitated for 60 seconds. Stop etching with de-ionized water.

Post-etch mask cleaning

The remaining photoresist has to be removed before the mask can be used. We tried less dangerous approaches, but the only process that succeeded in removing the post-etch AZ1518 was this, using highly corrosive Piranha solution:

- be sure to wear rubber gloves, a lab coat and a facial protection
- be sure to do this under a fume hood
- prepare a ceramic dish big enough for the mask
- prepare a water bath to cool the solution
- fill 50 ml of hydrogen peroxide into a 250 ml glass that is cooled in the cooling water
- slowly (!) pour 150 ml of concentrated sulphuric acid into the hydrogen peroxide
- you now have 200 ml of hot Piranha solution
- put the mask in the dish and pour the Piranha on it

- after five minutes, take the mask out
- clean it in DI water, blow dry
- good cleaning results by rinsing with ethanol, blowing it off quickly
- leave the Piranha in the hood so that the peroxide can gass out during the next days
- after that, dump the Piranha remains into the H2SO4 waste

C.2 Pattern transfer

Resist spin coating

This is the resist stack used for generating an undercut for optimal lift-off behavior. Various spin coaters were used, depending on location and availability. The resist was baked using a hot plate.

The bottom layer resist was borrowed from the e-beam process, details can be found there.

| Resist | Pre-spin | Main spin | baking |
|-----------|---------------|----------------|---------------|
| Copolymer | 300 rmp, 10 s | 4000 rpm, 60 s | 140 °C, 5 min |
| S1805 | 300 rmp, 10 s | 4500 rpm, 90 s | 115 °C, 1 min |

The resulting thicknesses estimated from the resists' data sheets are: 250 nm of Copolymer, 500 nm of S1805.

Mask aligner step

The actual pattern transfer from photomask to the resist covered substrate is done in the Suss MA 6 mask aligner. Good parameters are:

| Resist | Mode | Intensity | Duration |
|--------|--------------|-----------------------|----------|
| S1805 | soft contact | 10 mW/cm ² | 5 s |

Development

If a high percentage of the surface was exposed, the developer tends to saturate. It is important to use plenty of developer and agitate during development. With our developer MF 319, development times of 60 to 80 seconds proved successful. The sample has to be bathed in and/or rinsed with de-ionized water to remove remaining developer from the surface, and blown dry with nitrogen.

Undercut etching

The second resist layer is etched away in an oxygen plasma. Etching was done in a Sentech SI 220.

| Gas | Flow | Set pressure | Power | Duration |
|----------------|---------------------------|--------------|-------|----------|
| O ₂ | 15 (cm) ³ /min | 1 Pa | 50 W | 360 s |

The set pressure was not reached, meaning that during the etch process, gasses were pumped out at maximum pump rate while a constant stream of oxygen was flowing in.

Evaporation

Evaporation of the leads and bond pads was done in a Lesker PVD 75. A Titanium target and a Gold-Palladium alloy target were loaded to the multi-target revolver.

| Target | Chamber pressure | Thickness | Rate |
|--------|------------------|-----------|-------------|
| Ti | 2E-6 Torr | 3 nm | 1.2 Å/s |
| AuPd | 2E-6 Torr | 20 nm | 0.1-0.3 Å/s |
| Au | 2E-6 Torr | 50 nm | 0.1-0.3 Å/s |

The third layer required a second photolithography iteration, see section 3.1.

Lift-off

For the lift-off, a certain amount of ultrasound is helpful. Two hours ultrasonic bathing in warmed (60°C) N-Methyl-2-pyrrolidone (NMP) works well, good ventilation is advised.

D Electron beam lithography process details

Resist application

It is crucial to avoid dust particles on the substrate during spin-on. Clean the substrate with nitrogen flow directly before applying the resist for best results.

The PMMA resist we used was Allresist AR-P 679.04, a 950k PMMA solution, 4% in ethyl lactate. We diluted it to 2% in order to reduce film thickness. The Copolymer was MicroChem Copolymer MMA(8.5)MAA, 7.5 % in ethyl lactate.

| Resist | Pre-spin | Main spin | baking |
|-----------|---------------|----------------|---------------|
| Copolymer | 300 rmp, 10 s | 4000 rpm, 60 s | 140 °C, 5 min |
| PMMA 950k | 300 rmp, 10 s | 4000 rpm, 60 s | 140 °C, 5 min |

The resulting thicknesses estimated from the resists' data sheets are: 250 nm of Copolymer, 60 nm of PMMA.

Electron beam exposure

In order to find the alignment marks, the SEM has to be focused roughly on the resist surface. This can be achieved easiest by creating a small scratch in the resist in an uncritical position. Alignment marks in the corners of the chip can be used to define a coordinate system to find the write fields and their alignment marks.

The bond pads and leads were designed with the $(300 \mu\text{m})^2$ writing field of the lithography system in mind. It allows for and was used with a step size of 10 nm. Higher resolution can be achieved with a $(100 \mu\text{m})^2$ writing field and a step size of 4 nm.

| Voltage | Aperture | Area dose |
|---------|-------------------|-------------------------------|
| 30 kV | 7.5 μm | 250 $\mu\text{C}/\text{cm}^2$ |

The numbers given are for a single unangled evaporation. The undercut was enough for a good lift-off, but we were unable to create enough undercut for proper shadow evaporation, even though various approaches were tried (different developer systems, thicker copolymer layer, a widespread background exposure).

Development

Develop in E56 for 1 minute in slight agitation. Stop by bathing in pure isopropanol for one minute. Blow dry with nitrogen, and dry on a hotplate at 95°C for ten minutes, in order to remove remaining solvent to avoid outgassing during deposition.

Evaporation

Most stable rates were achieved slowly heating the tungsten boat by slowly increasing the heating current until a small rate (0.1 Å/s) appears. As the Aluminum evaporates from the source, heating current has to be adjusted to compensate for changing rates.

Parameters used for the thickness dependence experiment were

| Target | Chamber pressure | Thickness | Rate |
|--------|------------------------|----------------|---------|
| Al | $9 \cdot 10^{-6}$ mbar | 20 nm or 40 nm | 0.2 Å/s |

Lift-off

As in the photolithography lift-off, a certain amount of ultrasound is helpful. Warm (60°C) acetone was usually sufficient.

Oxidation considerations

Due to the deficiencies of the undercut, Junctions were never produced by the author. We did, however, acquire some experience of a suitable oxidation procedure in our type of machine.

The general procedure is simple: after the first layer has been deposited, wait until the sample is back at room temperature. Then, flood the chamber with the desired amount of oxygen, wait for a certain amount of time (on the order of minutes), then remove the oxygen. The thickness of the layer then depends on oxidation time and oxygen partial pressure.

The control of partial oxygen pressure can be improved if one has a gas mixture with a defined Oxygen concentration, e.g. 10 %. In our case, this shifted the total pressure during oxidation to a range that was better accessible by our pressure gauges.

We installed a small buffer volume in the path of the oxidizing gas. It could be filled with Oxygen or oxidizing gas mixture at around ambient pressure, and then connected with the chamber volume. The resulting chamber pressure was very reproducible, inviting to keep this part constant and vary the oxidation time only.

A vacuum lock was installed in the Univex machine, separating the reaction chamber from the turbomolecular pump. This means that the turbo pump can be kept running at full speed while the chamber is filled with a thin gas, as opposed to shutting down the pump for the oxidizing step, as was required in the original chamber design. It has been experimentally tested that the chamber pressure can be reduced very quickly if the lock is opened to reconnect the running pump with the chamber once oxidation is completed, provided the total chamber pressure does not exceed the 1 mbar range. The turbo pump is loaded considerably, but only for a short time, and not more than in an emergency shutdown.

Bibliography

- [Max73] J. C. Maxwell. *A Treatise on Electricity and Magnetism, Vol. 1*. Oxford: Clarendon Press, 1873.
- [Onn11] Heike Kamerlingh Onnes. “Further Experiments with Liquid Helium: G. On the Electrical Resistance of Pure Metals, Etc. VI. On the Sudden Change in the Rate at which the Resistance of Mercury Disappears”. In: *KNAW, Proceedings*. Vol. 14. 1911, pp. 1911–1912.
- [Nyq28] H. Nyquist. “Thermal Agitation of Electric Charge in Conductors”. In: *Phys. Rev.* 32 (1 1928), pp. 110–113.
- [Tes34] Nikola Tesla. *Radio Power Will Revolutionize the World*. Modern Mechanics and Inventions magazine. <http://blog.modernmechanix.com/radio-power-will-revolutionize-the-world/>. 1934.
- [BCS57] J. Bardeen, L. N. Cooper, and J. R. Schrieffer. “Theory of Superconductivity”. In: *Phys. Rev.* 108 (5 1957), pp. 1175–1204.
- [Jos62] B.D. Josephson. “Possible new effects in superconductive tunnelling”. In: *Physics Letters* 1.7 (1962), pp. 251–253.
- [AB63] Vinay Ambegaokar and Alexis Baratoff. “ERRATUM: Tunneling Between Superconductors”. In: *Phys. Rev. Lett.* 11.2 (1963), p. 104.
- [Sha63] S. Shapiro. “Josephson Currents in Superconducting Tunneling: The Effect of Microwaves and Other Observations”. In: *Phys. Rev. Lett.* 11 (2 1963), pp. 80–82.
- [NM65] W. D. Niven and J. C. Maxwell. *The Scientific Papers of James Clerk Maxwell: Two Vol. Bound as One*. Dover, 1965.

- [MT71] R. Meservey and P. M. Tedrow. "Properties of Very Thin Aluminum Films". In: *Journal of Applied Physics* 42.1 (1971), pp. 51–53.
- [SGW74] H. Sixl, J. Gromer, and H.C. Wolf. "Energy gaps and transition temperatures of ultrathin superconducting films". In: *Physics Letters A* 47.1 (1974), pp. 47–48.
- [Dol77] G. J. Dolan. "Offset masks for lift-off photoprocessing". In: *Applied Physics Letters* 31.5 (1977), pp. 337–339.
- [Lou79] O. V. Lounasmaa. "Dilution refrigeration". In: *Journal of Physics E: Scientific Instruments* 12.8 (1979), p. 668.
- [HHJ81] R.E. Howard, E.L. Hu, and L.D. Jackel. "Multilevel resist for lithography below 100 nm". In: *Electron Devices, IEEE Transactions on* 28.11 (1981), pp. 1378–1381.
- [Lik86] K. K. Likharev. *Dynamics of Josephson junctions and circuits*. Gordon and Breach Science Publishers New York, 1986.
- [DD88] G.J. Dolan and J.H. Dunsmuir. "Very small (≈ 20 nm) lithographic wires, dots, rings, and tunnel junctions". In: *Physica B: Condensed Matter* 152.1–2 (1988), pp. 7–13.
- [Law88] C. J. Lawrence. "The mechanics of spin coating of polymer films". In: *Physics of Fluids* 31.10 (1988), pp. 2786–2795.
- [She88] D. Sheff. "Izzy, Did You Ask a Good Question Today?" In: *The New York Times* (1988). <http://www.nytimes.com/1988/01/19/opinion/1-izzy-did-you-ask-a-good-question-today-712388.html>.
- [Del91] P. Delsing. "One-Dimensional Arrays of Small Tunnel Junctions". In: *Single Charge Tunneling, Vol 294 of NATO Advanced Study Institute Series B: Physics*. Ed. by H. Grabert and M. H. Devoret. Plenum, New York, 1991. Chap. 7.
- [IN91] G.-L. Ingold and Yu. V. Nazarov. "Charge Tunneling Rates in Ultrasmall Junctions". In: *Single Charge Tunneling, Vol 294 of NATO Advanced Study Institute Series B: Physics*. Ed. by H. Grabert and M. H. Devoret. Plenum, New York, 1991. Chap. 2.

- [Ast95] K.J. Astrom. "PID controllers: theory, design and tuning". In: *Instrument Society of America* (1995).
- [HD96] David B. Haviland and Per Delsing. "Cooper-pair charge solitons: The electrodynamics of localized charge in a superconductor". In: *Phys. Rev. B* 54.10 (1996).
- [HBJS96] Ziv Hermon, Eshel Ben-Jacob, and Gerd Schön. "Charge solitons in one-dimensional arrays of serially coupled Josephson junctions". In: *Phys. Rev. B* 54 (2 1996), pp. 1234–1245.
- [Kau96] R L Kautz. "Noise, chaos, and the Josephson voltage standard". In: *Reports on Progress in Physics* 59.8 (1996), p. 935.
- [Zor+96] A. B. Zorin, F.-J. Ahlers, J. Niemeyer, T. Weimann, H. Wolf, V. A. Krupenin, and S. V. Lotkhov. "Background charge noise in metallic single-electron tunneling devices". In: *Phys. Rev. B* 53 (20 1996), pp. 13682–13687.
- [MR97] Mark A McCord and Michael J Rooks. "Electron beam lithography". In: *Handbook of microlithography, micromachining, and microfabrication* 1 (1997), pp. 139–249.
- [Mel+97] J. A. Melsen, Ulrik Hanke, H.-O. Müller, and K.-A. Chao. "Coulomb blockade threshold in inhomogeneous one-dimensional arrays of tunnel junctions". In: *Phys. Rev. B* 55 (1997), pp. 10638–10642.
- [Sch97] V. V. Schmidt. *The physics of superconductors*. Ed. by P. Mueller and A. V. Ustinov. Springer, 1997.
- [Bou+98] V Bouchiat, D Vion, P Joyez, D Esteve, and M H Devoret. "Quantum coherence with a single Cooper pair". In: *Physica Scripta* 1998.T76 (1998), p. 165.
- [Kni98] David Knight. *Humphry Davy: science & power*. Cambridge University Press, 1998, p. 87.
- [Mat98] Donald M. Mattox. *Handbook of physical vapor deposition (PVD) processing : film formation, adhesion, surface preparation and contamination control*. Westwood, NJ: Noyes Publications, 1998.

- [Ust98] A.V. Ustinov. "Solitons in Josephson junctions". In: *Physica D: Nonlinear Phenomena* 123.1-4 (1998), pp. 315 -329.
- [JH00] J. Johansson and D. B. Haviland. "Random background charges and Coulomb blockade in one-dimensional tunnel junction arrays". In: *Phys. Rev. B* 63 (1 2000), p. 014201.
- [AAH01] Peter Agren, Karin Andersson, and David B. Haviland. "Kinetic Inductance and Coulomb Blockade in One Dimensional Josephson Junction Arrays". In: *Journal of Low Temperature Physics* 124 (2001), pp. 291-304.
- [Hav+01] D.B. Haviland, K. Andersson, P. Agren, J. Johansson, V. Schöllmann, and M. Watanabe. "Quantum phase transition in one-dimensional Josephson junction arrays". In: *Physica C: Superconductivity* 352.1-4 (2001), pp. 55 -60.
- [WH01] Michio Watanabe and David B. Haviland. "Coulomb Blockade and Coherent Single-Cooper-Pair Tunneling in Single Josephson Junctions". In: *Phys. Rev. Lett.* 86 (22 2001), pp. 5120-5123.
- [Agr02] P. Agren. "Charging effects in small capacitance Josephson junction circuits". PhD thesis. Royal Institute of Technology, Stockholm, 2002.
- [BB004] Ivo Babuška, Uday Banerjee, and John E. Osborn. "Generalized Finite Element Methods — Main Ideas, Results and Perspective". In: *International Journal of Computational Methods* 01.01 (2004), pp. 67-103.
- [Piq+04] François Piquemal, Alexandre Bounouh, Laurent Devoille, Nicolas Feltin, Olivier Thevenot, and Gérard Traçon. "Fundamental electrical standards and the quantum metrological triangle". In: *Comptes Rendus Physique* 5.8 (2004), pp. 857-879.
- [Tin04] Michael Tinkham. *Introduction to superconductivity*. 2nd ed. Dover Publications, 2004.

- [Fer+06] A.J. Ferguson, N. A. Court, F.E. Hudson, and R.G. Clark. "Thin-film aluminium for superconducting qubits". In: *Nanoscience and Nanotechnology, 2006. ICONN '06. International Conference on*. 2006.
- [Cou+08] N. A. Court, A. J. Ferguson, R. Lutchyn, and R. G. Clark. "Quantitative study of quasiparticle traps using the single-Cooper-pair transistor". In: *Phys. Rev. B* 77 (2008), p. 100501.
- [IL08] H. Ibach and H. Lüth. *Festkörperphysik: Einführung in die Grundlagen*. Springer, 2008.
- [LU08] A. Lukashenko and A. V. Ustinov. "Improved powder filters for qubit measurements". In: *Review of Scientific Instruments* 79.1 (2008), pp. 014701–014701–4.
- [Mai+09] Ville F Maisi, Yuri A Pashkin, Sergey Kafanov, Jaw-Shen Tsai, and Jukka P Pekola. "Parallel pumping of electrons". In: *New Journal of Physics* 11.11 (2009), p. 113057.
- [Nis+09] Masayoshi Nishiyama, Steven Kleijn, Vincenzo Aquilanti, and Toshio Kasai. "Temperature dependence of respiration rates of leaves, 180-experiments and super-Arrhenius kinetics". In: *Chemical Physics Letters* 482.4–6 (2009), pp. 325–329.
- [RS09] Stephan Rachel and Alexander Shnirman. "Theory of small charge solitons in one-dimensional arrays of Josephson junctions". In: *Phys. Rev. B* 80 (18 2009), p. 180508.
- [SEA09] S. V. Syzranov, K. B. Efetov, and B. L. Altshuler. "dc Conductivity of an Array of Josephson Junctions in the Insulating State". In: *Phys. Rev. Lett.* 103 (12 2009), p. 127001.
- [GH10] W. Guichard and F. W. J. Hekking. "Phase-charge duality in Josephson junction circuits: Role of inertia and effect of microwave irradiation". In: *Phys. Rev. B* 81 (6 2010), p. 064508.
- [Fie11] Andreas Fiebig. "Measurements on one-dimensional Josephson nano junction arrays of different length". Diplomarbeit. Karlsruhe Institute of Technology, 2011.

- [Gre+11] Tine Greibe, Markku P. V. Stenberg, C. M. Wilson, Thilo Bauch, Vitaly S. Shumeiko, and Per Delsing. “Are “Pinholes” the Cause of Excess Current in Superconducting Tunnel Junctions? A Study of Andreev Current in Highly Resistive Junctions”. In: *Phys. Rev. Lett.* 106 (9 2011), p. 097001.
- [Sch11] R. Schaefer. unpublished. 2011.
- [Sai+12] O.-P. Saira, A. Kemppinen, V. F. Maisi, and J. P. Pekola. “Vanishing quasiparticle density in a hybrid Al/Cu/Al single-electron transistor”. In: *Phys. Rev. B* 85 (2012), p. 012504.
- [Zwi12] Heiner Zwickel. “Entwicklung eines Lithographieverfahrens für supraleitende Bauteile zur Bestimmung der kritischen Temperatur von dünnen Aluminiumfilmen”. Bachelor’s thesis. Karlsruhe Institute of Technology, 2012.
- [Zim+13] J. Zimmer, N. Vogt, A. Fiebig, S. V. Syzranov, A. Lukashenko, R. Schäfer, H. Rotzinger, A. Shnirman, M. Marthaler, and A. V. Ustinov. “Thermally activated conductance in arrays of small Josephson junctions”. In: *ArXiv e-prints* (June 2013). eprint: arXiv:1306.6304.

Acknowledgments

It is a mistake to think you can solve any major problems just with potatoes.

Douglas Adams
Life, the Universe and Everything (1982)

The results presented here were influenced or made possible by many people, to whom I would like to express gratitude.

I would like to thank Prof. Alexey V. Ustinov for giving me the opportunity to work at Physikalisches Institut, and for directing my research, helping me to finish my thesis in time. My thanks also go to Prof. Alexander Shnirman for accepting to become second referee.

I owe my deep gratitude to Dr. Hannes Rotzinger, who I consider in many ways to be the primary supervisor of this work. Thank you for many hours of important discussions, and for crucial contributions to the experiments reported.

I would like to thank Andreas Fiebig and Dr. Roland Schäfer for experimental collaboration, especially for sharing several of their samples. Many thanks to Dr. Alexander Lukashenko for keeping the black fridge operational for my experiments.

Thanks to Adem Ergül and Prof. David Haviland from KTH Stockholm for providing samples on several occasions.

On the theory side, I'd like to thank Dr. Michael Marthaler and Nicolas Vogt for developing the equations to understand my measurements. I am grateful to Dr. Sergey Syzranov for many helpful discussions.

I would like to thank Heiner Zwickel, whose Bachelor thesis I had the honor to supervise. During your stay in the group, we made several important advances in our fabrication technology.

I would like to acknowledge Dr. Richard Montbrun and Jacques Hawecker, who helped me during my first attempts at electron beam lithography.

Acknowledgments

My thanks also go to Stefan Kühn for his work on the SEMs, Christopher Reiche for collaboration on the DWL 66, and Simon Hettler and Patrice Brenner for help with the PVD 75. I am grateful to Felix Maibaum and Dr. Alexey Feofanov for useful discussions.

Many thanks to all members of Ustinov group, the workshops and secretaries, and all members of Physikalisches Institut for providing a productive and sometimes even fun environment to work in.

Thanks to Philipp Jung, Dr. Michael Marthaler and especially Dr. Hannes Rotzinger for proofreading.

My personal thanks go my family: Mama, Elke, Insa und Oma Anneliese, who helped me become a person capable to do this kind of work.

I am especially grateful for the personal support I recieved from my girlfriend Gabriele Westhoff, and from Christina Stawiarski, Andreas Kosmider and Patricia Huber. Thanks for being great friends!

The White Rabbit put on his spectacles. 'Where shall I begin, please your Majesty?' he asked. 'Begin at the beginning,' the King said gravely, 'and go on till you come to the end: then stop.'

Lewis Carroll,
Alice's Adventures in Wonderland (1865)

